A THERMODYNAMIC AND OPTICAL ASSESSMENT OF SOLUBLE CARBON PARTICULATE EFFECTS ON LIPID FILM STRUCTURE AND ORGANIZATION

by

Nida Shaikh

A dissertation submitted in partial fulfillment
of the requirements for the degree

of

Doctor of Philosophy

in

Chemistry

MONTANA STATE UNIVERSITY
Bozeman, Montana

May 2022

DEDICATION

This dissertation is dedicated to my family, friends, colleagues, and loves ones. Your love and support were essential. Thank you all.

To my support system, with love ♥

ACKNOWLEDGEMENTS

First and foremost, I’d like to thank my advisor Dr. Rob Walker. He embodies everything I inspire to be, both as a respected scientist and as a general person. He is knowledgeable yet humble, isn’t afraid to think out loud but does so very eloquently, values a work-life/personal-life balance, and will be the first to tell you that having a life/hobbies outside of graduate school is just as important as work.

Thank you to both past and present members of the Walker Research Group, especially Dr. Katie Link and Dr. Grace Purnell for showing me the ropes, for grilling me, and for letting me ask any (even basic) questions (even after you graduated).

Thank you to Katie Duncan for sharing this journey with me (and for making us gallons and gallons of coffee every morning). I don’t know how I would have made it through graduate school without your friendship.

Thank you also to my committee members, Dr. Mary Cloninger, Dr. Erik Grumstrup, Dr. Berk Knighton, and Dr. Nicholas Stadie – your insightful questions and suggestions were essential in helping to guide me through this journey.

I’d like to thank Dr. Daniel Juliano, Nick Zelver, Dr. Quinton King, Dr. Darin Oelkers, Dr. Austin Leach, Dr. Jonathan Baker, Dr. Matthieu Dumont, Gary Bloomer, and James Austin for thoughtful discussions on, and/or training in, evaluating, licensing, and marketing technologies, patent law, and intellectual property in general.

An EXTRA big thank you to Doreen Brown who I think has the hardest job.

Last but not least, thank you to NSF EPSCoR for funding and to all of the CREWS members who have challenged me to communicate science across disciplines.

TABLE OF CONTENTS

1. INTRODUCTION

TABLE OF CONTENTS CONTINUED

TABLE OF CONTENTS CONTINUED

LIST OF TABLES

Table Page

LIST OF FIGURES

LIST OF FIGURES CONTINUED

Figure Page

LIST OF FIGURES CONTINUED

Figure Page

LIST OF FIGURES CONTINUED

ABSTRACT

Research described in this thesis investigates the effects of carbonaceous particulate matter on model biological membrane structure, organization, and function. Although the harmful impacts of black carbon are well-documented, researchers lack the chemically-specific, mechanistic information necessary for understanding how black carbon aerosols affect lung surfactant spreading and compression. Surface specific optical spectroscopy methods together with complementary thermodynamic methods are used to measure how carbon nanoparticles, a model for black carbon aerosols that are a component of particulate matter ($PM_{2.5}$), change average lipid conformation, orientation, thickness, and compressibility in monolayers, and how these changes affect overall membrane organization. Addressing these questions requires a suite of independent, but complementary, experimental techniques including Langmuir trough and surface tension measurements, surface specific nonlinear optical spectroscopy measurements including both second harmonic generation and sum frequency generation, and spectroscopic ellipsometry measurements. Work presented in this thesis discusses cooperative adsorption as a possible mechanism to explain the interactions between DPPC monolayers and PHFs at biologically-relevant aqueous – air interfaces. The experiments forthcoming represent a detailed investigation of 1) the mechanism(s) responsible for accumulation of carbon particulates at the aqueous/monolayer/air interface present in the lungs, and 2) how specific thermodynamic behavior and optical properties (i.e. structure, composition, membrane integrity, orientation, thickness, and organization) at the aqueous/monolayer/air interface change with the inclusion of non-biological, nano-sized materials. Motivating this work is a need to develop a predictive understanding of black carbon – lung surfactant interactions and how non-biological, nano-sized materials impact membrane structure and function.

CHAPTER ONE

INTRODUCTION

1.1 Motivation

Work described in this dissertation details how a combination of independent thermodynamic and optical methods were used to characterize interactions between soluble carbon particulates and lipid films adsorbed to the water – air interface. These experiments draw their motivation from the need to understand how lipid monolayers interact with non-biological, nano-sized particulates commonly found in ambient conditions. Specifically, carbon particulates generated from biogenic (e.g. wildfires) and anthropogenic (e.g. automobiles) sources are known to compromise lung surfactant function, leading to pulmonary disease and other health complications. Furthermore, carbon particulates – often described as black carbon aerosols – change in composition as they age, so these interactions will depend upon time dependent properties such as size, chemical composition, and aqueous phase solubility. The introduction of this thesis begins by describing black carbon and its life cycle. Following this description, lipid films and lung surfactant function is described. Section 1.2 details the model systems chosen as surrogates for the physiological systems that motivate these studies and Section 1.3 addresses the fundamental scientific considerations that are believed to control particulate-lipid interactions. Section 1.4 provides an overview of the techniques used in this research, the properties that are measured, and the conclusions that can be drawn from acquired data.

1.1.1 Black Carbon

Black carbon (BC) is a general term that describes a mixture of products resulting from incomplete combustion and anthropogenic activities, and this material presents physiological and environmental threats due to its extreme chemical heterogeneity.[1] In the U.S., approximately 35% of BC emissions come from wildfires, 52% from transportation (vehicle and aircraft), and the remaining 13% come from the energy and industry sectors.[2] The physiological and environmental impacts of BC can fall into various categories which include health effects, water quality, climate change, and air pollution. BC arising from incomplete combustion and anthropogenic activities leads to increased air pollution.[3] Specific to air pollution, although BC is generally considered a short-lived pollutant, it does persist in the atmosphere. Smaller BC particulates can remain suspended indefinitely, and these suspended particulates collide and react with other airborne particulates making BC more chemically heterogeneous (with elemental carbon content dropping from 80% in newly generated particles to under 50% in aged particles).[4, 5] Additionally, due to its short lifetime, newly generated BC often poses stronger negative health and environmental impacts than aerosolized pollutants of longer lifetimes. Specific to climate change, BC causes positive radiative forcing, leads to global warming, as well expedites the melting of snow/ice.[3, 6-8] Specific to adverse health effects, approximately seven million people die every year from poor air quality/air pollution, with particulate matter pollution being the leading cause of premature deaths.[9] Specific to BC contamination impacting water quality, 10% of dissolved organic carbon in rivers is in the form of dissolved BC.[1] In order to assess and predict BC's impact on physiological and ecological health, researchers must be able to monitor where BC aerosols are generated and what happens to them as they persist in the atmosphere.

Freshly generated BC particulates are primarily hydrophobic and can be externally mixed with other ambient aerosol constituents.[8, 10] Previous studies have found that BC particulates age in the atmosphere through condensation and coagulation processes.[8] More recent studies have found that freshly generated BC becomes coated by water-soluble material during atmospheric aging, including condensation of sulfate, nitrate, and small volatile organic species, coagulation with preexisting aerosols, and heterogeneous reactions with gaseous oxidants.[8] Consequently, BC aerosols transform from having a surface of primarily carbon and being strongly hydrophobic, to having the presence of oxygen and making the surface more hydrophilic, posing a threat to water – air interfaces.[10] Although models exist to estimate BC aging time, results are inconsistent. For example, in one model the average BC aging rate in Beijing, China is roughly seven times higher than that in Houston, Texas. In another model approximately 23.1 hours on average is required in Beijing, China to complete the hydrophobic-to-hydrophilic conversion, while it takes approximately 8.3 hours for the same conversion process in Houston, Texas.[6] Regardless of the models being used and the variable BC aging rates, the aging process for BC, specifically the hydrophobic-to-hydrophilic conversion process, happens on a very short time scale considering the lifetime of BC ranges from days to weeks. Given this short lifetime coupled with this short time scale for the hydrophobic-to-hydrophilic process, BC can significantly impact water – air interfaces.

Recent reports suggest that BC aerosols from combustion sources adversely impact human health more than BC aerosols from other sources.[11] Adsorption of BC aerosols to biologically relevant aqueous/vapor interfaces such as alveoli surfaces causes health risks and is linked to increased mortality rates throughout the world.[12, 13] Specific to pulmonary diseases, BC aerosols change the structural, elastic, and dynamic properties of lung surfactant and inhibit O_2 transport across the lung lining and into the bloodstream.[13] Lung surfactant, which is the final line of defense from nanoparticle inhalation, is a heterogeneous chemical mixture consisting primarily of saturated lipids, specifically 1,2-dipalmitoyl-sn-glycerol-3-phosphocholine (DPPC), with a small amount of proteins. Despite the harmful effects posed by BC aerosols to lung surfactant function, researchers lack the chemically-specific, mechanistic information necessary for understanding how BC aerosols affect lung surfactant spreading and compression, ultimately leading to decreased lung surfactant functionality.

Several methods exist to measure poor air quality and direct health impacts. Currently, the FAA uses a combination of field monitoring and dispersion modeling studies along with statistical methods to estimate BC aerosol toxicity.[14] Additionally, EPA researchers have developed models such as the Human Exposure Model (HEM) to perform risk assessments from sources that emit toxic aerosols into ambient air (i.e. studying the inhalation pathway of exposure in order to make predictions about risks associated with toxic aerosols). EPA models such as the HEM are also being used to further learn about BC composition, compare BC impacts relative to those of other airborne particles, evaluate how particulates absorb and scatter different wavelengths of light, and study the effects of BC on human health through controlled clinical studies examining effects from exposure to different air quality.[15] Much of the health impacts of BC and particulate matter are studied in vitro and in vivo – not very many studies exist that investigate fundamental interactions at the molecular level.[9, 16] Based on *in vitro* and *in vivo* studies, particular concern are the class of particles labeled $PM_{2.5}$ ($< 2.5\ \mu$m in diameter) and especially particles smaller than 100 nm because they can be readily inhaled and penetrate deep into the lungs and bloodstream and translocate to other organs and tissues.[16, 17]

BC poses significant impacts on air pollution, climate change, water quality, and health. However, several questions such as "What factors control short and long-term health and environmental effects?" and "Are the level of health and environmental effects dependent on a particle's chemical composition or concentration?" remain unanswered. Although these policy-driven questions address health impacts of BC inhalation, they do not address fundamental interactions at the molecular level. Current work being done is largely correlative – we can anticipate or predict the effects of these aerosols on human health, but we still don't know how or why BC leads to negative health effects.

My work is motivated by recent reports suggesting that insoluble elemental carbon nanoparticles, models for freshly generated BC with high elemental carbon content, within a DPPC monolayer affect DPPC domain growth by inducing DPPC, a model for lung surfactant, to first form incompressible microscopic domains that exclude the nanoparticles.[12, 13] The domains then increase in size as more DPPC molecules adhere to the domain perimeter. Because the carbon nanoparticles aggregate around the lipid domain perimeters, smaller domains are unable to come together and form larger structures leading to reduced monolayer elasticity and decreased rigidity.[12]

Based on existing models I hypothesize that soluble carbon nanoparticles, models for BC in the atmosphere that has aged and become oxidized, will affect DPPC monolayer structure and organization by cooperatively adsorbing to lipid films, leading to changes in monolayer orientation and packing.

Testing this hypothesis requires addressing fundamental physical phenomena, specifically interactions at the molecular level. To do so, this thesis will address several questions to test the proposed hypothesis. These questions include: 1) Are soluble carbon particulates surface active?; 2) Do soluble carbon particulates remain associated with biologically-relevant lipid films?; 3) If so, how do these associations affect structure and organization in biologically-relevant lipid monolayers?; and 4) What role, if any, does particulate aggregation play in the behaviors? Research discussed in this dissertation will use optical and thermodynamic techniques to examine the effects of polyhydroxylated fullerenes (PHFs), surrogates for aged BC, on model biological membranes.[18, 19] The studies will focus on using well-controlled model systems to determine 1) the mechanism(s) responsible for carbon particulate accumulation at the aqueous/monolayer/vapor interface; and 2) how specific thermodynamic and optical properties at the aqueous/monolayer/vapor interface change with the inclusion of carbon particulates. Using a well-defined model biological DPPC monolayer intended to serve as a lung surfactant surrogate and PHFs as a model for BC components will allow us to propose a mechanistic understanding of PHF – lipid film interactions.

1.2 Model Systems

1.2.1 Aged Black Carbon and Lung Surfactant

Nanoparticles can be readily inhaled, and they penetrate deep into one's lungs.[17] Lung alveoli have an aqueous – vapor interface, shown in Figure 1.1, that acts as a final line of defense from foreign nanoparticles in the air. Once inhaled, nanoparticles can penetrate and interact with the lung surfactant lining in the alveoli. Lung surfactant is a heterogeneous chemical mixture consisting primarily of saturated DPPC (90%), with a small amount of surfactant associated proteins (10%).[20, 21] Lung surfactant functions to lower surface pressure of alveoli to near zero during breathing to prevent lung collapse. The surfactant layer is subject to disruption when nanoparticles are introduced to it. Reduced lung surfactant efficacy is the result of nanoparticle integration into lung surfactant. Despite the widely known harmful effects of carbonaceous nanoparticles on lung surfactant function, we still lack the chemically – specific, mechanistic information necessary for understanding *how* inhalation of these carbonaceous nanoparticles affects lung surfactant spreading and compression.

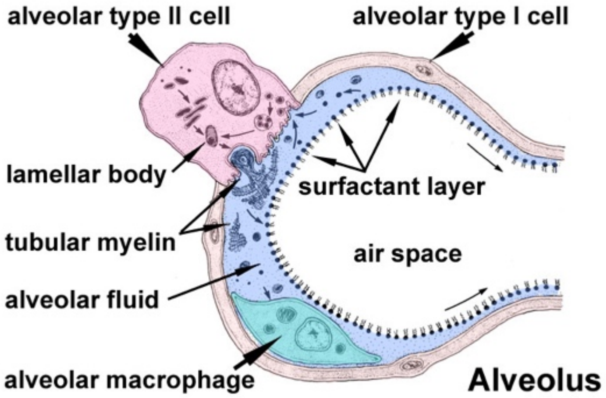

Figure 1.1. Aqueous/vapor interface in the alveoli of lungs [22].

Successfully identifying how aged carbonaceous nanoparticles affect lipid monolayer structure, organization and compressibility will require a model system that has well controlled lipid compositions and controlled concentrations of carbon particulates so that a single component in a well-known system can be changed in order to isolate a lipid monolayer's thermodynamic and optical behavior change as a function of carbon nanoparticle concentration. Studies described in this dissertation used a well-defined biological membrane model system with DPPC (Figure 1.2), the primary component of lung surfactant, and polyhydroxylated fullerenes (Figure 1.2) as a model for BC that has aged in the atmosphere and become oxidized.

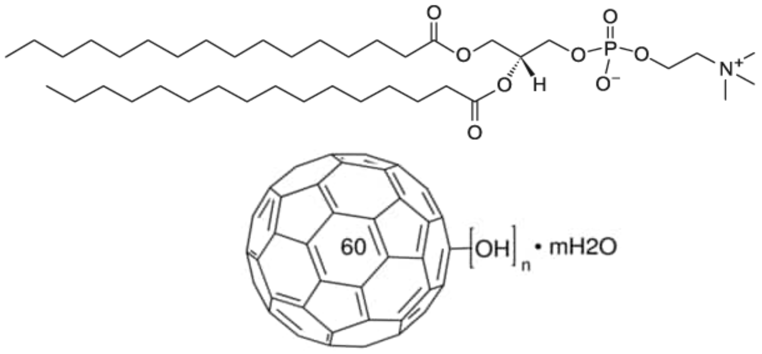

Figure 1.2. 1,2-dipalmitoyl-sn-glycerol-3-phosphocholine (DPPC) (top) and polyhydroxylated fullerene (PHF) (bottom).

Carbonaceous nanoparticles, such as carbon nanopowder, fullerene, and polyhydroxylated fullerenes, are products that are commercially available with varying elemental carbon content, and are often used as model materials to examine the properties of BC.[4] Polyhydroxylated fullerenes (PHFs) – also called 'fullerols' or 'fullerenols' – comprise a family of soluble carbon particulates that have been targeted for applications as diverse as drug delivery, metal nanoparticle catalysis and agricultural pest control.[23-29]

Interest in PHFs as a functional carbon nanoparticle is driven by its ability to generate reactive oxygen species when irradiated with UV light.[30, 31] PHFs have also been associated with harmful environmental and physiological outcomes.[32-34]

PHFs consist of C_{60} fullerenes functionalized with a variable number ($n = 12 – 40$) of hydroxyl groups. PHFs are highly soluble in aqueous solution, with solubilities as high as 58.9 g/L having been reported.[35, 36] PHFs are known to behave nonideally at higher concentrations, forming aggregates that can be detected by dynamic light scattering.[35-37] Despite the large number of hydroxyl groups decorating the PHF surface, not all hydroxyl groups contribute to aqueous solubility. Numerous experimental and modeling studies report that there is asymmetry in the clustering of hydroxyl groups. Specifically, they tend to cluster on the fullerene surface where they can be stabilized internally through intramolecular hydrogen bonding[38-49], complicating efforts to understand PHF chemistry in aqueous solution and at aqueous interfaces. Furthermore, this asymmetry leaves PHFs with hydrophobic surface areas, and this amphiphilic structure enhances the likelihood of aggregate formation in water[50] and makes PHF surface activity more likely.[51, 52]

For the studies discussed in this thesis, water-soluble polyhydroxylated fullerenes are used as model for aged BC constituents that have oxidized in the atmosphere. Using varying concentrations of PHFs will allow me to change a single component of a well-defined system and isolate how changing particle properties (i.e. concentration) alters thermodynamic and optical behavior. Controlling lipid composition and PHF concentration 1) allows us to isolate the effects of adding specific PHF concentrations to a specific mixture of DPPC, 2) allows us to better determine the mechanism(s) responsible for accumulation of BC at the aqueous/monolayer/vapor interface present in lungs, and 3) allows us to understand how specific thermodynamic and optical properties of the aqueous/monolayer/vapor interface change with the inclusion of PHFs.

1.3 Underlying Scientific Principles

1.3.1 Adsorption to Aqueous – Air Interfaces

Aqueous – air interfaces are ubiquitous and are both environmentally and physiologically significant. These interfaces describe the surface/near-surface region where water meets air. Although the significance of these interfaces has been well-recognized, studies of water interfaces at the molecular level are fairly recent [53-56]. The main reason for this recent onset of experimental and computational discovery is due to a limited amount of highly surface-specific techniques that are effective enough to probe aqueous – air interfaces at the molecular level [53].

Experimentally identifying how a medium's bulk properties differ from those at the interface is fundamental in understanding molecularly-based mechanisms of adsorption, surface structure, and surface reactivity at the aqueous – air interface [57-59]. In its simplest terms, solute adsorption to an aqueous – air interfaces reflects solutes adsorbing to a surface when they wouldn't otherwise. The alveoli of our lungs consist of an aqueous – air interface, as shown in Figure 1.1, that acts as the final line of defense against nanoparticle inhalation. Once inhaled, nanoparticles can penetrate and adsorb to the lung surfactant lining in the alveoli, leading to deficiency and dysfunction of lung surfactant, and can contribute to a variety of harmful respiratory disorders and illnesses [60]. The studies discussed in this thesis specifically address interactions of PHFs and DPPC, models for aged/oxidized BC and lung surfactant, at a biologically-relevant aqueous – air interface.

Solute adsorption to interfaces can be difficult predict. Understanding even the simplest of questions about a solute's tendency to adsorb to interfaces requires knowledge of solute-substrate, solvent-substrate, and solute-solvent energetics and interactions.[61] Overarching questions about solute adsorption to interfaces can be distilled to three specific queries: 1) Will a solute adsorb to a surface from solution?; 2) Is adsorption reversible or irreversible?; and 3) Does adsorption cease at terminal monolayer coverage, or will more solutes continue to accumulate leading to aggregate and/or multilayer formation?[61] Answers to these questions depend sensitively on substrate, solute, and solvent identity and interactions, as well as anisotropy induced at the interface. From a microscopic perspective, adsorption mechanisms can be used to assess fundamental interactions at the molecular level at an interface of interest.

The consequences of cooperative adsorption to liquid interfaces are far-ranging in a host of fields including groundwater remediation, sea spray aerosols (SSA), black carbon (BC), and remote sensing.[61-74] When considering liquid interfaces, cooperative adsorption is a common proposed mechanism for molecular interactions occurring at these interfaces. This thesis describes cooperative adsorption to a liquid interface as potential non-covalent interactions (at the surface/near-surface region) between insoluble molecules at the interface, and solutes in the bulk phase, with the interface being the depth to which anisotropy exists. More specifically, the work in this thesis investigates the hypothesis that soluble carbon particulates will adsorb to biologically-relevant lipid films at the water – air interface when they wouldn't otherwise.

1.3.2 Cooperative Adsorption

In the broadest sense, cooperative adsorption describes synergistic effects that enhance adsorbate surface activity relative to expectations based on simple ideal interactions between independent, non-interacting species and an interface.[75-78] These interactions can be as simple as Coulomb attractions between oppositely charged surfactants that lead to surfactant crowding at a water–air interface,[79] or as nuanced as entropy driven changes that drive selective ion adsorption at liquid surfaces.[80-82] Cooperative adsorption has been addressed with thermodynamic models that consider changes to surface tension and the impact of double layer formation[83-85] as well as with more discrete, molecular descriptions that include multivalent interactions between monomers and aggregates and adsorbate conformational effects responsible for isomer separation.[76, 86-90] Regardless of how cooperative adsorption is described, the phenomenon has important effects on the properties of physiological, industrial, and environmental systems.

1.3.2.1 Differentiating Ideal vs. Non-ideal Interaction Cooperative Adsorption Systems. Unlike the cooperative adsorption model, the Langmuir adsorption model ignores adsorbate/adsorbate interactions. Experimental evidence exists for adsorbate/adsorbate interactions, specifically with two distinct types of adsorbate/adsorbate interactions: direct interaction and indirect interaction. Direct interactions between adjacent adsorbed molecules might make additional adsorption more likely or less likely depending on specific details about the resulting monolayer structure and organization. This direct interaction has the greatest effect on high-coverage behavior. Adsorbates also have an indirect effect on further adsorption when changes in surface properties affect subsequent adsorption of additional adsorbates. In the cooperative adsorption model, *both* direct and indirect interactions can occur *simultaneously*.

1.3.2.2 Differentiating Competitive Adsorption from Cooperative Adsorption.

Unlike the cooperative adsorption model, the Langmuir adsorption model is a reversible process – the cooperative adsorption model can be either reversible or irreversible. In the Langmuir adsorption model, adsorption is explained with the assumption that an absorbate behaves as an ideal gas at isothermal conditions. The sub-phase is assumed to be an ideal solid surface composed of distinct adsorption sites capable of binding the absorbate. In the most basic model, we assume that there is only one species adsorbing to the surface. Competitive adsorption considers the case when there are two distinct absorbates present in the system. Both adsorbates compete for the same adsorption sides on the adsorbent. The competitive adsorption model assumes that all adsorption sites are equivalent, and that each site can hold at most just one of the two absorbates, not both adsorbates simultaneously. Additionally, there are no interactions between adsorbate molecules on adjacent sites. For the cooperative adsorption model discussed in this thesis, with the presence of a tightly packed insoluble lipid monolayer adsorbed to the surface no vacant interstitial space between the lipid monomers exists for a soluble adsorbate to occupy. However, in the cooperative adsorption model, solutes with high solubilities *still* adsorb to the surface despite having *no* vacant adsorption sites, and the solutes *do* interact with the insoluble lipid monolayer when they wouldn't otherwise. These conclusions are self-evident in surface tension compression isotherms and are also readily informed from independent nonlinear and linear optical measurements.

1.3.2.3 Molecular Structure and Organization of Langmuir Films.

When considering adsorption to water – air interfaces, Langmuir films represent a limiting case because all molecules are constrained to the surface and cannot be solubilized in bulk aqueous solution. The amphiphilic nature of the surfactant has the charged headgroup solvated in the water with the two (saturated or unsaturated) acyl chains either lying on the surface (at low coverage) or generally directed along the surface normal (at high coverage). The water – air interface possesses excess free energy that originates from the difference in environment between the surface molecules and those in the bulk. This interfacial free energy can be measured by the system's surface tension. Surface pressure is then determined by measuring the surface tension between a clean surface and the same surface with an insoluble monolayer present. The most important indicator of monolayer properties (i.e. organization or packing) is given by measuring the surface pressure as a function of area of the water surface available to each molecule (often reported as mean molecular area or MMA).

Insoluble Langmuir films are a critical component in lung surfactant mixtures that enable alveoli to expand and contract without having to overcome the high surface tension associated with water-air interfaces. [64, 91-93] Lipids are also the primary components of biological membranes whose primary function is to contain and protect the interior of cells from chemical threats in the periplasm.[60, 64, 94, 95]. When considering insoluble lipid monolayers, lipid film function depends sensitively on the monolayer's structure and organization. Structure and organization in lipid monolayers adsorbed to liquid interfaces depends sensitively on conditions of the liquid subphase. Numerous studies have shown that solutes can intercalate into lipid films, inducing structural disorder, and altering membranes permeability and phase behavior [96-99].

Relevant for work described in this dissertation, recent studies have reported that soluble carbon particulates, surrogates for aged BC, also show an affinity for insoluble lipid films at liquid interfaces. BC aerosol adsorption to biologically relevant liquid interfaces such as alveoli surfaces has long been associated with health risks and is linked to increased mortality rates throughout the world [11-13]. Specific to pulmonary diseases, BC aerosols change the structural, elastic, and dynamic properties of lung surfactant [17, 100]. The mechanisms responsible for these effects, however, remain under debate. Specifically, the impact of carbon particulates on lung surfactant structure and organization, and the consequences of these interactions on lung surfactant's dynamic properties remain correlative at best. Experimental data suggest that low concentrations of BC do affect lipid monolayer structure strongly, suggesting cooperative adsorption where the DPPC attracts and retains BC in the surface/near surface region, enriching the interface's organic content and forcing lipid monolayers to adopt an altered structure [65, 66].

Work described in this dissertation examines interactions between highly soluble fullerene particles (polyhydroxylated fullerenes or PHFs) and Langmuir monolayers composed of the lipid 1,2_dipalmitoyl-*sn*-glycero-3-phosphocholine (DPPC). Data in Chapters 3 and 4 show that even though PHFs are themselves weakly surface active, very low bulk solution concentrations lead to observable and sometimes pronounced changes in DPPC structure and organization. These findings strongly suggest that PHFs are more strongly attracted to the aqueous surface covered by the lipid film. Such affinity is consistent with a cooperative adsorption mechanism. An invited review of cooperative adsorption phenomena is being prepared for submission to the journal *Langmuir*.

1.4 Techniques

1.4.1 Surface Specific Techniques

Cooperative adsorption in this thesis describes interactions between insoluble Langmuir monolayers and soluble organic molecules at the water/air interface.[65, 66, 101] We propose that the soluble organic molecules are drawn to the surface/near-surface region, through non-covalent interactions, by the insoluble lipid monolayer and they cooperatively adsorb. In order to investigate the cooperative adsorption mechanism at the water/air interface, surface specific techniques are required to address the questions outlined in 1.1.1.[53, 65, 66, 101]

To address whether PHFs are surface active, surface tension measurements will be used to obtain surface pressures of PHF solutions at varying concentrations. Gibbs adsorption equation will then be applied to these data to determine terminal surface coverages.[102] Next, Langmuir trough measurements will be used to investigate how PHFs affect a lipid film's thermodynamic properties. Langmuir trough experiments will examine lipid monolayer phase behavior, surface tension and collapse pressure when carbon particulates are introduced to a DPPC film. Langmuir trough isotherms will show phase changes the monolayer undergoes and how particle addition disrupts lipid film order. From these data we will determine whether PHFs remain associated with lipid films.

While thermodynamic data are instructive, they do not provide any direct information about surface behavior or molecular structure and organization. In order to determine how inclusion of carbonaceous particulates changes surface behavior at the interface, and how it changes lipid film organization, second harmonic generation (SHG) and vibrational sum frequency generation (VSFG), both second order nonlinear optical technique that measure surface behavior and vibrational spectra of surface species are used. SHG and VSFG will be used to look at microscopic changes occurring at the aqueous/vapor interface, specifically changes in surface behavior and the conformational distribution of the lipid films with the inclusion of carbon particulates. Finally, spectroscopic ellipsometry (SE) is used to observe macroscopic properties including lipid monolayer surface thickness and reflectivity

Together, data provide an independent, interlocking description of how PHFs affect lipid film structure, organization, and conformation. Using a simple model system (and building up in complexity) to study PHF – lipid film interactions in conjunction with the techniques mentioned above will provide us with specific molecularly resolved data that is both quantitative and enables us to predict how specific PHF concentrations affect model biological membranes while providing clues about the molecular origin of detrimental health effects induced by BC.

1.4.1.1 Langmuir Trough and Surface Tension. Langmuir monolayers of lipids (i.e. DPPC) and lipid-based mixtures are common models used to study surface properties of biological systems.[13, 103-107] Langmuir trough surface tension measurements are used to measure the two-dimensional phase behavior of lipid monolayers. Compression isotherms provide a measure of the phase changes a lipid monolayer undergoes during compression and expansion. For my proposed work, Langmuir trough isotherms will be obtained to examine the thermodynamic and structural properties of the aqueous/monolayer/vapor interface in model pulmonary systems.

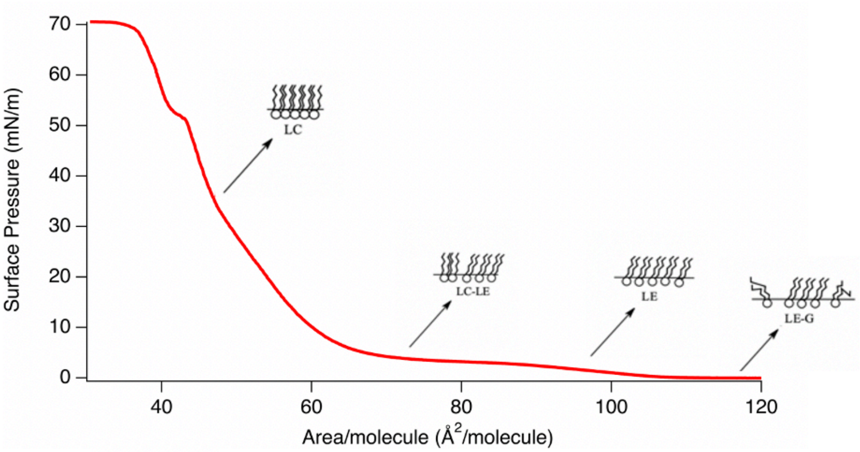

Figure 1.3. Langmuir isotherm of DPPC with phase regions (55 Å^2/molecule).[108]

A compression isotherm (Figure 1.3) measures surface pressure as a function of molecular area. Surface pressure (Π) is obtained by taking the difference between the surface tension of Millipore water (γ_0) and the surface tension of the system (γ) as seen in Equation 1.1. Millipore water has a surface tension of 72.5 mN/m at 23ºC.[13] The collapse pressure, where a Langmuir monolayer is compressed beyond its stability limit, for DPPC is also 72.5 mN/m. By taking the difference of the surface tensions of Millipore water and DPPC on Millipore, we determine the system's surface pressure.

$$\Pi = \gamma_0 - \gamma \quad \text{(Eqn. 1.1)}$$

At large areas per molecule (when the barriers are far apart), the lipid molecules are dispersed as a 2-dimensional gaseous (G) phase – the hydrophobic tails of the lipid are randomly oriented and in contact with the water surface but have little contact with each other. As the lipid monolayer is compressed into a liquid-expanded (LE) phase (shown on the right side of Figure 1.3), the hydrophobic tails of the lipids come into contact with each other and lift from the water surface but remain largely disordered and fluid. Further compression of the monolayer leads to a first-order transition into a liquid-condensed (LC) phase (when the barriers are close together). In single component lipid monolayers (i.e. DPPC), the LE-LC coexistence phase is delineated by a plateau in the isotherm that extends from approximately 85 Å^2/molecule to 60 Å^2/molecule shown in Figure 1.3.[108-110]

Given that PHFs are weakly surface active, we can determine excess free energies of mixing (G_{ex}). Free energies of mixing can be determined by using Equations 1.2-1.5. In Equation 1.2, A_n is the area per monolayer of molecule n, and χ_n is the mole fraction of molecule n. With Equation 1.2 we can determine the average area (A_{ex}) and use this value in Equation 1.3 where excess free energy (G_{ex}) is the area under the curve that plots excess area per molecule with respect surface tension. In Equation 1.4, free energy of mixing is represented as the sum of the free energy of an ideal monolayer and the excess free energy of mixing. Equation 1.5 can be used to find the free energy of an ideal monolayer.

$$\mathrm{A_{ex}} = \mathrm{A_{12}} - (\chi_1 \mathrm{A_1} + \chi_2 \mathrm{A_2}) \text{ (Eqn. 1.2)}$$

$$\Delta \mathrm{G_{ex}} = \int_0^{\pi} \mathrm{A_{ex}} d\pi \text{ (Eqn. 1.3)}$$

$$\Delta \mathrm{G_{mix}} = \Delta \mathrm{G_{id}} + \Delta \mathrm{G_{ex}} \text{ (Eqn. 1.4)}$$

$$\Delta \mathrm{G_{id}} = \mathrm{k_b T}(\chi_1 \ln \chi_1 + \chi_2 \ln \chi_2) \text{ (Eqn. 1.5)}$$

In order to study the behavior of PHFs with DPPC monolayers, studies will focus on more loosely packed lipid films (~55 Å^2/molecule) and densely packed lipid films (~ 40 Å^2/molecule). At lower surface coverages (~55 Å^2/molecule) lipid films have vacant, interstitial spaces so we hypothesize that PHFs should have a more significant impact on the DPPC monolayer structure and organization in this regime than for higher surface coverages (~40 Å^2/molecule). The Langmuir trough isotherms will allow us to extract information about thermodynamic and structural properties at the aqueous/monolayer/vapor interface. Because DPPC forms monolayers with LE-LC coexistence phases, compression isotherms of PHFs with DPPC will address how PHFs affect a DPPC monolayer's thermodynamic properties by showing disruption in ordering of the DPPC film with the addition of particulates. Data from these experiments will allow us to determine if a DPPC monolayer's structure and organization, at a given area with the inclusion of PHFs, is impacted post-compression.[111] We will learn about changes in lipid phase behavior (lipid arrangement), surface tension, changes in collapse pressure, surface coverage, and free energies of adsorption when PHFs are introduced to a DPPC film.

1.4.1.2 Second Harmonic Generation Spectroscopy. Resonance enhanced second harmonic generation (SHG) spectroscopy is a second order nonlinear optical spectroscopic technique that is inherently surface specific. Shortly after the discovery of the first Ruby laser, nonlinear optical effects were first reported [112]. Because linear polarization could no longer account for the effects of intense, coherent optical radiation (i.e. a laser), nonlinear optical effects were explained by expanding the expression for the polarization, $\mathrm{P(t)} = \varepsilon_0 \chi^{(1)} \mathrm{E(t)}$, in a power series to contain more than the linear contribution (Equation 1.6).

$$\mathrm{P(t)} = \varepsilon_0[\chi^{(1)}\mathrm{E(t)} + \chi^{(2)}\mathrm{E(t)}^2 + \chi^{(3)}\mathrm{E(t)}^3 + \ \ldots \text{ (Eqn. 1.6)}$$

The second order nonlinear optical polarization, also known as $\mathrm{P}^{(2)}$, is the origin of second order nonlinear optical effects. $\mathrm{P}^{(2)}$ is equal to the second order nonlinear optical susceptibility times the incident electric field squared, $\mathrm{P}^{(2)}(\mathrm{t}) = \varepsilon_0 \chi^{(2)} \mathrm{E(t)}^{(2)}$. The second order nonlinear optical susceptibility, also known as $\chi^{(2)}$, is a third rank tensor which means by definition, $\chi^{(2)}_{\mathrm{ijk}} = -\chi^{(2)}_{\mathrm{-i-j-k}}$, a statement that is only true in spatially isotropic materials if $\chi^{(2)} = 0$. For this reason, the only systems in which $\chi^{(2)} = 0$ are those with an inherent anisotropy (i.e. interfaces). This unique attribute of $\chi^{(2)}$ enables for one to detect signal from molecules at intrinsically anisotropic interfaces.

When two laser beams with different frequencies are incident on a medium with a non-zero nonlinear susceptibility ($\chi^{(2)} \neq 0$), substitution into the expression for the second order nonlinear polarization ($P^{(2)}(t)$) gives Equation 1.7.

$$P^{(2)}(t) = \varepsilon_0\chi^{(2)}[(E_1^2e^{-i(2\omega_1)t} + E_2^2e^{-i(2\omega_2)t} + c.c) + 2E_1E_2(e^{-i(\omega_1+\omega_2)t} + e^{-i(\omega_1-\omega_2)t} + c.c) + 2(E_1^2 + E_2^2)] \quad \text{(Eqn. 1.7)}$$

The frequency components in Equation 1.7 are comprised of signals from three separate second order nonlinear optical techniques: SHG, SFG, and difference frequency generation (DFG). Of these three second order optical nonlinear effects, two are useful for spectroscopic experiments at interfaces: SHG and SFG.

In SHG, two incident photons of frequency ω couple to produce a single SH photon of frequency of 2ω. SHG is typically performed with incident photons in the visible region, generating photons in the ultraviolet. When either the incident or the generated SH light is resonant with an electronic transition of molecules present at the interface, the SH signal experiences a resonant enhancement, making resonance enhanced SHG a useful tool to study electronic structure of interfacial molecules and materials, as well as surface behavior.

SFG will be discussed in further detail below, but briefly it is similar in principle to SHG. In SFG there are two photons of different frequencies, ω_1 and ω_2, which combine to give a single photon of frequency ω_3 ($\omega_3 = \omega_1 + \omega_2$). SFG requires that the two pulsed laser beams, ω_1 and ω_2, overlap at the sample both spatially and temporally, as well as necessitating that at least one medium making up the interface be transparent to both visible and IR light. Similar in principle to SHG, when the IR frequency in SFG is resonant with a vibrational transition of molecules present at the interface, SF signal enhancement occurs. This SFG signal enhancement allows for detailed structural information of interfacial molecules.

As the experiments in this thesis were interested in the water – air interface, both SHG (complementary electronic spectroscopy to fluorescence) and SFG (complementary vibrational spectroscopy to Fourier-transform infrared spectroscopy (FTIR)) were used.

Not only is $\chi^{(2)}$ surface specific due to its behavior with respect to inversion, but elements in the $\chi^{(2)}$ tensor are also molecularly specific. The $\chi^{(2)}$ tensor consists of two components, a resonant (R) portion and a nonresonant (NR) portion (Equation 1.8).

$$\chi^{(2)} = \chi^{(2)}_{\mathrm{NR}} + \chi^{(2)}_{\mathrm{R}} \text{ (Eqn. 1.8)}$$

The nonresonant portion ($\chi^{(2)}_{\mathrm{NR}}$) of $\chi^{(2)}$ in the experiments described in Chapter 3 is small and therefore fit to a constant. The resonant portion ($\chi^{(2)}_{\mathrm{R}}$) of $\chi^{(2)}$ is the orientational average over the molecular hyperpolarizability times the total number of surface molecules as shown in Equation 1.9, where β is given by $\beta = \frac{A}{\omega_0 - \omega - i\Gamma}$.

$$\chi^{(2)}_{\mathrm{R}} = N\langle \beta_{i,j,k} \rangle \text{ (Eqn. 1.9)}$$

When breaking down the components of β in Equation 1.9, A is a constant related to the one- and two-photon absorption resonances of molecules at the interface [113], ω_o is the resonant frequency of a transition, ω is the frequency of incident light, and Γ is the linewidth associated with a transition.

To conduct SHG experiments, a Coherent Libra-HE Ti:sapphire chirped pulse regenerative amplifier (1 kHz repetition rate, 3.4 W average power, 800 nm, 85 fs pulses), coupled to an optical parametric amplifier (Coherent OperA Solo, FWHM 10 nm) to create the wavelengths needed to perform SHG experiments, was used. To prevent from oversaturating the detector, neutral density filters were used, when necessary, to reduce the intensity of the light. The beam from the Coherent OPerA Solo, OPA, was set to a specific wavelength and was focused on the sample. The fundamental beam was then filtered out of the reflected light from the sample, and the SH photons were collected by a photomultiplier tube (PMT), which was coupled to a monochrometer to discern relevant wavelengths.

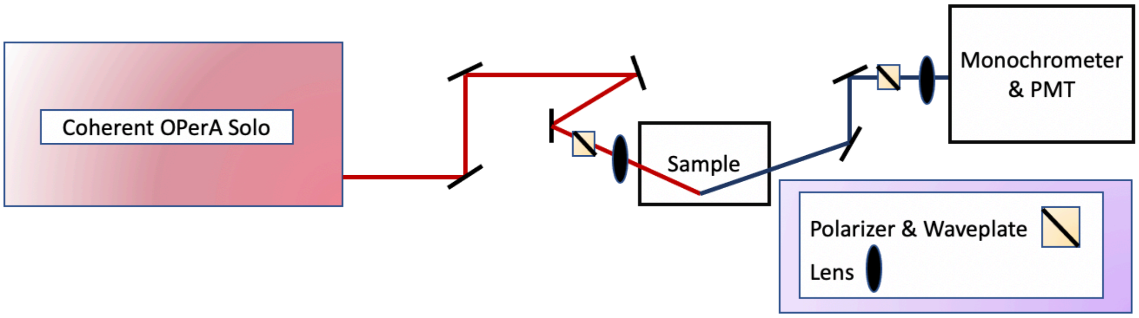

Figure 1.4. Experimental geometry of the SHG instrument.

To study changes in surface behavior at the interface with the addition of PHFs, studies will focus varying PHF concentrations and bulk-phase concentrations (varying NaCl concentrations). The SHG data will allow us to extract information about the optical behavior of PHFs with varying solution-phase ionic strength at the aqueous/air interface.

1.4.1.3 Vibrational Sum Frequency Generation Spectroscopy. VSFG is a surface-specific, second-order nonlinear optical technique commonly used to study molecular structure at liquid interfaces [53]. My research will use VSFG to examine lipid structure and orientation in adsorbed monolayers with the inclusion of PHFs. VSFG is both surface and molecularly specific, meaning that surface vibrational spectra of liquid interfaces can be used to learn about lipid conformation and orientation. Based on the polarization dependence and relative intensities of different features, I will measure how PHF adsorption induces changes in lipid conformation and average orientation [53]. These experiments will be performed with lipid monolayers having different surface coverages and different compositions.

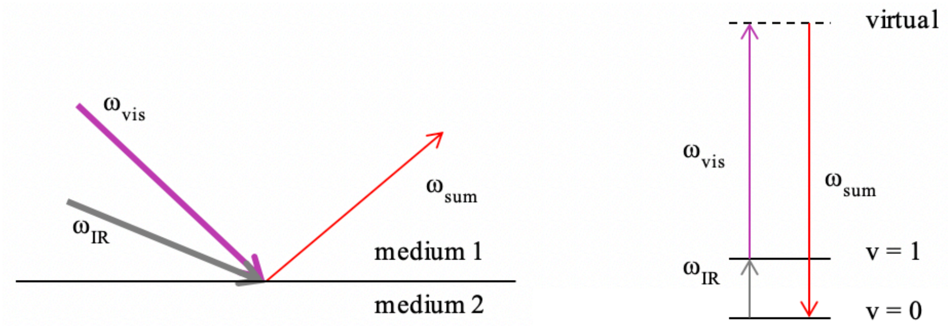

Figures 1.5. Schematic of an SFG process at an interface that is detected in the reflection direction (left) & Jablonski diagram of SFG process with ω_{IR} at resonance with a vibrational transition (right) [53].

In a VSFG experiment two oscillating electromagnetic fields ($\vec{E}^i$) at different frequencies (ω_{Vis} and ω_{IR}), overlap both spatially and temporally on a surface of interest

(Equation 1.10). The two fields couple through the 2nd order susceptibility tensor ($\chi^{(2)}$) to generate a third field equal in frequency to the sum of the first two ($\omega_{sum} = \omega_{Vis} + \omega_{IR}$). For an SFG process, the 2nd order polarization ($\vec{P}$) that generates the output is given by Equation 1.11. $\chi^{(2)}$ describes the relationship between two applied electric field vectors ($\vec{E}^1$ and $\vec{E}^2$) and the resultant vector ($\vec{P}^{(2)}$) [114]. The 2nd order polarization (Equation 1.11) can then be expanded into Equation 1.12 where it consists of four components, including the SFG portion. The red pieces are DC fields that correspond to THz frequencies, the green pieces comprise the second harmonic generation (SHG) portion, the blue piece is the difference frequency generation (DFG), and the violet piece is the sum frequency generation (SFG) [114].

$$\vec{E}^{i} = \vec{E}^{1}\cos\omega_1 t + \vec{E}^{2}\cos\omega_2 t \text{ (Eqn. 1.10)}$$

$$\vec{P}^{(2)} = \epsilon_0\chi^{(2)}\left(\vec{E}^{1}\cos\omega_1 t + \vec{E}^{2}\cos\omega_2 t\right)^2 \text{ (Eqn. 1.11)}$$

$$\vec{P}^{(2)} = {\vec{E}^{1}}^{2} + {\vec{E}^{2}}^{2} + \vec{E}^{1^2}\cos 2\omega_1 t + \vec{E}^{2^2}\cos 2\omega_2 t + \frac{1}{2}\vec{E}^{1}\vec{E}^{2}\cos(\omega_1 - \omega_2)\,t + \frac{1}{2}\vec{E}^{1}\vec{E}^{2}\cos(\omega_1 + \omega_2)\,t \text{ (Eqn. 1.12)}$$

$$I(\omega_3; \omega_1, \omega_2) \propto \left|\chi^{(2)}\right|^2 I_1(\omega_1) I_2(\omega_2) \text{ (Eqn. 1.13)}$$

Because VSFG is a second-order nonlinear process, it depends on the 2nd order susceptibility $\chi^{(2)}$ [114]. $\chi^{(2)}$ is a third rank tensor and is antisymmetric with respect to inversion. In isotropic media, this property requires that all elements of the $\chi^{(2)}$ tensor are zero. When an interface between two materials or centrosymmetric media is present, inversion symmetry breaks and a VSFG signal is generated, which demonstrates that

VSFG spectra represent a thin layer of molecules where only the surface is being probed, and when there is a net polar orientation, a signal is generated [115]. With the 2nd order susceptibility ($\chi^{(2)}$), the intensity (I) of the output beam can be calculated using Equation 1.13, where ω_1 is the visible frequency, ω_2 is the IR frequency, and ω_3 is the sum frequency ($\omega_3 = \omega_1 + \omega_2$).

$\chi^{(2)}$ has both a resonant (χ_r) and a non-resonant (χ_{nr}) contribution as shown in Equation 1.14. χ_r results from the vibrational modes while χ_{nr} is from electronic responses. The resonant piece is often described with a Lorentzian function (Equation 1.15) where the amplitude term is a product of the IR and Raman transition dipole moments (Equation 1.16) and χ_r indexes all of the vibrational modes contributing to the resonant part of the 2nd order susceptibility at a given frequency [115]. Equations 1.15 and 1.16 require that any transition observed in a VSFG spectrum be both IR and Raman active [116]. Equation 1.14 can be substituted into Equation 1.15 to obtain a general expression for the second order susceptibility, Equation 1.17. Equation 1.17 is used to model SFG output. When the frequency of a vibrational mode of a surface molecule is matched by the SFG, the output intensity is resonantly enhanced [116].

$$\chi = \chi_{nr} + \chi_r \text{ (Eqn. 1.14)}$$

$$\sum_q \frac{A_q}{\omega_2 - \omega_{0_q} + i\Gamma_q} \text{ (Eqn. 1.15)}$$

$$A_q = \langle i|\mu|v\rangle \left\langle v\left|\frac{\delta\alpha}{\delta q}\right|i\right\rangle \text{ (Eqn. 1.16)}$$

$$\chi = |\chi_{nr}|e^{i\phi} + \sum_q \frac{A_q}{\omega_2 - \omega_{0_q} + i\Gamma_q} \text{ (Eqn. 1.17)}$$

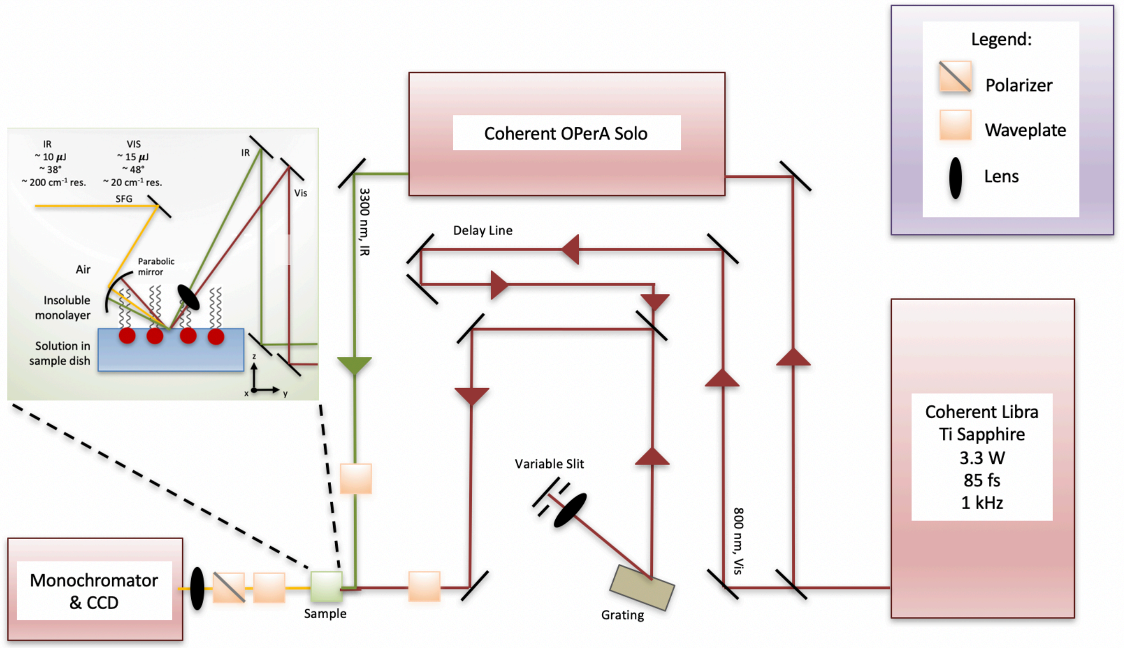

Figure 1.6. MSU Walker Research Group SFG laser diagram.

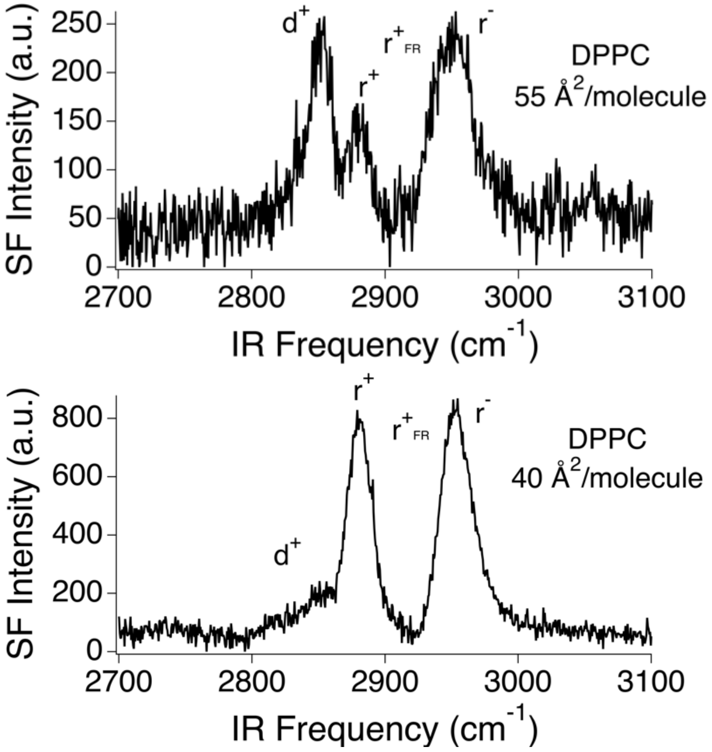

Figure 1.7. Vibrational spectra of DPPC in the CH stretch region with SSP polarization at 55 Å^2/molecule (top) and 40 Å^2/molecule (bottom).

With polarization analysis we can determine the relative orientation of molecules at the surface (i.e. facing parallel to the surface or angled off the surface) [116, 117]. Different polarization combinations sample different non-zero elements of the $\chi^{(2)}$tensor. With $\chi^{(2)}$, the intensity of the output beam can be calculated using Equation 1.13 and a ratio of intensities (i.e. methyl intensities to methylene intensities) can be used to determine tilt angle. I will use SSP ($S_{sum}S_{vis}P_{IR}$) and SPS ($S_{sum}P_{vis}S_{IR}$) polarization combinations where SSP samples normal modes with IR transition moments aligned along the surface normal and the SPS combination probes vibrational modes with transition moments parallel to the surface. With VSFG, we will be able to look at microscopic changes occurring at the interface and get direct information about orientation distribution of DPPC with the inclusion of PHFs.

The VSFG in our lab is best suited for measuring spectra in the CH stretching region (2700-3100 cm^{-1}). Figure 8 is a vibrational spectrum of DPPC in the CH stretch region where “r” denotes vibrations associated with the methyl group of DPPC monomers and “d” describes vibrations associated with methylene groups. The “+” indicates a symmetric stretch (SS) and a “-” indicates an antisymmetric stretch (AS). d^+ at 2846 cm^{-1} corresponds to a CH_2 SS, r^+ at 2870 cm^{-1} corresponds to a CH_3 SS, r^- at 2952 cm^{-1} corresponds to an out-of-plane CH_3 AS, r^- at 2962 cm^{-1} corresponds to an in-plane CH_3 AS, and r^+_{FR} at 2930 cm^{-1} corresponds to a CH_3 Fermi resonance interaction [60, 118]. The $\frac{r^+}{d^+}$ ratio of methyl to methylene intensities is a useful qualitative measure of conformational order in the DPPC monolayer [118]. Based on the features that appear in VSFG spectra having different polarizations, we can infer details about interfacial molecular composition as well as molecular orientation. Because our current setup probes CH stretches, we will not see any VSFG signal from PHFs, but we will see how the signal for DPPC changes with the addition of PHFs.

To study changes in structure and orientation distribution of the interface with the addition of PHFs, studies will focus on loosely packed lipid films (~55 Å^2/molecule) and densely packed lipid films (~ 40 Å^2/molecule). In lower surface coverage (~55 Å^2/molecule) there is more surface area that is unoccupied by the lipid film so PHFs should have a more significant impact on the DPPC monolayer than for higher surface coverage (~40 Å^2/molecule). The VSFG vibrational spectra will allow us to extract information about the changes in orientation of the lipid monolayer with the addition of PHFs at the aqueous/monolayer/vapor interface.

1.4.1.4 Spectroscopic Ellipsometry. SE is increasingly being used for studying biological systems and characterizing surface layers[65, 66, 119-122]. Unlike standard ellipsometry, SE allows you to measure two ellipsometric angles (Ψ and Δ) that provide information about the sample at each wavelength over a wide spectral range [123]. SE is a real-time site-specific surface or interface technique where the ratio of reflection of p- versus s-polarized light is compared to a model to learn the optical constants of materials [124]. SE is used to observe macroscopic properties of a sample such as thickness, refractive index, and optical density, allowing us to learn about ideal versus non-ideal mixing in terms of PHF-lipid film interactions.

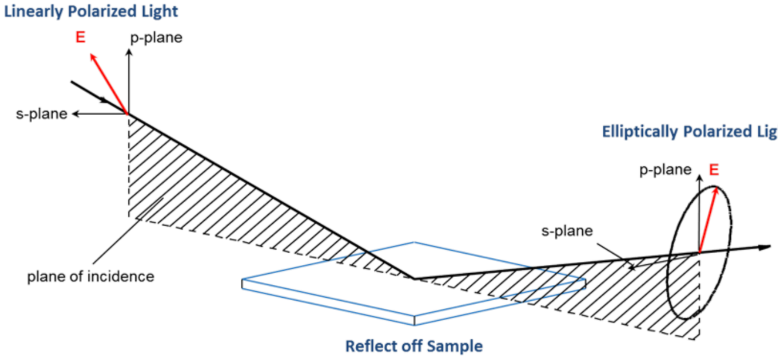

Figure 1.8. Ellipsometry schematic [125].

In SE, linearly polarized incident light (two orthogonal light waves in-phase) changes to elliptically polarized light (combination of orthogonal waves of arbitrary amplitude and phase) after reflection off of a sample. Elliptical polarization is detected by placing an analyzer in front of the detector, and it can be rotated to select out a certain projection onto an x-y axis. The amplitude (Ψ) of a sine wave is detected, which provides information about the $\tan^2 \phi_0$ term, ϕ_0 being the known angle of incidence (Equation 17), and the phase (Δ) of the sine wave is detected, which provides information about the phase shift. The ratio of p- versus s-polarized light (ρ, also known as the complex reflectance ratio) can be found using Equation 1.18. In order to find ρ, the amplitude component (Ψ, Equation 1.19) and the phase difference (Δ, Equation 1.20) need to first be determined. Ψ and Δ are ellipsometric angles that provide information about the properties of the sample. $\tan \Psi$ is equal to the ratio of the intensities (or absolute magnitudes) of the p- and s-polarized light. Δ is the difference in phase between the p- and s-polarized light. Once Ψ and Δ are obtained, one can determine the complex reflectance ratio (ρ) and use ρ to derive the optical constants and other components of your sample using Equation 1.21, where ε is the relative permittivity (aka dielectric function), χ is the electric susceptibility, n is index of refraction, k is the extinction coefficient, the "n+ik" term is referred to the complex refractive index, and ϕ_0 is the known angle of incidence.

$$\rho = \frac{R_p}{R_s} = \tan(\Psi)\exp(i\Delta) \text{ (Eqn. 1.18)}$$

$$\tan\Psi = \frac{|R_p|}{|R_s|} \text{ (Eqn. 1.19)}$$

$$\Delta = \Delta_p - \Delta_s \text{ (Eqn. 1.20)}$$

$$\varepsilon = 1 + \chi = (n + ik)^2 = \sin^2\phi_0 + \sin^2\phi_0 + \tan^2\phi_0 \left[\frac{1-\rho}{1+\rho}\right]^2 \text{ (Eqn. 1.21)}$$

To study DPPC monolayer thickness, surface reflectivity and other optical constants of the aqueous/monolayer/vapor interface in the presence and absence of PHFs, studies will focus on loosely packed lipid films(~55 Å^2/molecule) and densely packed lipid films (~ 40 Å^2/molecule). At lower surface coverages (~55 Å^2/molecule) I expect that PHFs should have a more significant impact on DPPC monolayer structure than when adding PHFs at higher surface coverage (~40 Å^2/molecule). SE allows for real-time characterization of our interface with spectral resolution of 2 nm, spatial resolution of ~20-400 μm and depth penetration between 1 Å to 50 μm. We will focus the beam on a spot size on the surface and will be able to determine how surface reflectivity and monolayer thickness change with varying PHF concentration.

1.5 Organization of Thesis

Note that Chapters 2-4 are prepared in manuscript format for future submission. Due to their publication (or anticipated publication) in literature, information in the introductions, materials, and methods sections of these chapters may appear in several different sections of this dissertation. Research described in this dissertation is organized as follows:

Chapter 2: Surface Activity and Aggregation Behavior of Polyhydroxylated Fullerenes in Aqueous Solutions

Chapter 2 describes the surface activity and aggregation behavior of PHFs in bulk aqueous solutions (varying NaCl concentrations) at the water/air interface.

Chapter 3: Carbon Nanoparticle-Induced Organizational Changes in Lipid Monolayers at Water – Air Interfaces

Chapter 3 describes how PHFs in Millipore water induce organizational changes in DPPC monolayers at the water/air interface.

Chapter 4: Carbon Nanoparticle-Induced Changes to Lipid Monolayer Structure at Air – Water Interfaces. 2. Ionic Strength Effects

Chapter 4 describes how the addition of salt impacts PHF-DPPC interactions, specifically organizational changes in DPPC monolayers at the water/air interface.

Chapter 5: Conclusions and Future Directions

Chapter 5 includes the summary of research described in Chapters 3-5 and includes a discussion on further experiments that should be performed to continue this project.

CHAPTER TWO

SURFACE ACTIVITY AND AGGREGATION BEHAVIOR OF POLYHYDROXYLATED FULLERENES IN AQUEOUS SOLUTIONS

Contribution of Authors and Co-Authors

Manuscript in Chapter 2:

Author: Nida Shaikh

Contributions: Collected and analyzed all experimental data and authored manuscript

Author: Samuel P. Bernhard

Contributions: Collected and analyzed experimental data and authored supplemental information

Co-Author: Robert A. Walker

Contributions: Assisted with data analysis, writing, and editing manuscript

Manuscript Information

Nida Shaikh, Samuel P. Bernhard, and Robert A. Walker

Langmuir

Status of Manuscript:
____ Prepared for submission to a peer-reviewed journal
_X__ Officially submitted to a peer-reviewed journal
____ Accepted by a peer-reviewed journal
____ Published in a peer-reviewed journal

Publisher: American Chemical Society
Date of Submission: 25-04-2022
Date Accepted: D M Y
Volume __, M Y, ####-####
DOI: ###

CHAPTER TWO

SURFACE ACTIVITY AND AGGREGATION BEHAVIOR OF POLYHYDROXYLATED FULLERENES IN AQUEOUS SOLUTIONS

2.1 Introduction

Polyhydroxylated fullerenes (PHFs) - also called ‘fullerols’ or ‘fullerenols’ – comprise a family of soluble carbon particulates that have been targeted for applications as diverse as drug delivery, metal nanoparticle catalysis and agricultural pest control.[23-29] In part, this interest in PHFs as a functional carbon nanoparticle is driven by its ability to generate reactive oxygen species when irradiated with UV light.[30, 31] PHFs have also been associated with harmful environmental and physiological outcomes, including enhanced copper release from ores and measurable phototoxicity in human epithelial cells.[32-34] Despite this intense interest in PHF properties and applications, simple questions about PHF behavior in aqueous solution remain unanswered. Specifically, accurate, quantitative descriptions of PHF surface activity and aggregation tendencies remain tentative and incomplete. Findings reported in this work show that PHFs are, in fact, weakly surface active and that their surface activity depends on solution phase ionic strength, supporting the premise that surface activity and solution phase aggregation are inextricably linked.

PHFs consist of C_{60} fullerenes functionalized with a variable number ($n = 12 - 40$) of hydroxyl groups, These carbon nanoparticles are highly soluble in aqueous solution, with solubilities as high as 58.9 g/L having been reported.[35, 36] PHFs are known to behave nonideally at higher concentrations, forming aggregates that can be detected by dynamic light scattering.[35-37] PHF behavior at lower concentrations is less well characterized, although most reports generally assume – either explicitly or implicitly – that PHF solutes are monomers in aqueous solutions having concentrations ≤ 0.1 mg/ml.[126, 127] Despite the large number of hydroxyl groups decorating the PHF surface, not all hydroxyl groups contribute to aqueous solubility. Numerous experimental and modeling studies report that hydroxyl groups tend to cluster on the fullerene surface where they can be stabilized internally through intramolecular hydrogen bonding.[38-49] This asymmetry complicates efforts to understand PHF chemistry in aqueous solution and at aqueous interfaces. Simple models describing properties based on functional group additivity will be less effective because not all hydroxyl groups contribute equally to stabilization in solution. Furthermore, clustering of hydroxyl groups on one side of a fullerene structure leaves PHFs with hydrophobic surface areas that resemble engineered Janus particles.[128, 129] This amphiphilic structure enhances the likelihood of aggregate formation in water[50] and makes PHF surface activity more likely.[51, 52]

Resolving questions about PHF behavior in aqueous solution and PHF surface activity also has impact beyond advancing the community's understanding of this specific class of carbon-based materials. Fullerenes are often used surrogates for more heterogeneous carbon black aerosols.[130-132] Although carbon particulates often have extremely hydrophobic character when first generated, they become more hydrophilic as they age in the environment and become oxidized.[133-135] Consequently, identifying PHF properties in aqueous environments marks a first step toward understanding how heterogeneous carbon aerosols affect the properties of atmospheric and terrestrial water surfaces and bulk solution chemistry.[136-138]

Findings reported below result from studies examining PHF surface activity and PHF aggregation as a function of bulk concentration and solution-phase ionic strength. The data imply that PHF aggregation in bulk solution impacts PHF adsorption to aqueous/vapor interfaces and that PHFs aggregate at bulk concentrations much lower than previously acknowledged. Surface tension data show PHFs to be modestly surface active, forming monolayers with a terminal surface coverage of 7.50×10^{13} /cm^2 (130 Å^2/molecule). Conductivity measurements confirm that the PHFs are charged. Surface activity is confirmed with second harmonic generation measurements.

2.2 Experimental Methods

2.2.1 Materials

The carbon nanoparticles used were commercially available polyhydroxylated fullerene powder ($C_{60}(OH)_n \cdot (H_2O)_m$, average n = 20-24 measured by size exclusion chromatography; American Elements, Los Angeles, CA). Sodium chloride was purchased from Sigma-Aldrich (99.999% purity; St. Louis, MO). All chemicals were used as received without further purification. Water used in the aqueous experiments was nanopure, from a Millipore filtration system, and had a resistivity of 18.2 MΩ and a surface tension of 72.5 mN/m at 23 °C.

2.2.2 Preparation of Samples

Polyhydroxylated fullerene stock solutions (0.5 mg/mL) were prepared in Millipore water and in solutions containing 50 mM NaCl and 500 mM NaCl. All solutions were sonicated for 5 min to ensure complete dissolution. The polyhydroxylated fullerene stock solutions were used to prepare aqueous PHF solutions having concentrations of 0.5, 0.125, 0.06 0.03, 0.0075, and 0 mg/mL.

2.2.3 Surface Tension (Terminal Surface Coverages)

Surface tension measurements were carried out using methods described previously.[62, 64, 66, 139] Briefly, a NIMA Langmuir trough (Model 302LL) equipped with a NIMA PS4 pressure sensor and a microprocessor interface 104 was used to perform measurements. Paper Wilhelmy plates (Brown Waite Engineering) were used to measure surface tension. Surface pressure (Π) was measured as a function of concentration. The surface pressure is the difference between the surface tension of the underlying neat liquid subphase (γ_0) and the surface tension resulting from the subphase and surfactant monolayer (γ), PHF solutions in this case (Equation 2.1).

$$\Pi = \gamma_0 - \gamma \text{ (Eqn. 2.1)}$$

By using the relationship in Equation 2.1 we obtain a concentration versus surface pressure plot. Treating adsorbed PHF solutes as soluble surfactants, we then used the Gibbs adsorption equation to determine limiting surface coverages (Equation 2.2):[140]

$$\Pi A = n * k * T * \ln{[C]} \text{ (Eqn. 2.2)}$$

$$\Gamma = \frac{d\Pi}{dln[C]} * \frac{1}{kT} \text{ (Eqn. 2.3)}$$

where Γ is the surface excess concentration. Equation 2.2 can be simplified to Equation 2.3 to approximate Γ, or surface excess, where $\frac{d\Pi}{dln[C]}$ is the slope of steepest ascent determined from a PHF concentration versus surface pressure plot.

2.2.4 Second Harmonic Generation (SHG)

SHG experiments were performed to assess if PHF surface activity measured in the surface tensions measurements manifested in the sample's optical properties. In these experiments, the incident wavelength was set to 690 nm and the SHG signal was detected at 345 nm. This combination of wavelengths leveraged the broad electronic resonance shown by PHFs in aqueous solution. This resonance increases at short wavelengths. A PHF UV-vis absorption spectrum is shown in Figure 2.3. Details of the experimental assembly have been described previously.[59, 61, 141, 142] Briefly, ~3.4 W from a Ti-Sapphire regenerative amplifier (Libra-HE, Coherent, 85 fs pulses, 1 kHz repetition rate, 800 nm) was coupled to a visible optical parametric amplifier (Coherent OPerA Solo) and focused on the sample. Incident visible light was attenuated to below 2 mW with neutral density filters before it reached the sample, if and when necessary. The second harmonic signal was collected using a photomultiplier tube and photon counting electronics. Data for each sample at the wavelength of interest were collected over 3-5 separate 10 s intervals, background corrected, and then averaged.

The intensity of the collected second harmonic signal is proportional to the square of the second order polarizability, P^2 (Equation 2.4), in Equation 2.5, where:

$$P^{(2)} = \chi^{(2)} : E(\omega)E(\omega) \text{ (Equation 2.4)}$$

$$I(2\omega) \propto \left|P^{(2)}\right|^2 = \left|\chi^{(2)}\right|^2 I(\omega)^2$$ (Equation 2.5)

SHG's surface specificity stems from the surface's second order susceptibility, $\chi^{(2)}$, a third rank tensor whose elements must be antisymmetric with respect to inversion (Equation 2.6):

$$\chi^{(2)}_{i,j,k} = -\chi^{(2)}_{-i,-j,-k}$$ (Equation 2.6)

While this condition forbids SHG from originating from bulk solution, solutes adsorbed to interfaces are subject to surface anisotropy and can become SH active. Finally, we note that $\chi^{(2)}$ itself can be expressed as the sum of resonant (R) and nonresonant (NR) contributions (Equations 2.7 and 2.8)

$$\chi^{(2)} = \chi^{(2)}_{NR} + \chi^{(2)}_{R}$$ (Equation 2.7)

$$\chi^{(2)}_{R} = N\langle\beta_{abc}\rangle = N\sum_{k,e}\frac{A_{k,e}}{(\omega_{gk}-\omega_0-i\Gamma)(\omega_{eg}-2\omega_0+i\Gamma)}$$ (Equation 2.8)

where N refers to the number of surface species; β_{abc} is the orientationally averaged hyperpolarizability; $A_{k,e}$ is an amplitude term related to the transition dipoles between the ground (g), intermediate (k) and excited (e) states, ω_0 is the frequency of the incident light and Γ is the ground-excited state transition linewidth. The resonance condition for SHG requires that an SH response originate from an electronic transition that is both 1- and 2-photon allowed.[113]

2.3 Results

2.3.1 PHF Surface Activity

Surface tension measurements were used to assess PHF surface activity. Figure 2.1 shows surface pressure data for PHF solutions as a function of the natural log of PHF concentration where a concentration of 1.0 mg/ml has been chosen as the reference concentration. Measurements were made using solutions having three different ionic strengths: 0, 0.05, and 0.50 M (where ionic strength was controlled by addition of NaCl).

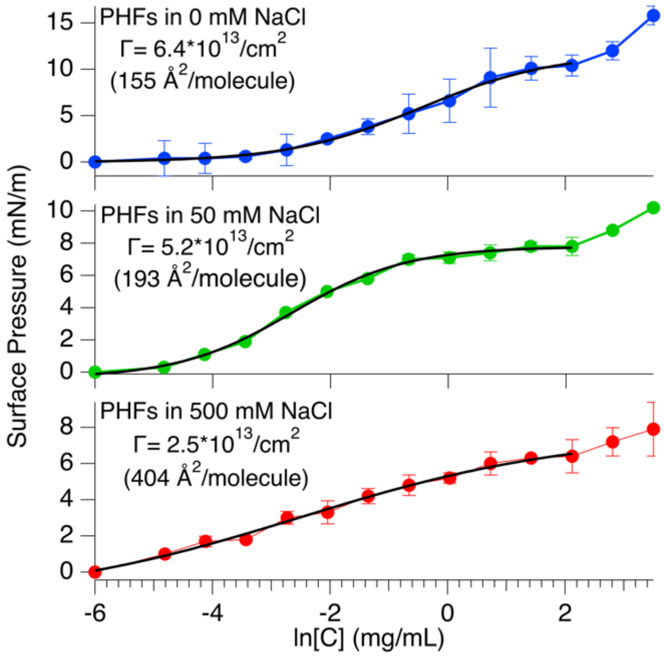

Figure 2.1. Terminal surface coverages of PHFs in 0 mM NaCl (neat Millipore water) (top). Terminal surface coverages of PHFs in 50 mM NaCl (middle). Terminal surface coverages of PHFs in 500 mM NaCl (bottom). Black lines are empirical fits of the data to a sigmoidal function and are used to calculate slopes at different bulk solution PHF concentrations

According to Equation 2.3, the slope of steepest ascent provides a direct measure of the terminal PHF surface excess concentration.[140] The data show PHFs are, in fact, surface active despite their high aqueous solubility. Specifically, PHFs have terminal surface coverages of 155 Å^2/molecule in 0 mM NaCl (neat Millipore water), 193 Å^2/molecule in 50 mM NaCl, and 404 Å^2/molecule in 500 mM NaCl with an uncertainty of ~±5-10 Å^2/molecule. Surface tension data show that in Millipore water, a concentration of ~0.5 mg/ml is required to reach terminal surface coverage but adding NaCl to solution dramatically lowers the bulk PHF concentration required to reach (lower) terminal surface coverages. Surface coverages are reported in Table 2.1.

Table 2.1. PHF surface coverages (in both molecules/cm^2 and Å^2/molecule) in 0, 50, and 500 mM NaCl as a function of PHF concentration.

PHF concentration (mg/mL)	**0 mM NaCl**		**50 mM NaCl**		**500 mM NaCl**	
	(/cm^2)	**Å^2**	**(/cm^2)**	**Å^2**	**(/cm^2)**	**Å^2**
Terminal coverage	$6.4*10^{13}$	155	$5.2*10^{13}$	193	$2.5*10^{13}$	404
0.519	$6.4*10^{13}$	155	$5.2*10^{13}$	193	$2.5*10^{13}$	404
0.260	$5.1*10^{13}$	194	$5.2*10^{13}$	193	$2.5*10^{13}$	404
0.130	$3.7*10^{13}$	273	$5.2*10^{13}$	193	$2.5*10^{13}$	404
0.063	$2.3*10^{13}$	434	$5.1*10^{13}$	196	$2.4*10^{13}$	408
0.033	$1.4*10^{13}$	705	$4.1*10^{13}$	239	$2.3*10^{13}$	428
0.008	$4.3*10^{12}$	≥2200	$1.5*10^{13}$	664	$1.8*10^{13}$	549

Previous studies have proposed that PHFs form aggregates in aqueous solution.[122] Additional work has reported that dissolved NaCl limits PHF aggregation through screening effects and reducing the PHF hydrodynamic diameter by up to 50%.[122, 143, 144] Data in Figure 2.1 and Table 2.1 support the PHF aggregation hypothesis. They also confirm the surface activity of PHFs and support claims that PHFs also aggregate at the air – water interface.[119-121] In pure water surface pressure data show the highest surface coverage, while increasing ionic strength reduces terminal PHF surface coverage by a factor of three. Fitting these data from Figure 2.1 lead to adsorption energies of -29 (±7) (0 mM NaCl), -26 (±7) (50 mM NaCl), and -21 (±7) (500 mM NaCl) kJ/mole [102] (see Figure SI-2.5).

Details about PHF structure can be used to rationalize PHF surface behavior. PHFs consist of a hydrophobic core and hydrophilic pieces (~20 hydroxyl groups) and these hydroxyl groups are not uniformly distributed around the fullerene structure.[44, 145] This inhomogeounus distribution of -OHs on the fullerene structure can drive aggregation by creating Janus-like hydrophilic and hydrophobic surface regions on the same PHF.[146] The PHFs used in these studies are also charged. The literature contains conflicting accounts about the charged state of PHFs in solution, so conductivity measurements were carried out with PHF Millipore water [44, 146-148]. Control experiments testing the conductivity of ethanol in water and NaCl at equivalent PHF concentrations were also performed (Figure 2.2).

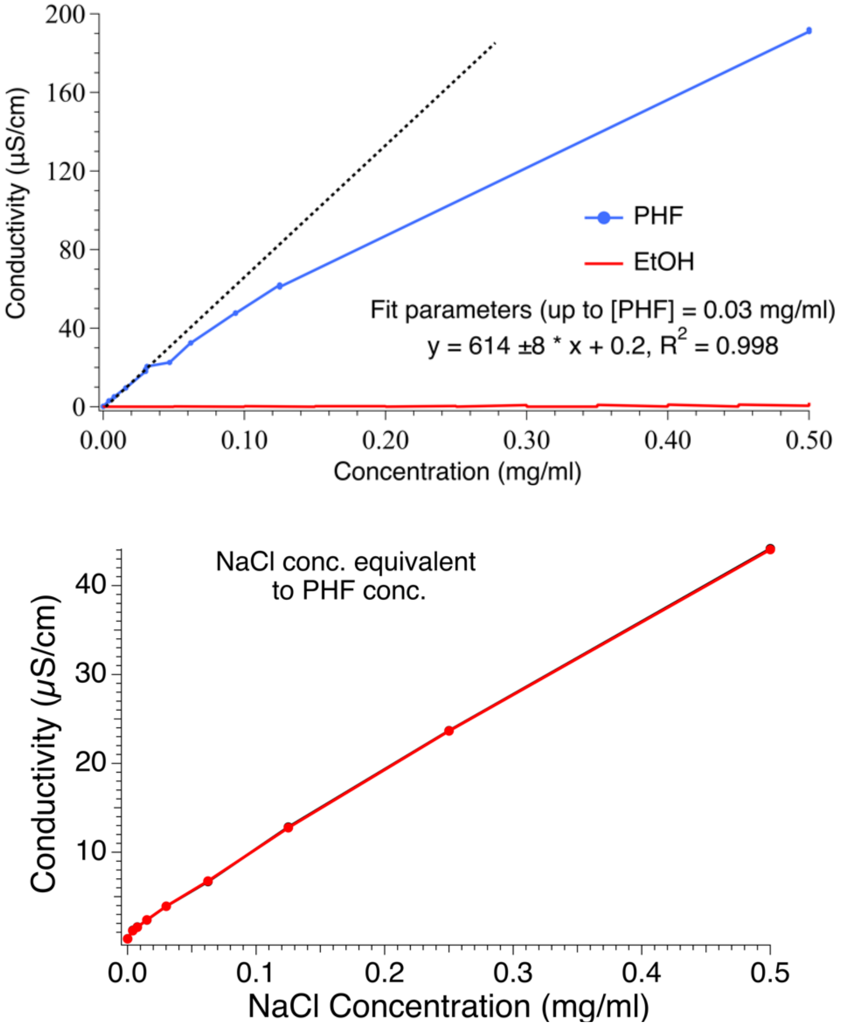

Figure 2.2. Top: Conductivity measurements of PHFs in comparison to ethanol/Millipore water mixtures. The dashed line corresponds to a linear fit of solution conductivity as a function of PHF concentration including concentrations of 0.03 mg/ml. Bottom: Conductivity measurements of NaCl at equivalent PHF concentrations. Uncertainty in measured conductivities is ≤ ±1.0 µS/cm.

Conductivity experiments were performed using Millipore water having a resistivity of 18.2 MΩ-cm (= conductivity of 0.055 µS/cm). When comparing NaCl conductivity to that of PHFs at equivalent concentrations, the data show clearly that the PHFs used here increase the ionic strength of the aqueous solution and do with a slope that strongly suggests that, on average, PHF solutes carry a formal charge of around -4.

At PHF concentrations above 0.03 mg/mL, the data start to depart from linearity reflecting an activity constant of less than unity and suggesting that in Millipore water aggregation may start to affect PHF solvation.

2.3.2 Optical Behavior of PHFs at Air – Water Interface in Bulk Solution

An independent, non-invasive means of testing PHF surface activity is to measure how PHF adsorption changes a surface's optical properties. PHFs have a broad, featureless absorbance across the visible and UV region that rises smoothly at shorter wavelengths (Figure 2.3). For the wavelengths used in SHG experiments, 690 nm incident and 345 nm signal, the molar extinction coefficient increases by 3.6. Resonance enhanced SHG experiments took advantage of these features to independently evaluate PHF surface activity.

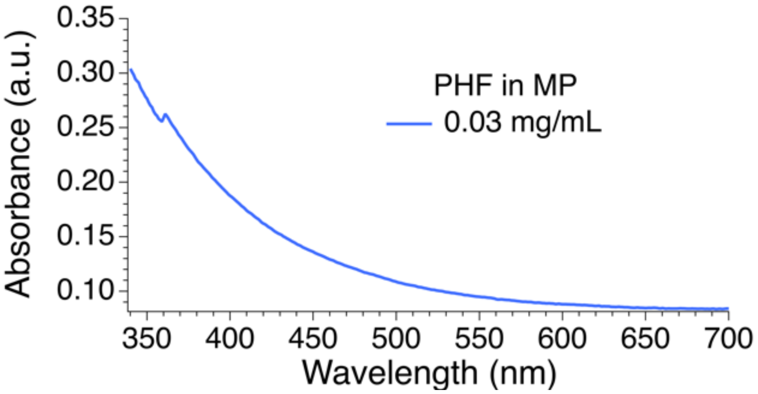

Figure 2.3. Absorbance measurement of 0.03 mg/mL PHF in Millipore water.

Figure 2.4 shows the SHG response measured from the water–air interface as a function of bulk PHF concentration in Millipore water and in solutions containing 50 mM and 500 mM NaCl. Several observations stand out. First, PHF solutions in Millipore and 50 mM NaCl show measurable SHG signal having comparable magnitudes to that observed from the neat water-air interface. The fact that PHFs have a SHG response means that the resonant electronic transition is both 1- and 2- photon allowed.[149] By symmetry, this discovery predicts a non-symmetric distribution of –OH groups on the fullerene structure.[150] Second, SHG signal from PHF samples in 500 mM NaCl solutions are significantly suppressed. These observations are consistent with the surface tension data in Figure 2.1 that show PHF surface activity to be significantly suppressed in solutions having high ionic strength.

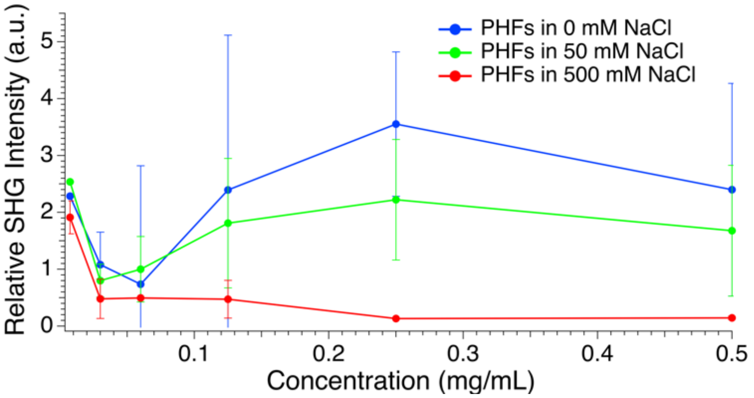

Figure 2.4. Fixed wavelength (690 nm incident and 345 nm for collection) relative SHG signal intensity of PHFs at higher concentrations in 0 mM NaCl, 50 mM NaCl, and 500 mM NaCl.

The third observation is the most curious: SHG signal as a function of concentration does not behave in a manner consistent with simple monomer adsorption to a surface.[59] Relative to the neat air–water interface, SHG intensity first *decreases* at low PHF concentrations before starting to increase (in the case of Millipore and 50 mM NaCl) when PHF concentration exceeds 0.063 mg/ml. According to Equations 2.5 and 2.8, in the absence of surface coverage-dependent reorientational effects, I_{SHG} should scale as N^2 meaning that the signals reported in Figure 2.4 should rise quadratically with increasing PHF concentration. The fact that the SHG first drops and then rises with increasing PHF concentration is consistent surface aggregation and implies that aggregates rather than monomers are responsible PHF surface activity and the enhanced nonlinear optical susceptibility observed at PHF concentrations above 0.06 mg/ml. [61] These findings are also consistent with the very low surface excess concentrations reported in Table 2.1 in the 500 mM NaCl solutions where the high ionic strength is expected to suppress aggregate formation. While these conclusions are admittedly speculative, the data do show that PHF adsorption affects the nonlinear optical properties of the water–air interface and hint that PHF surface chemistry reflects a delicate balance between a solute's aggregation behavior both in bulk solution and in the anisotropic surface environment.

2.4 Conclusions

Surface tension data from PHF dissolved in Millipore, 50 mM NaCl, and 500 mM NaCl solutions show that highly soluble PHFs are also weakly surface active. Increasing solution phase ionic strength suppresses but does not eliminate PHF adsorption to the aqueous-air interface. Conductivity measurements show that PHFs used in these studies are charged with an average charge of -4 per monomer. Independent SHG measurements confirm PHF surface activity, and the data are generally consistent with conclusions based on surface tension data. However, SHG results show unusual behavior in the low PHF concentration limit, implying that PHF speciation at the surface is changing. We propose that in the low concentration limit, the SHG response reflects contributions from monomers while at concentrations ≥0.06 mg/ml, the nonlinear optical response comes from aggregates. Given the prevalence of soluble, inorganic carbon species in environmental systems, we anticipate that findings reported in this work will have important consequences for predicting how carbon-containing particulates affect the surface properties of rivers, streams, and aqueous aerosols.

CHAPTER THREE

CARBON NANOPARTICLE-INDUCED ORGANIZATIONAL CHANGES IN LIPID MONOLAYERS AT WATER – AIR INTERFACES

Contribution of Authors and Co-Authors

Manuscript in Chapter 3:

Author: Nida Shaikh

Contributions: Collected and analyzed all experimental data and authored manuscript

Co-Author: Jessica M. Andriolo

Contributions: Assisted with spectroscopic ellipsometry setup, measurements, analysis, and editing manuscript

Co-Author: Jack L. Skinner

Contributions: Assisted with spectroscopic ellipsometry analysis, and editing manuscript

Co-Author: Robert A. Walker

Contributions: Assisted with data analysis, writing, and editing manuscript

Information

Nida Shaikh, Jessica M. Andriolo, Jack L Skinner, and Robert A. Walker

J. Phys. Chem. B

Status of Manuscript:
____ Prepared for submission to a peer-reviewed journal
_X__ Officially submitted to a peer-reviewed journal
____ Accepted by a peer-reviewed journal
____ Published in a peer-reviewed journal

Publisher: American Chemical Society
Date of Submission: 12-04-2022
Date Accepted: D M Y
Volume __, M Y, ####-####
DOI: ###

CHAPTER THREE

CARBON NANOPARTICLE-INDUCED ORGANIZATIONAL CHANGES IN LIPID MONOLAYERS AT WATER – AIR INTERFACES

3.1 Introduction

Black carbon (BC) is a component of $PM_{2.5}$ (particulate matter <2.5 μm in diameter) produced by both natural and anthropogenic combustion processes. BC aerosol adsorption to biologically relevant water – air interfaces such as alveoli surfaces has long been associated with health risks and is linked to increased mortality rates throughout the world [11-13]. Specific to pulmonary diseases, BC aerosols change the structural, elastic, and dynamic properties of lung surfactant [17, 100]. The mechanisms responsible for these effects, however, remain under debate. Specifically, the impact of carbon particulates on lung surfactant structure and organization, and the consequences of these interactions on lung surfactant's dynamic properties remain correlative at best. Furthermore, the chemistry of these heterogeneous systems becomes even more complex when one considers that BC itself changes as a function of time. While BC typically starts out hydrophobic with high carbon content, oxidative processes render aged BC much more hydrophilic and highly soluble in aqueous solution [35, 36, 133-135].

Studying the effects of BC on lung surfactant typically proceeds in one of two ways. At a physiological scale, *in vitro* and *in vivo* experimental systems demonstrate the effects of carbonaceous pollutants by directly linking inhalation of and exposure to nonbiological particulates in the atmosphere/environment to cardiorespiratory health impacts, including susceptibility to respiratory viruses, particle – induced lung cancer, pulmonary pathophysiologic changes, and cardiac injury [151-154]. A second approach attempts to identify specific particulate surfactant interactions by distilling the system's complexity to its component parts, starting from the level of model systems in order to generalize to larger, ensemble effects [13, 17, 155]. Both approaches are necessary, as the physiological studies are, by definition, considering the consequences of BC on lung surfactant function, and the laboratory, model-system experiments provide the detailed, molecular level insight necessary for developing predictive models. Work described in this manuscript adopts the latter approach: optical and thermodynamic methods are used to evaluate the effects of soluble carbon particulates chosen as models for aged BC on dipalmitoylphosphatidylcholine (DPPC) monolayers adsorbed to the water – air interface as a function of monolayer compression.

The system used in this work was chosen to reproduce many of the features found at the tissue – air interface in lungs. Lung alveoli consist of a water – air interface covered with a surfactant mixture comprised of lipids (90% by mole fraction), cholesterol (10%) and trace amounts of SP proteins [156]. This surfactant mixture reduces water – air interfacial tension and enables alveoli to expand and contract during respiration with significantly reduced mechanical effort [64, 91-93]. Lung surfactant also represents the final line of defense against aerosol inhalation [17] and serves as a barrier that prevents inhaled particulates from entering the bloodstream. DPPC is the majority component of lung surfactant, and DPPC monolayers adsorbed to aqueous – air interfaces are commonly used to model lung surfactant surface properties such as fluidity, permeability, and miscibility (in mixed Langmuir films) [60, 64, 94, 95]. Freshly generated BC aerosols generally start out with high elemental carbon content and are quite hydrophobic, [157] but as they age and become oxidized their elemental carbon content decreases making them hydrophilic and water soluble [133-135]. Polyhydroxylated fullerenes (PHFs), also known as 'fullerols' or 'fullerenols,' comprise a family of soluble carbon particulates (CPs) with solubilities as high as 58.9 g/L in water [35, 36], making them ideal surrogates for aged BC aerosols [130-132].

In the studies described below, surface tension measurements, surface – specific vibrational sum frequency generation (VSFG) spectroscopy and spectroscopic ellipsometry (SE) are used to examine the effects of PHFs on DPPC Langmuir monolayer structure and organization. Measurements are carried out at two DPPC monolayer surface coverages: 55 Å^2/molecule (corresponding to a monolayer in its liquid condensed state) and 40 Å^2/molecule (corresponding to a tightly packed DPPC monolayer). Findings show that even very small amounts of PHF in solution directly impact monolayer organization. This result is significant by itself, because given PHF high bulk solubility, simple equilibrium considerations would predict that PHF concentrations below ≤ 0.125 mg/ml should lead to vanishingly small surface excess concentrations with very little impact on DPPC monolayer structure. The fact that low PHF concentrations *do* affect DPPC monolayer structure strongly suggests cooperative adsorption where the DPPC attracts *and retains* PHFs in the surface/near surface region, enriching the interface's organic content and forcing the DPPC monomers to adopt a more ordered structure.

3.2 Experimental Methods

3.2.1 Materials

1,2-Dimyristoyl-*sn-glycero*-3-phosphocholine (DPPC) was purchased from Avanti Polar Lipids Inc. (powder, >99% purity; Alabaster, AL) and used as received. PHFs were purchased from American Elements (Los Angeles, CA) and used as received. The PHFs themselves consisted of a mixture of species having the general formula $C_{60}(OH)_n \cdot {}_mH_2O$, where $n=22\pm2$ (determined by SEC-HPLC), $m>8$). HPLC-grade chloroform, used as the DPPC spreading solvent, was purchased from Fisher Scientific (99.9% purity; Waltham, MA). The aqueous subphase used was water from a Millipore filtration system (Synergy® by Millipore). Before any addition of lipids or PHFs, the subphase had a resistivity of 18.2 MΩ and a surface tension of 72.5 mN/m at 23 °C.

3.2.2 Sample Preparation

Sample preparation has been described previously [62-64]. Millipore water was used for all aqueous sample preparations. Polyhydroxylated fullerene stock solutions (0.5 mg/mL) were prepared in Millipore water and sonicated for 5 min. The polyhydroxylated fullerene stock solutions were used to prepare aqueous PHF mixtures of 0.0075, 0.03, 0.06, 0.125, and 0.5 mg/mL. DPPC lipid stock solutions (~0.4-0.7 mg/mL) were prepared in chloroform and sonicated for 10 min. Aqueous PHF samples for VSFG measurements were prepared in borosilicate Petri dishes. The Petri dishes were rinsed with methanol, acetone, and Millipore water several times prior to acid-washing (50/50 vol. nitric/sulfuric), and then rinsed with Millipore water several times before use. Surface tension measurements of these systems show PHFs to be very weakly surface active with surface concentrations of $7.5*10^{13}/cm^2$ at the highest bulk concentrations used in these studies (see Figure 3.1 and Table SI-3.1). A Hamilton glass microsyringe was used to apply the appropriate amount of the DPPC/chloroform stock solution to the subphase surface to ensure the desired surface coverage of 55 or 40 $Å^2$/molecule. After depositing the DPPC at the water – air interface, the sample was allowed to sit for ≥ 5 minutes so that the chloroform could evaporate and the DPPC monolayer could equilibrate – DPPC was deposited on both a neat Millipore subphase, as well as on aqueous PHF subphases.

3.2.3 Surface Tension and Langmuir Trough

Simple surface tension measurements and Langmuir trough compression isotherms were carried out using methods described previously [62-64]. Simple surface tension measurements were carried out to quantify PHF surface activity. These experiments simply consisted of preparing Millipore solutions having different PHF concentrations, measuring the surface tension with a calibrated, NIMA PS-4 pressure sensor (with a paper Wilhelmy plate) and converting the surface tension to surface pressure. (Equation 3.1):

$$\Pi = \gamma_0 - \gamma \text{ (Eqn. 3.1)}$$

In experiments designed to determine whether or not the soluble PHFs are surface active, surface pressure is plotted as a function of the natural log of concentration and surface excess concentrations are determined using the Gibbs isotherm equation (Equation 3.2) [140]:

$$\Pi A = nk_B T \ln(c) \quad \text{(Eqn. 3.2)}$$

$$\Gamma = \frac{n}{A} = \frac{1}{k_B T}\frac{d\Pi}{d\ln c} \quad \text{(Eqn. 3.3)}$$

where Γ is the surface excess concentration, A is the sample area, n is the number of adsorbed species, k_B is Boltzmann's constant, T is temperature (in K) and c is the PHF concentration. Note that for the experiments described here, a 1 mg/ml PHF solution was chosen as a reference concentration. (This concentration corresponds to approximately 0.8 mM.) Terminal surface coverage is determined from the slope of steepest ascent (Equation 3.3).

To assess the effects of soluble PHFs on insoluble DPPC monolayers, compression isotherms were acquired using a NIMA Langmuir trough (Model 302LL) equipped with a NIMA PS4 pressure sensor and a microprocessor interface 104. To obtain Langmuir trough compression isotherms, Langmuir trough barriers were closed at a speed of 12 cm^2/min, although slowing this compression by a factor of 3 did not change observed results. Surface pressure (Π) was measured as a function of surface area.

Given that the PHFs were found to be only weakly surface active, we can calculate excess free energies of mixing, ΔG^E_{mix} for Equation 3.4. In Equation 3.4, A_{12} is the actual area per molecule of a mixed monolayer, A_1 and A_2 are the area per molecule of a pure monolayer of one of the species in the mixed monolayer, and x_1 and x_2 are the mole fractions of each of the species in the mixed monolayer [62, 158, 159].

$$\Delta G^E_{mix} = \int_{\pi_1}^{\pi_2} N_A(A_{12} - x_1 A_1 - x_2 A_2)\,d\pi \quad \text{(Eqn 3.4)}$$

Equation 3.4 can be further simplified. Because PHFs are highly soluble in aqueous solution (>50 mg/mL in H_2O), we assume that DPPC (species 1) is the only species constrained to the water – air interface. Using this assumption, Equation 3.4 simplifies to Equation 3.5.

$$\Delta G_{mix}^{E} = \int_{\pi_1}^{\pi_2} N_A (A_{12} - A_1) d\pi \text{ (Eqn. 3.5)}$$

Therefore, by integrating the differences in area between the isotherm from the system of interest and that of pure DPPC as a function of surface pressure, the excess free energy of mixing can be determined. We note here that if the PHFs showed no affinity for the DPPC monolayer, this integral would equal zero.

3.2.4 Vibrational Sum Frequency Generation Spectroscopy

Vibrational sum frequency generation (VSFG) is a second-order nonlinear spectroscopy technique that has been described in detail previously [53, 62-64, 160]. Interfaces break the inversion symmetry between centrosymmetric media, leading to VSFG becoming symmetry allowed provided that species at the interface have a net polar ordering [115]. To perform VSFG experiments, two oscillating electromagnetic fields at different frequencies (fixed visible 800 nm and a tunable IR) are overlapped both spatially and temporally on a surface of interest. The two fields couple through the 2nd order susceptibility tensor, $\chi^{(2)}$, and create a coherent nonlinear polarization equal in frequency to the sum of the two input frequencies.

In SFG experiments, the intensity of the resultant SF signal, $I(\omega)$, is proportional to the square of the effective portion of the 2nd order nonlinear susceptibility, $\chi_{eff}^{(2)}$, as shown in Equation 3.6. The $\chi^{(2)}_{eff}$ consists of two parts, a resonant contribution ($\chi^{(2)}_{q,eff}$) and a non-resonant contribution ($\chi^{(2)}_{NR,eff}$). When the IR frequency (ω_{IR}) is resonant with a vibrational mode (ω_q) of surface species, the SF signal generated is resonantly enhanced, as displayed in Equation 3.7 [160].

$$I(\omega) \propto \left|\chi^{(2)}_{eff}\right|^2 \text{ (Eqn. 3.6)}$$

$$\left|\chi^{(2)}_{eff}\right|^2 = \left|\chi^{(2)}_{NR,eff} + \sum \frac{\chi^{(2)}_{q,eff}}{\omega_{IR} - \omega_q + i\Gamma_q}\right| \text{ (Eqn. 3.7)}$$

Reported VSFG spectra were acquired under SSP polarization conditions (listed in order of sum, visible, and IR polarizations, respectively - $S_{sum}S_{vis}P_{IR}$). The SSP polarization combination samples a single $\chi^{(2)}$ element, $\chi^{(2)}_{iiz}$ and is sensitive to only those vibrations whose IR transition moment is aligned along the surface normal (assigned as the z-axis). r+/d+ ratios reported from VSFG spectra are the average of 2-5 measurements taken per sample.

The VSFG setup used has been described in detail elsewhere [62-64]. Briefly, ~3.4 W from a Ti-Sapphire regenerative amplifier (Libra-HE, Coherent, 85 fs pulses, 1 kHz repetition rate, 800 nm) was coupled to an optical parametric amplifier (Coherent OPerA Solo). An 80/20 beam splitter reflects 80% of the 800 nm into a tunable Coherent OPerA Solo optical parametric amplifier to produce IR light. The 800 nm light and the IR light (centered at ~3.4 μm) are then aligned both spatially and temporally, and focused onto the sample of interest at 48 and 38°, respectively, from surface normal. The SF response is then collimated and isolated before being focused into a monochromator (SpectraPro-

300i, Action Research Corporation). The SF response is then dispersed into a 1340 x 100 pixel CCD (PIXIS100B, Princeton Instruments).

4.2.5 Spectroscopic Ellipsometry

Spectroscopic ellipsometry experiments were carried out with a J.A. Woollam RC-2 and data were analyzed in CompleteEASE, a modeling software application distributed by J.A. Woollam. The beam from the instrument was calibrated in the source and detector prior to every measurement. The signal detected was the change in polarization upon the incident beam irradiating the sample, which was quantified through ellipsometric angles Ψ (amplitude ratio) and Δ (phase difference) in Equations 3.8 and 3.9 respectively.

$$\tan(\Psi) = \frac{|R_p|}{|R_s|} \text{ (Eqn. 3.8)}$$

$$\Delta = \Delta_p - \Delta_s \text{ (Eqn. 3.9)}$$

$$\rho = \frac{R_p}{R_s} = \tan(\Psi)\, e^{i\Delta} \text{ (Eqn. 3.10)}$$

A sample of pure Millipore water matched with a mean standard error (MSE) of 0.99-2.28 at the start of the measurements to a model of water at 25 °C. The incident angle was set at 75° with the thickness set to fit. Once Ψ and Δ were obtained, the complex reflectance ratio (ρ) was determined by using Equation 3.10, and then used to derive the optical constants (i.e. film thickness) of lipid films at the air – water interface [119-122]. Monolayer thicknesses reported from SE experiments are the average of 6 measurements taken per sample.

3.3 Results

3.3.1 Surface Tension and Langmuir Trough

To address whether soluble PHFs affect insoluble DPPC monolayer structure and organization, experiments were first carried out to assess whether the PHFs themselves were surface active. Surface tension measurements of PHF-containing aqueous solutions were made as a function of PHF concentration, and results were plotted as surface pressure (Π) vs. the natural log of PHF concentration. (Figure 3.1, top) the rise in surface pressure as a function of PHF concentration shows that these soluble solutes are, in fact, surface active. The isotherm itself shows unusual behavior. After passing through an inflection point at a concentration of approximately 0.37 mg/ml (ln[C] = -1.0) and starting to plateau, the surface pressure starts to rise steeply again at PHF concentration above ~7.4 mg/ml (ln[C] > 2.0). Vibrational and ellipsometry experiments show that PHF effects on lipid monolayer organization are most pronounced in the low PHF concentration limit, so all further results described below are carried out with solutions having PHF concentrations ≤ 0.125 mg/ml (= <-2.8 on Figure 3.1, top). PHF surface behavior at higher concentrations will be the subject of future studies.

Analyzing the data in Figure 3.1 (top) using the Gibbs isotherm (Equations 3.2 and 3.3) leads to a terminal monolayer coverage of 7.5 x 10^{13} cm^{-2} or, equivalently, ~130 Å^2/molecule. Given an estimated PHF radius of ~4.5Å, each PHF has a 64 Å^2 footprint, meaning that PHFs adsorbed to the aqueous/air interface are not tightly packed. As the VSFG and SE experiments described below will show, most of the changes induced by PHFs on DPPC monolayer organization occur at PHF concentrations below 0.06 mg/ml where PHF surface coverage (at the neat water – air interface) is even smaller (2.6 x 10^{13} cm^{-2} or 380 Å^2/molecule).

DPPC compression isotherms were acquired on a Langmuir trough having different amounts of PHF present in the subphase (Figure 3.1, middle). The pure DPPC isotherm lifts off between 100-110 Å^2/molecule and passes through a liquid expanded-liquid condensed coexistence region between 90 Å^2/molecule and 60 Å^2/molecule. The monolayer collapses with a terminal surface coverage of 42 Å^2/molecule, in agreement with previous literature reports [62-64]. The isotherms show slight but measurable deviation with PHF sub-phase concentration. Specifically, increasing PHF concentration leads to slightly expanded monolayers where a given surface pressure corresponds to increasingly larger areas. In this context, areas are reported as areas per DPPC monomer given that PHFs are only weakly surface active with a coverage corresponding to >200 Å^2/molecule at the neat aqueous/air interface for a concentration of 0.125 mg/ml. As will be discussed below, we believe that the DPPC monolayer actually *enriches* PHFs at the interface in ways that enhance lipid structure and organization.

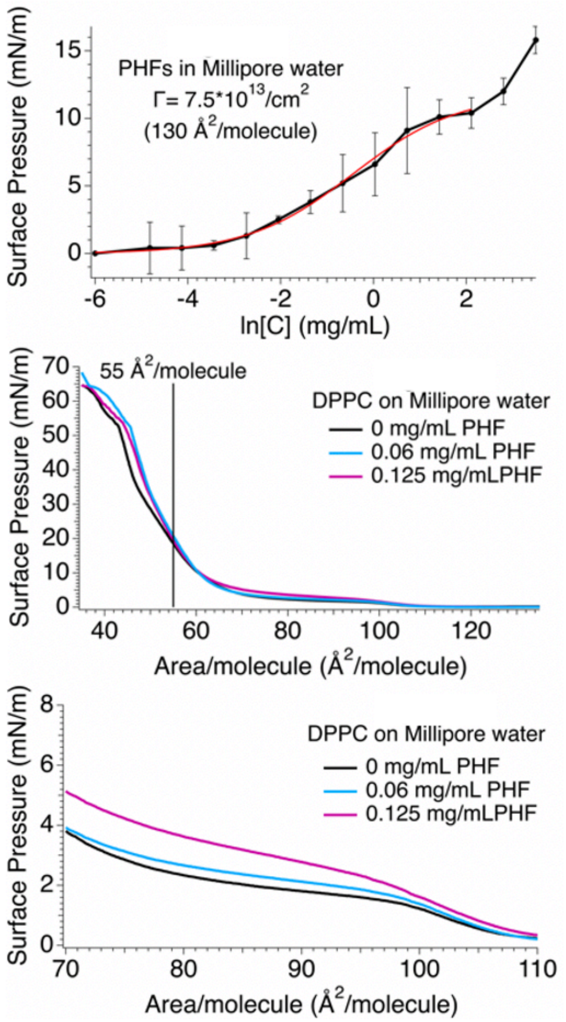

Figure 3.1. Surface tension measurements (ln[C] vs. surface pressure) demonstrating surface activity, where C is PHF concentration. The red line is an empirical fit of the data to a sigmoidal function and is used to calculate slope at different bulk solution PHF concentrations (top). Langmuir trough compression isotherms of DPPC with PHF subphase of varying concentrations (middle). An expanded view of Langmuir trough compression isotherm data showing slight, systematic variation in liftoff and slope with changing PHF concentrations (bottom).

3.3.2 Excess Free Energy of Mixing

Because adsorbed DPPC is constrained to the surface, integrating the differences in area between the isotherm from the system of interest and that of pure DPPC as a function of surface pressure provides information about mixing behavior at the interface.

A positive ΔG^{EX} value reflects a more expanded mixed monolayer relative to the weighted sums of the pure components. Similarly, a negative ΔG^{EX} value implies that the mixed monolayer is more compressed with attractive interactions between the constituent components. Such an interpretation is misleading for the DPPC/PHF system.

The isotherms in Figure 3.1 (middle) show that at a given surface pressure, the small amount of PHF in solution leads to a larger DPPC mean molecular area (MMA), but if PHFs are being drawn to the surface through cooperative interactions, then their adsorption from the bulk to the water – air interface will force the DPPC monomers to become *more* tightly packed. Similar results have been reported before with soluble alkyl surfactants and with simple monosaccharides [62, 63, 161]. VSFG data below suggest that such a picture accurately describes the effects of PHFs on DPPC monolayers in the liquid condensed state (55 Å^2/molecule). Langmuir trough compression isotherm data from Figure 3.1 (middle) were analyzed using excess free energy expressions shown in Equations 3.4 and 3.5. ΔG^{EX} values in Figure 3.2 show positive excess free energies, consistent with PHF cooperative adsorption, and although the excess free energies are small, they have measurable effects on monolayer structure. (*Vide infra.*)

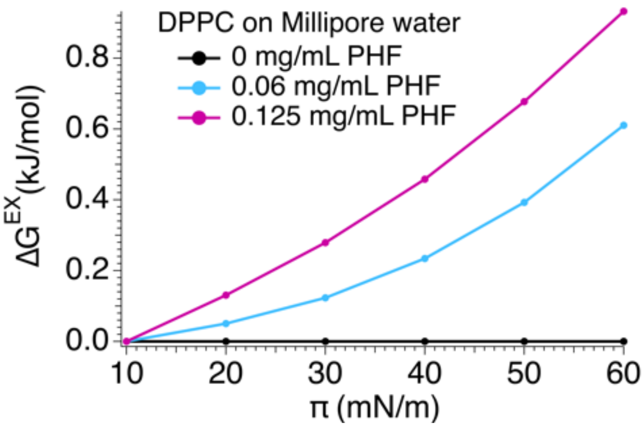

Figure 3.2. Excess free energy of mixing for DPPC with PHF solution mixtures at very low PHF concentrations.

While thermodynamic data are instructive, they do not provide information about molecular structure and organization. Discerning molecular structure and organization at interfaces is challenging due to the small number of molecules involved and the sometimes large, overwhelming responses from bulk solution responses. In order to determine how inclusion of surface active, soluble carbonaceous particulates changes lipid film structure and organization, VSFG was used to measure vibrational spectra of DPPC monolayers in their liquid condensed and tightly packed states.

3.3.3 VSFG (Spectra & r^+/d^+ Ratios)

Figure 3.3 shows VSFG spectra in the CH stretching region of DPPC monolayers in their liquid condensed and tightly packed states. Following convention, “r” denotes vibrations associated with the DPPC methyl group and “d” describes vibrations associated with methylene groups [162, 163]. The “+” indicates a symmetric stretch (SS) and a “-“ indicates an antisymmetric stretch (AS). d^+ at 2850 cm^{-1} corresponds to a CH_2 SS, r^+ at 2874 cm^{-1} corresponds to a CH_3 SS, r^- at 2952 cm^{-1} corresponds to an out-of-plane CH_3

AS, r^- at 2962 cm^{-1} corresponds to an in-plane CH_3 AS, and r^+_{FR} at 2930 cm^{-1} corresponds to a CH_3 Fermi resonance interaction [64, 117]. Note that the y-axes report intensities in 'arbitrary units' (au), and intensities should not be compared directly between Figures 3.3 (left) and 3.3 (right). A better indicator of the absolute signal intensities in the two spectra can be inferred from each spectrum's S/N. As expected based on number density and polar ordering considerations, spectra from the more expanded, liquid-condensed monolayer are much weaker than those from tightly packed monolayers.

A ratio of the r^+ and d^+ intensities often serves as a sensitive indicator of alkyl chain conformational order [164-166]. Under $S_{sum}S_{vis}P_{IR}$ conditions, a well-ordered monolayer with alkyl chains in an all-*trans* conformation aligned predominantly along the surface normal will show a strong r^+ band and a weak d^+ band. The strong r^+ results from the terminal methyl groups aligned with their local C_3 axes (and IR transition moments) directed in the laboratory z-axis. Two considerations lead to a weak d^+ band in this well-ordered system: first, if the chains are all-*trans* and aligned along the surface normal, the CH_2 symmetric (and antisymmetric) IR transition moments will be aligned in-plane and will not be accessible to the SSP polarization combination. Second, an all-*trans* chain will have local inversion symmetry about each carbon-carbon bond making the d^+ transition symmetry forbidden in VSFG experiments. The introduction of *gauche* defects leads to more conformational disorder, a weaker r^+, and the appearance of now-symmetry allowed d^+ transitions. Evidence of this behavior is readily apparent in Figures 3.3 (left) and 3.3 (right), where the more loosely packed DPPC monolayer (55 $Å^2$/molecule, Figure 3.3, left) has an r^+/d^+ ratio of 0.6 and the tightly packed, well-ordered DPPC monolayer (40 Å^2/molecule, Figure 3.3, right) has an r^+/d^+ ratio of 5.0 This ratio will serve as an important indicator of how DPPC monolayers are affected by soluble PHFs. We note that the PHFs themselves have no VSFG active features in the region of interest. We also acknowledge that the r^+/d^+ ratio in the liquid condensed phase is very sensitive to small changes in surface coverage so that this value can range from 0.4 to 1.4.

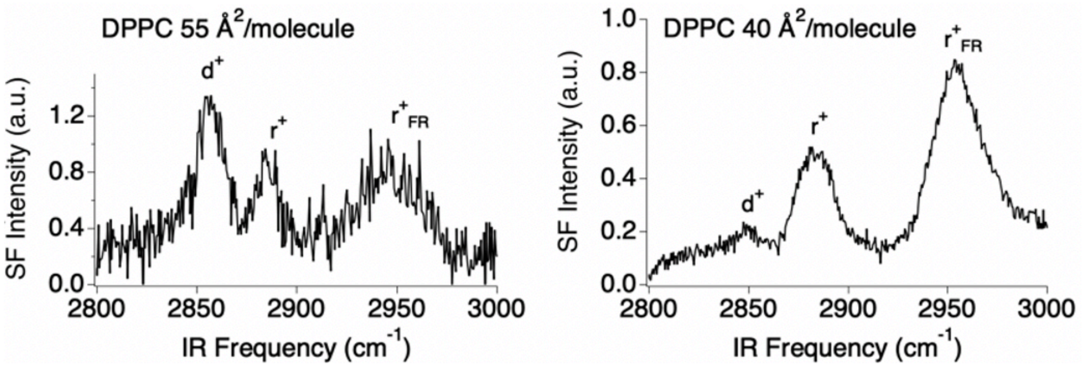

Figure 3.3. VSFG spectra of 55 Å^2/molecule DPPC on Millipore water at SSP polarization with peak assignments, and an r+/d+ ratio of 0.60 (left). VSFG spectra of 40 Å^2/molecule DPPC on Millipore water at SSP polarization with peak assignments, and an r+/d+ ratio of 5.0 (right).

Figure 3.4 shows resonant VSFG spectra from DPPC monolayers at 55 Å^2/molecule and 40 Å^2/molecule as a function of solution phase PHF concentration. Of importance is the scale of SF intensity. Although the data are baseline corrected relative to a pure water – air interface, addition of PHF to the aqueous solution leads to a baseline that rises with increasing PHF concentration. Analysis of reflectivity data (Figure SI-3.2) show that the surface reflectivity remains constant for all PHF concentrations tested in this work, so the rising baseline is not attributed to a change in reflectivity. We speculate that the rising baseline may result from broadband fluorescence emission following 2-

photon absorption, but this hypothesis has yet to be tested and will be the subject of future studies. The symmetric VSFG lineshapes show that the increasing baseline signal is not coherent and thus does not interfere with the nonlinear VSFG response.

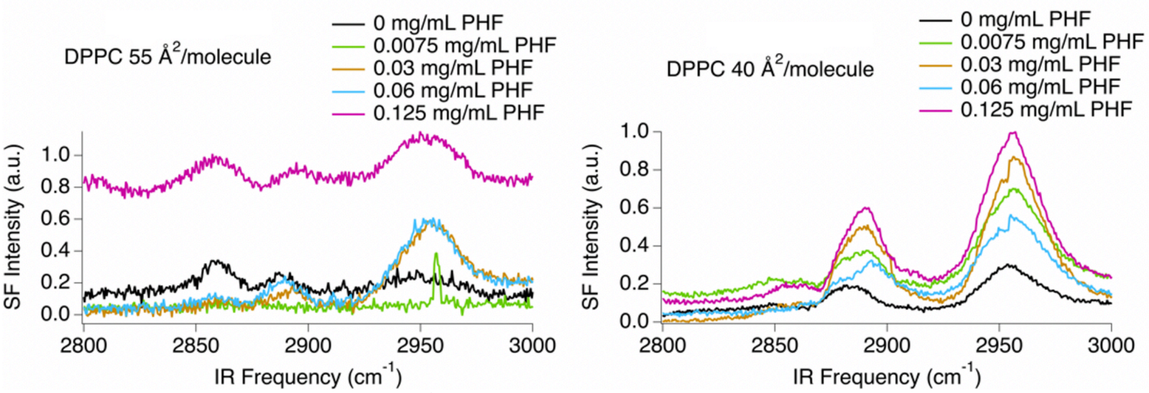

Figure 3.4. VSFG spectra of 55 Å^2/molecule DPPC on different concentrations of PHFs with a neat Millipore subphase (all at SSP polarization), with an r+/d+ ratio of 0.60 (left). VSFG spectra of 40 Å^2/molecule DPPC on different concentrations of PHFs with a neat Millipore subphase (all at SSP polarization), with an r+/d+ ratio of 5.0 (right).

Changes in the VSFG spectra as a function of PHF concentration show that these soluble carbon particulates affect DPPC monolayer structure. These changes are most evident when comparing the r^+/d^+ intensity ratios from the different spectra. Figures 5 shows r^+/d^+ ratios for DPPC monolayers as a function of PHF concentration. These ratios were calculated from spectra acquired with an $S_{sum}S_{vis}P_{IR}$ polarization combination meaning that larger r^+/d^+ ratios reflect DPPC chains having more upright, all-*trans* conformations. Figure 3.5 shows that, in neat Millipore, PHFs at very low concentrations increase DPPC acyl chain ordering in a liquid condensed film more so than in a tightly packed film.

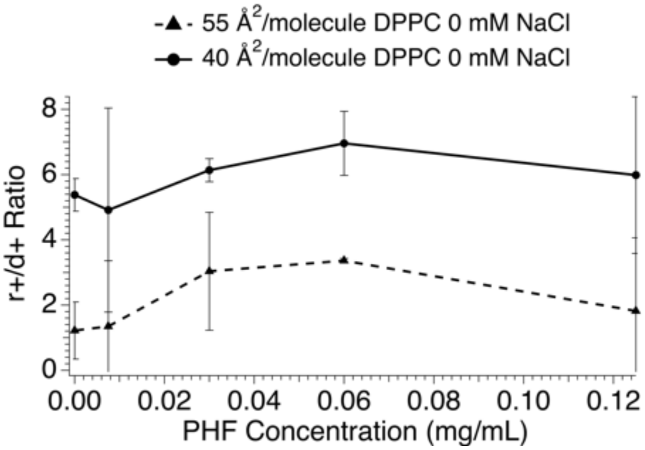

Figure 3.5. VSFG r+/d+ intensity ratios for DPPC on different concentrations of PHFs in neat Millipore at 55 and 40 Å^2/molecule.

This r+/d+ ratio behavior is consistent with results from Langmuir trough compression isotherms shown in Figure 3.1 assuming a cooperative adsorption mechanism that draws PHFs from solution to the DPPC covered water – air interface. In this scenario, PHFs are drawn to the surface by the DPPC monolayer and occupy the interstitial space between the DPPC monomers/islands in their liquid condensed state. When adsorbing to the surface, PHF solutes force the DPPC monomers into a smaller area leading to greater conformational order (and higher surface pressures at a given MMA). For the tightly packed monolayer, the effects of PHF adsorption are less pronounced.

3.3.4 Spectroscopic Ellipsometry

SE experiments were carried out to assess changes in the surface's optical properties and monolayer film thickness. Figure 3.6 shows calculated thickness of both the 55 Å^2 and 40 Å^2 DPPC monolayers as a function of PHF bulk solution concentration.

The procedure for calculating film thicknesses is described in the Experimental Section and has been detailed in other reports [167-169].

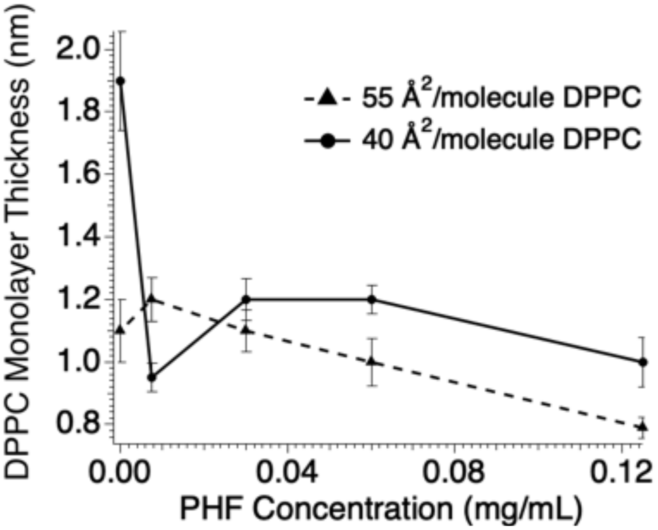

Figure 3.6. DPPC monolayer thickness on different concentrations of PHFs in neat Millipore at 55 and 40 Å^2/molecule. Monolayer thickness uncertainties range between ±0.034 and ±0.16 nm.

SE data show that small amounts of PHF in the subphase lead to systematic changes in DPPC monolayer thickness. We note that SE measurements of aqueous solutions containing only PHFs (e.g. samples whose surface tensions are reported in Figure 1) do not show conclusive evidence of changing surface composition/thickness, so the data reported in Figure 3.6 assume a model equivalent to that used to fit the DPPC-only monolayers on Millipore water. The most extreme effects are observed for the 40 Å^2/molecule monolayer. In the absence of any PHF in solution, the tightly packed monolayer is 1.9 nm thick, a value consistent with previous reports [167-169]. Even the smallest amount (0.0075 mg/ml) of PHF in solution, however, leads to a 2-fold drop in monolayer thickness (0.95 ± 0.05 nm). Changes in DPPC monolayer thickness are less pronounced at higher PHF concentrations, falling between 1.2 and 1.0 nm at concentrations up to 0.12 mg/ml. For the 55 Å^2/molecule films, monolayer thickness is 1.1 nm in the absence of PHF, consistent with an 'thinner', more disorganized monolayer and the correspondingly smaller r^+/d^+ ratio observed in the VSFG data. Monolayer thickness rises slightly at the lowest PHF concentration (to 1.2 nm) before falling monotonically to 0.8 at a PHF concentration of 0.12 mg/ml.

3.4 Discussion

The studies described above were premised on the notion that interactions between soluble carbon nanoparticles and lipid monolayers change monolayer properties. Unknown when the work began was the concentration range where these interactions would be most pronounced. In this section, findings from each type of measurement – surface tension, VSFG, and SE – are summarized and interpreted in the context of the original hypothesis.

Surface tension measurements resulted in two important discoveries. First, PHFs themselves are weakly surface active, creating terminal monolayer coverages of 7.5×10^{13} molecules/cm^2 at the water – air interface when bulk PHF concentrations approach 0.5 mg/ml. Fitting the data in Figure 3.1 results in a ΔG_{ads} for PHFs to the neat water–air interface of -30 (±5) kJ/mole, a value of similar magnitude as for other nonionic surfactants such as Triton X-100 [102]. Second, even though PHFs are not strongly drawn to the water – air interface, their presence in solution has readily observable effects on DPPC monolayer compression isotherms that suggest a cooperative adsorption mechanism. Specifically, even at the lowest PHF bulk concentration tested in this work (0.0075 mg/ml) where surface coverages at the neat water – air interface are only 3 x 10^{12} molecules/cm^2 or ~4% of full monolayer coverage, PHFs cause DPPC isotherm to shift to larger areas with consistently larger DPPC MMAs relative to DPPC on a pure water subphase. While this effect is often interpreted in terms of more expanded monolayers, an alternative explanation – especially in the context of one monolayer component being highly soluble in the subphase – is that cooperative interactions between the PHF and DPPC *draw* the PHF from solution, *enriching* interfacial organic composition and forcing the DPPC monomers into more tightly packed, better organized structures. Data from VSFG and spectroscopic ellipsometry measurements support this interpretation for the liquid condensed monolayer. For the tightly packed monolayer, interpretation of the optical data is more nuanced.

In order to test the effects of PHF concentration on DPPC monolayer structure and organization, VSFG measurements were performed at two different DPPC surface coverages: 55 Å^2/molecule (where the DPPC monolayer is in its liquid condensed state) and 40 Å^2/molecule (corresponding to a tightly packed DPPC monolayer). As a measure of organization within the DPPC monolayer, a ratio of r^+/d^+ intensities was used, where a larger ratio corresponds to acyl chains tightly packed vertically aligned having very few *gauche* defects. Not surprisingly, the tightly packed monolayer on a pure aqueous subphase is much more ordered than the liquid condensed monolayers with the two systems having average r^+/d^+ ratios of ~5.5 and ~1.0, respectively.

With increasing PHF concentration, this ratio for the liquid condensed monolayer rises by a factor of 3 (to 3.0). Together with the surface tension data, these observations strongly suggest that PHFs are adsorbing to the surface, effectively compressing the liquid condensed DPPC monolayer, leading to higher surface pressures at a given DPPC MMA and more highly ordered DPPC monomers as described above.

PHF-induced changes in tightly packed DPPC monolayer organization are more challenging to interpret. The well-ordered monolayer inferred from a large r^+/d^+ ratio diminishes slightly with the addition of the smallest amount of PHF in solution that was tested (0.0075 mg/ml). This change in r^+/d^+ character coincides with a significant drop in monolayer thickness as measured by spectroscopic ellipsometry. Given that these experiments are performed independently and the results reproduce with equivalent samples, we believe these effects are real and coupled. Higher PHF concentrations – although still well below PHF concentrations that result in terminal monolayer coverage – lead at first to modest increases in r^+/d^+ and monolayer thickness (at 0.06 mg/ml) before both measures of DPPC film structure fall at a PHF concentration of 0.125 mg/ml.

Reconciling a modest r^+/d^+ reduction and a 50% loss in film thickness at the lowest PHF concentration is challenging. The DPPC monolayer starts out tightly packed, so unlike with the liquid condensed system, no interstitial space at the water – air interface exists to accommodate adsorbing PHF monomers. If, however, PHF adsorption leads to an overall tilting of the monolayer structure, then the DPPC acyl chains could still retain their high degree of conformational order (with a small d^+ and a smaller r^+ as the IR transition moment is deflected away from surface normal), while the apparent monolayer width shrinks. The tilt would have to be extreme with a 50% loss of monolayer thickness corresponding to a 60° deflection from surface normal. Then, as more PHFs adsorb (from solutions having concentrations of 0.03 and 0.06 mg/ml), the effects induced by the first adsorbed PHFs are diminished and the chains adopt a more upright structure (and the monolayer appears slightly thicker).

This interpretation is admittedly speculative, but it *is* consistent with the observations made from tightly packed DPPC monolayer on a PHF-containing subphase. While the specific mechanisms responsible for these findings remain uncertain, what is clear is that the highly soluble PHF solutes *do* cooperatively adsorb to tightly packed DPPC monolayers and that the effects of cooperative adsorption are significant even at the lowest PHF concentrations sampled in this work.

3.5 Conclusions

Results reported here use optical and thermodynamic techniques to examine the effects of PHFs, a model for aged BC, on DPPC monolayer properties. The first studies focus on model systems having well-controlled lipid compositions as a function of PHF concentrations to determine the mechanism(s) responsible for carbon particulate accumulation at the water – air interface. Surface tension, VSFG and SE experiments all show that soluble PHFs are drawn to the lipid covered water – air interface through a cooperative adsorption mechanism, *and* that this effect is observable even at very low PHF concentrations. For lipid monolayers in their liquid condensed state where area still exists between monomers, PHF adsorption (from bulk solution) effectively compresses the DPPC monolayer making the acyl chains more ordered. For tightly packed DPPC monolayers, surface tension data, VSFG spectra and spectroscopic ellipsometry measurements all show evidence of cooperative adsorption although the data are more difficult to interpret. One possible interpretation is that the small amounts of PHF cooperatively adsorbed to the tightly packed DPPC monolayer induces a net ‘tilting’ of the monolayer away from surface normal leading to a monolayer that appears less well ordered (according to the r^+/d^+ order parameter) and thinner. From a physiological perspective, results presented in this work suggest that carbon particulates, especially those that are at the very small end of $PM_{2.5}$ range as approximated by the PHFs used here, may be enriched at the alveoli water – air interface rather than dissolving into the alveoli’s water subphase.

CHAPTER FOUR

CARBON NANOPARTICLE-INDUCED CHANGES TO LIPID MONOLAYER STRUCTURE AT AIR-WATER INTERFACES.

2. IONIC STRENGTH EFFECTS

Contribution of Authors and Co-Authors

Manuscript in Chapter 4:

Author: Nida Shaikh

Contributions: Collected and analyzed all experimental data and authored manuscript

Co-Author: Jessica M. Andriolo

Contributions: Assisted with spectroscopic ellipsometry setup, measurements, analysis, and editing manuscript

Co-Author: Jack L. Skinner

Contributions: Assisted with spectroscopic ellipsometry analysis, and editing manuscript

Co-Author: Robert A. Walker

Contributions: Assisted with data analysis, writing, and editing manuscript

Manuscript Information

Nida Shaikh, Jessica M. Andriolo, Jack L Skinner, and Robert A. Walker

J. Phys. Chem. C

Status of Manuscript:
_X__ Prepared for submission to a peer-reviewed journal
____ Officially submitted to a peer-reviewed journal
____ Accepted by a peer-reviewed journal
____ Published in a peer-reviewed journal

Publisher: American Chemical Society
Date of Submission: D M Y
Date Accepted: D M Y
Volume __, M Y, ####-####
DOI: ###

CHAPTER FOUR

CARBON NANOPARTICLE-INDUCED CHANGES TO LIPID MONOLAYER STRUCTURE AT AIR – WATER INTERFACES.

2. IONIC STRENGTH EFFECTS

4.1 Introduction

Black carbon (BC) aerosols arising from incomplete combustion and anthropogenic activities have long been identified as a cause of diminished respiratory and pulmonary function, leading to increased mortality rates throughout the world [11-13]. However, efforts to identify carbon particulate-lung surfactant interactions, specifically the impact of carbon particulates on lung surfactant structure and organization, remain incomplete and sometimes contradictory [13, 17, 155]. Work described in this manuscript uses model-system experiments to provide detailed molecular-level insight into the molecular mechanism(s) responsible for carbon particulate-lipid monolayer interactions. Such foundational knowledge is necessary for developing predictive models and considering the actual consequences of BC on lung surfactant function. Model systems used in this work have also been employed to assess how aerosolized environmental contaminants interact with lipid films and to predict the physiological consequences of airborne pollution [170-173].

A DPPC isotherm on pure water has four distinct phases – gaseous phase (G), liquid-expanded (LE) phase, a liquid-expanded – liquid-condensed (LE-LC) coexistence phase, and a liquid-condensed (LC) phase [66, 174-176]. The pure DPPC isotherm lifts off between 100-110 Å^2/molecule. At large areas per molecule, the lipid molecules are dispersed as a 2-dimensional gaseous (G) phase – the hydrophobic tails of the lipid are randomly oriented and in contact with the water surface but have little contact with each other. As the lipid monolayer is compressed into a liquid-expanded (LE) phase, the hydrophobic tails of the lipids come into contact with each other and lift from the water surface but remain largely disordered and fluid. Further compression of the monolayer leads to a first-order transition into a liquid-condensed (LC) phase. In single component lipid monolayers (i.e. DPPC), the LE-LC coexistence phase is delineated by a plateau in the isotherm that extends from 90 to 60 Å^2/molecule[108-110]. The monolayer collapses with a terminal surface coverage of 42 Å^2/molecule, in agreement with previous literature reports [62-64].

DPPC phases, including the LE-LC coexistence region, are also on subphases containing dissolved sodium chloride[174, 176]. The effects of salt on Langmuir monolayers, specifically the impacts of salt on phosphocholine (PC) monolayer structure by means of Langmuir compression isotherms, have been investigated in detail [174, 176, 177]. Coordination of ions to surface-active species such as DPPC is known to alter DPPC orientation, packing, interfacial properties, and surface morphology by significantly perturbing the sustained LC-LE coexistence regions of DPPC monolayers, leading to more rigid films around the LC-LE equilibrium [174, 176-181]. Two mechanisms have been proposed as to how ions affect the aggregation and self-assembly behavior of lipids in aqueous solution – 1) an indirect mechanism of action where the ions interact with the water around the lipid, and 2) a direct mechanism of action where ions interact directly with the lipids [174]. Monovalent cations such as Na^+ cause DPPC monolayers to expand relative to salt-free conditions, with higher salt concentrations leading to more disrupted morphology in the lipid film [176]. Monovalent cations have also been found to increase DPPC alkyl chain ordering while having little interaction with the DPPC headgroup organization [176]. Additionally, the presence of salt in the subphase has been found to increase DPPC monolayer surface pressure at a fixed area per molecule, while simultaneously causing the $\Pi - A$ isotherms to shift to larger areas per molecule which the highest salt concentration exhibiting the largest shift [174, 176, 179, 182-187].

In the studies described below, surface tension measurements, surface specific vibrational sum frequency generation (VSFG) spectroscopy, and spectroscopic ellipsometry (SE) are used to examine the effects of PHFs on DPPC Langmuir monolayer structure and organization as a function of solution-phase ionic strength. Measurements are carried out with DPPC monolayer surface coverages of 40 $Å^2$/molecule, corresponding to tightly packed DPPC monomers, and 55 $Å^2$/molecule, corresponding to a more expanded monolayer in its liquid condensed state. Prior results showed that PHF concentrations as low as 0.03 mg/ml strongly affected lipid structure and organization, especially for monolayers in their lipid condensed phase [66]. Adding salt to the aqueous subphase amplifies these effects. Again the impact is more pronounced for DPPC monolayers in their liquid condensed state. PHFs are known to aggregate in solution and NaCl is often added to inhibit this effect. Assuming that PHFs in 500 mM NaCl solutions are present as monomers and in pure Millipore as aggregates, we interpret the results in terms of different species – monomers vs. aggregates – interacting with the

DPPC monolayer, affecting monolayer energetics, average DPPC monomer conformation, and DPPC monolayer thickness. Earlier work established that PHF solutes in aqueous solution, even when very dilute, were drawn to a water–air interface covered with DPPC through a cooperative adsorption mechanism [66]. Adding salt to the solution adds chemical complexity to the system in ways that change how PHF associates with deposited Langmuir films.

4.2 Experimental Methods

4.2.1 Materials

Dipalmityolphosphatidylcholine (DPPC) was purchased from Avanti Polar Lipids Inc. (powder, >99% purity; Alabaster, AL) and used as received. PHFs were purchased from American Elements (Los Angeles, CA) and used as received. The PHFs themselves consisted of a mixture of species having the general formula $C_{60}(OH)_n{\cdot}H_2O_m$, where $n = 22 \pm 2$ (determined by SEC-HPLC), $m > 8$). Sodium chloride used was purchased from Sigma-Aldrich (99.999% purity; St. Louis, MO). HPLC-grade chloroform, used as the DPPC spreading solvent, was purchased from Fisher Scientific (99.9% purity; Waltham, MA). The aqueous subphase used was water from a Millipore filtration system (Synergy® by Millipore). Before any addition of lipids or PHFs, the subphase had a resistivity of 18.2 MΩ and a surface tension of 72.5 mN/m at 23 °C.

4.2.2 Preparation of Samples

Sample preparation has been described previously [62-64, 66, 67]. Aqueous samples were prepared with Millipore water. Aqueous polyhydroxylated fullerene stock solutions (0.5 mg/mL) were prepared in 0, and 500 mM NaCl, with Millipore water, and sonicated for 5 min. The polyhydroxylated fullerene stock solutions were used to prepare aqueous PHF mixtures of 0.0075, 0.03, 0.06, 0.125, and 0.5 mg/mL. DPPC lipid stock solutions (~0.4-0.7 mg/mL) were prepared in chloroform and sonicated for 10 min. Aqueous PHF samples for VSFG and SE measurements were prepared in borosilicate Petri dishes. The Petri dishes were rinsed with methanol, acetone, and Millipore water several times prior to acid-washing (50/50 vol. nitric/sulfuric), and then rinsed with Millipore water several times before use. Surface tension measurements of these systems show PHFs to be very weakly surface active with surface concentrations of $6.4*10^{13}$ and $2.5*10^{13}/cm^2$ (in 0 and 500 mM NaCl respectively) at the highest bulk concentrations used in these studies (see Figure 4.1 and Table SI-4.1). A Hamilton glass microsyringe was used to apply the appropriate amount of the DPPC/chloroform stock solution to the aqueous subphase surface to ensure the desired surface coverages of 40 and 55 $Å^2$/molecule. DPPC was deposited on 0 and 500 mM NaCl subphases, both with and without PHFs, at the two desired surface coverages. After depositing the DPPC at the aqueous – air interface, the sample was allowed to sit for ≥ 5 minutes so that the chloroform could evaporate and the DPPC monolayer could equilibrate prior to measurements.

4.2.3 Surface Tension and Langmuir Trough

Surface tension measurements were carried out using methods described previously [62-64, 66, 67]. Briefly, a NIMA Langmuir trough (Model 302LL) equipped with a NIMA PS4 pressure sensor was used to perform measurements. Paper Wilhelmy plates from Brown Waite Engineering were used to measure surface tension. To obtain Langmuir trough compression isotherms, Langmuir trough barriers were closed at a speed of 10 cm^2/min. Slowing this compression by a factor of 3 did not change observed results. Surface pressure (Π) was measured as a function of surface area. The surface pressure is the difference between the surface tension of the underlying neat liquid subphase (γ_0) and the surface tension resulting from the subphase and surfactant monolayer (γ), PHF solutions in this case, as shown in Equation 4.1. All data reported are the average of 1-5 measurements taken per sample.

$$(\Pi = \gamma_0 - \gamma) \text{ (Eqn. 4.1)}$$

By using the relationship in Equation 4.1 we obtain a concentration versus surface pressure plot. Treating adsorbed PHF solutes as soluble surfactants, we then used the Gibbs adsorption equation to determine limiting surface coverages (Eqn. 4.2):[140]

$$\Pi A = n * k * T * \ln\,[C] \text{ (Eqn. 4.2)}$$

$$\Gamma = \frac{d\Pi}{dln[C]} * \frac{1}{kT} \text{ (Eqn. 4.3)}$$

where Γ is the surface excess concentration. Equation 4.2 can be simplified to Equation 4.3 to approximate Γ, or surface excess, where $\frac{d\Pi}{dln[C]}$ is the slope of steepest ascent determined from a PHF concentration versus surface pressure plot.

Given that the PHFs are only weakly surface active, we can calculate excess free energies of mixing, ΔG_{mix}^{E} (Equation 4.4). In Equation 4.4, A_{12} is the area per molecule of a mixed monolayer, A_1 and A_2 are the area per molecule of a pure monolayer of one of the species in the mixed monolayer, and x_1 and x_2 are the mole fractions of each of the species in the mixed monolayer [62, 158, 159].

$$\Delta G_{mix}^{E} = \int_{\pi_1}^{\pi_2} N_A(A_{12} - x_1A_1 - x_2A_2)d\pi \text{ (Eqn. 4.4)}$$

We can further simply Equation 4.4. Because PHFs have a high solubility in aqueous solution (>50 mg/mL in H_2O), we can assume that DPPC (species 1) is the only species constrained to the water – air interface. Using this assumption, Equation 4.4 simplifies to Equation 4.5.

$$\Delta G_{mix}^{E} = \int_{\pi_1}^{\pi_2} N_A(A_{12} - A_1)d\pi \text{ (Eqn. 4.5)}$$

Therefore, by integrating the differences in area between the isotherm from the system of interest and that of pure DPPC as a function of surface pressure, the excess free energy of mixing can be determined. We note here that if the PHFs did not have an affinity for the DPPC monolayer, this integral would equal zero.

4.2.4 Vibrational Sum Frequency Generation Spectroscopy

Vibrational sum frequency generation (VSFG) is a second-order nonlinear optical spectroscopy technique that has been described in detail previously [53, 62-64, 66, 160]. VSFG becomes symmetry allowed at an interface, provided that species at the interface have a net polar ordering, when inversion symmetry is broken between centrosymmetric media [115]. To perform VSFG experiments, two oscillating electromagnetic fields at different frequencies (fixed visible 800 nm and a tunable IR) are overlapped both spatially and temporally on a surface of interest. The two oscillating electromagnetic fields couple through the 2nd order susceptibility tensor, $\chi^{(2)}$, and create a coherent nonlinear polarization equal in frequency to the sum of the two input frequencies, also known as the sum frequency.

In SFG experiments, the intensity of the SF signal, $I(\omega)$, is proportional to the square of the effective portion of the 2nd order nonlinear susceptibility, $\chi_{eff}^{(2)}$, as shown in Equation 4.6. The $\chi_{eff}^{(2)}$ consists of two parts, a resonant contribution ($\chi_{q,eff}^{(2)}$) and a non-resonant contribution ($\chi_{NR,eff}^{(2)}$). When the IR frequency (ω_{IR}) is resonant with a vibrational mode (ω_q) of surface species, the SF signal generated is resonantly enhanced, as displayed in Equation 4.7 [160]. This resonance enhancement allows us to ignore the non-resonant contribution ($\chi_{NR,eff}^{(2)}$) as it is significantly smaller than the resonant contribution ($\chi_{q,eff}^{(2)}$).

$$I(\omega) \propto \left|\chi_{eff}^{(2)}\right|^2 \text{ (Eqn. 4.6)}$$

$$\left|\chi_{eff}^{(2)}\right|^2 = \left|\chi_{NR,eff}^{(2)} + \sum \frac{\chi_{q,eff}^{(2)}}{\omega_{IR} - \omega_q + i\Gamma_q}\right| \text{ (Eqn. 4.7)}$$

All reported VSFG spectra were acquired under SSP polarization conditions (listed in order of sum, visible, and IR polarizations, respectively - $S_{sum}S_{vis}P_{IR}$). The SSP polarization combination samples a single $\chi^{(2)}$ element, $\chi^{(2)}_{iiz}$ and is sensitive to only those vibrations whose IR transition moment is aligned along the surface normal (assigned as the z-axis). VSFG spectra were then used to report r+/d+ ratios. r+/d+ ratios reported from VSFG spectra are the average of 1-5 measurements taken per sample.

The VSFG setup used has been described in detail elsewhere [62-64, 66]. Briefly, ~3.4 W from a Ti-Sapphire regenerative amplifier (Libra-HE, Coherent, 85 fs pulses, 1 kHz repetition rate, 800 nm) was coupled to an optical parametric amplifier (Coherent OPerA Solo). An 80/20 beam splitter reflects 80% of the 800 nm into a tunable Coherent OPerA Solo optical parametric amplifier to produce IR light. The 800 nm light and the IR light (centered at ~3.4 μm) are then aligned both spatially and temporally, and focused onto the sample of interest at 48 and 38°, respectively, from surface normal. The SF response is then collimated and isolated before being focused into a monochromator (SpectraPro-300i, Action Research Corporation). The SF response is then dispersed into a 1340 x 100 pixel CCD (PIXIS100B, Princeton Instruments).

4.2.5 Spectroscopic Ellipsometry

Spectroscopic ellipsometry measurements were carried out using methods described previously [66]. Briefly, measurements were performed on a J.A. Woollam RC-2 and data was analyzed in CompleteEASE, a modeling software distributed by J.A. Woollam. The beam from the instrument was calibrated in the source and detector prior to every measurement. The signal detected is the change in polarization upon the incident beam irradiating the sample, which is quantified through ellipsometric angles Ψ (amplitude ratio) and Δ (phase difference) in Equation 4.8.

$$\rho = \frac{R_p}{R_s} = \tan(\Psi)\, e^{i\Delta} \quad \text{(Eqn. 4.8)}$$

$$\varepsilon = 1 + \chi = (\mathrm{n} + \mathrm{ik})^2 = \sin^2 \phi_0 + sin^2\phi_0 + tan^2\phi_0 \left[\frac{1-\rho}{1+\rho}\right]^2 \text{(Eqn. 4.9)}$$

A sample of pure Millipore water matched with a mean standard error (MSE) of 0.99-2.28 at the start of the measurements to a model of water at 25 °C. The incident angle was set at 75° with the thickness set to fit. Once Ψ and Δ are measured, the complex reflectance ratio (ρ) (Equation 4.8) can be obtained and applied to Equation 4.9 to derive optical constants (i.e. film thickness) of lipid films at the air – water interface [119-122]. SE measurements were used to report thicknesses. Monolayer thicknesses reported from SE experiments are the average of 6 measurements taken per sample.

4.3 Results

4.3.1 Surface Tension and Langmuir Trough

To address whether salt changes how soluble PHFs associate with insoluble DPPC monolayers, our initial studies focused first on how dissolved salt changes the surface activity of PHFs themselves. Briefly, solutions with various PHF concentrations were prepared, in Millipore water and in 500 mM NaCl, and the surface tension of each sample was measured. According to Equations 4.2 and 4.3, plotting surface pressure as a function of the natural log of PHF concentration shows PHF surface coverage. Data for each family of solutions – Millipore and 500 mM NaCl – are shown in Figure 4.1.

Earlier studies demonstrated that PHFs in Millipore are, in fact, surface active with a terminal monolayer coverage of 7.7 x 10^{13}/cm^2 (or 130 Å^2/molecule) at PHF concentrations of ~50 mg/ml [66]. Conductivity measurements showed that PHFs carried on average a -4 charge *and* departure from ideal solute behavior started at concentrations as low as 0.04 mg/ml implying a low-concentration onset of aggregation [188]. Adding salt to solution reduces but does not eliminate PHF surface activity. The effects of dissolved NaCl are apparent from the lower terminal surface pressures relative to pure Millipore as well as a shallower slope in the surface pressure rise (Figure 4.1). Using Equation 4.3, we calculate a terminal surface coverages of 2.5 x 10^{13}/cm^2 PHF coverages for the 500 mM NaCl solution, corresponding to ~400 Å^2/molecule. (See Table SI-4.1 in Supporting Information for surface coverages at different PHF concentrations.) Furthermore, terminal surface coverage is achieved at lower bulk PHF concentrations relative to the pure Millipore system, supporting the premise that the NaCl solutions have higher concentrations of monomers and the monomers are adsorbing to the surface. Interestingly, these observations also raise the question of whether PHFs are adsorbing to the pure water–air interface as monomers or as aggregates. Experiments described in this study are unable to resolve this issue.

DPPC compression isotherms were acquired on a Langmuir trough having different amounts of PHF and NaCl present in the subphase (Figure 4.1). The pure DPPC isotherm lifts off between 100-110 Å^2/molecule) and passes through a liquid expanded-liquid condensed coexistence region between 90 Å^2/molecule and 60 Å^2/molecule. The monolayer collapses with a terminal surface coverage of 44 Å^2/molecule, in agreement with previous literature reports [62-64]. The isotherms deviate significantly more from each other at 55 Å^2/molecule in the presence of salt when compared to the pure Millipore isotherms previously reported [66]. Specifically, increasing NaCl concentration pushes the isotherms to higher areas per molecule, as evidenced in Figure 1a. This effect is modest in the absence of any PHF in solution but becomes quite apparent as PHF concentration increases to 0.125 mg/ml. The effects are most pronounced in the 500 mM NaCl solution. The shift to higher areas per molecules in the DPPC isotherms with the addition of salt (no PHFs present) is consistent with literature [174, 176, 177]. The π – area data from DPPC in the presence of PHFs is expanded with DPPC taking up a larger mean molecular area (MMA) at a given surface pressure. This increase can result from PHF integration into the monolayer causing a larger overall footprint (or MMA) for DPPC monomers and hints at specific, cooperative interactions between the soluble PHF and the insoluble DPPC. Complementary vibrational spectroscopy data shown below will reveal that this cooperative adsorption of the PHFs to the surface affects structure and organization within the DPPC monolayers.

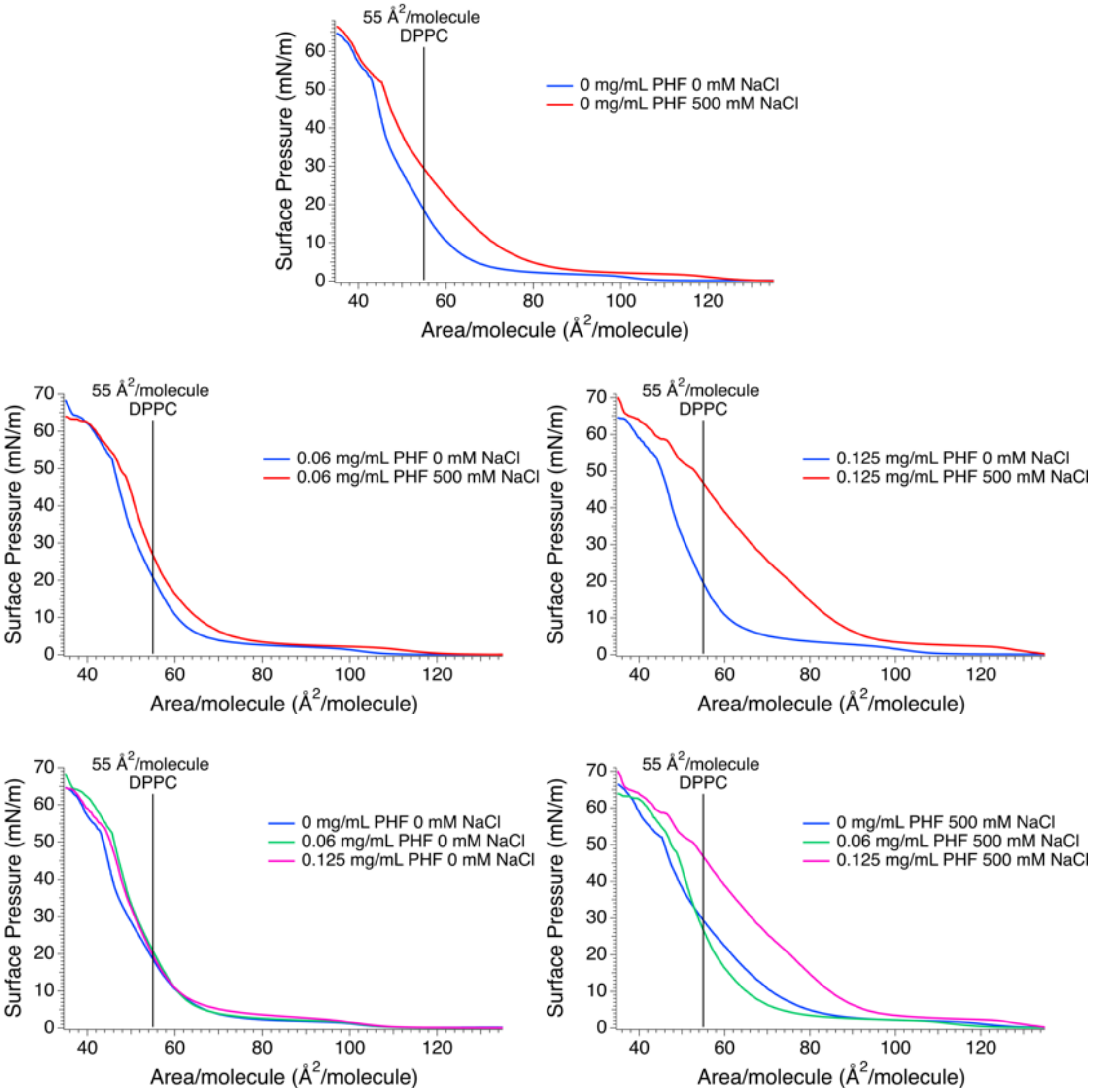

Figure 4.1a. Langmuir trough compression isotherms of DPPC with varying NaCl subphase (top). Langmuir trough compression isotherms of DPPC with 0.06 mg/mL PHF with varying NaCl subphase (middle left). Langmuir trough compression isotherms of DPPC with 0.125 mg/mL PHF with varying NaCl subphase (middle right). Langmuir trough compression isotherms of DPPC with varying PHF and 0 mM NaCl (bottom left). Langmuir trough compression isotherms of DPPC with varying PHF and 500 mM NaCl (bottom right).

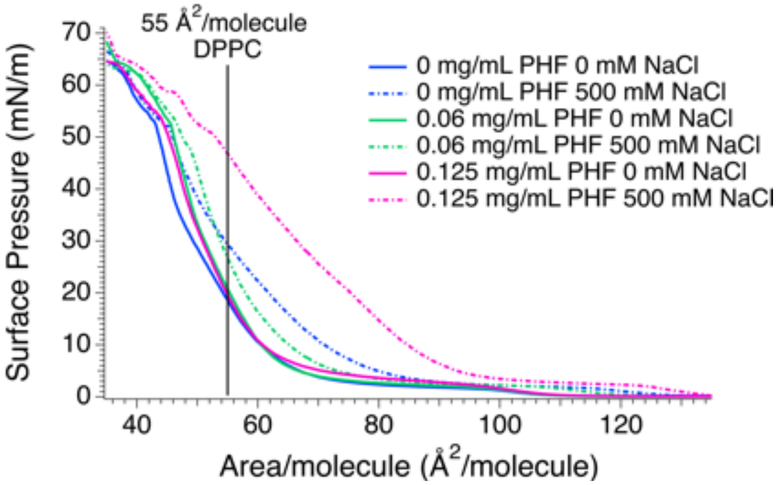

Figure 4.1b. Langmuir trough compression isotherms of DPPC with varying PHF and varying NaCl subphase.

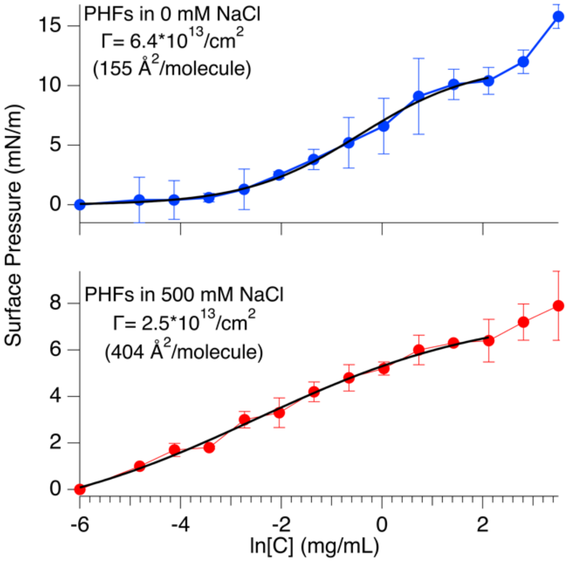

Figure 4.1c. Terminal surface coverages of PHFs in 0 mM NaCl (blue trace) and in 500 mM NaCl (red trace). Black lines are empirical fits of the data to a sigmoidal function and are used to calculate slopes at different bulk solution PHF concentrations.

4.3.2 Excess Free Energy of Mixing

As described previously, integrating the differences in area between the isotherm from the system of interest and that of pure DPPC as a function of surface pressure provide information about the energetics of mixed monolayer formation [66]. A positive ΔG^{EX} value typically reflects a more expanded mixed monolayer relative to the weighted sums of the pure components, while a negative ΔG^{EX} value implies that the mixed monolayer is more compressed with attractive interactions between the constituent components. Such an interpretation is misleading here. The isotherms in Figure 4.1 show that at a given surface pressure, the small amount of PHF in solution leads to a larger DPPC MMA, but if PHFs are being drawn to the surface through cooperative interactions, then their adsorption from the bulk to the water – air interface will force the DPPC monomers themselves to become *more* tightly packed. Similar results have been reported before with soluble alkyl surfactants and with simple monosaccharides [62, 63, 161]. VSFG data below suggest that such a picture accurately describes the effects of PHFs on DPPC monolayers in the liquid condensed state (55 Å^2/molecule). Langmuir trough compression isotherm data from Figure 4.1 were analyzed using excess free energy expressions shown in Equations 4.4 and 4.5. ΔG^{EX} values in Figure 4.2 show positive excess free energies, consistent with PHF cooperative adsorption, and although the excess free energies are small, they have measurable effects on monolayer structure. When determining excess free energies by comparing the isotherms from that of pure DPPC, the ΔG^{EX} values deviate as we increase PHF concentration, but the largest change is seen with the highest NaCl concentration. (*Vide infra.*)

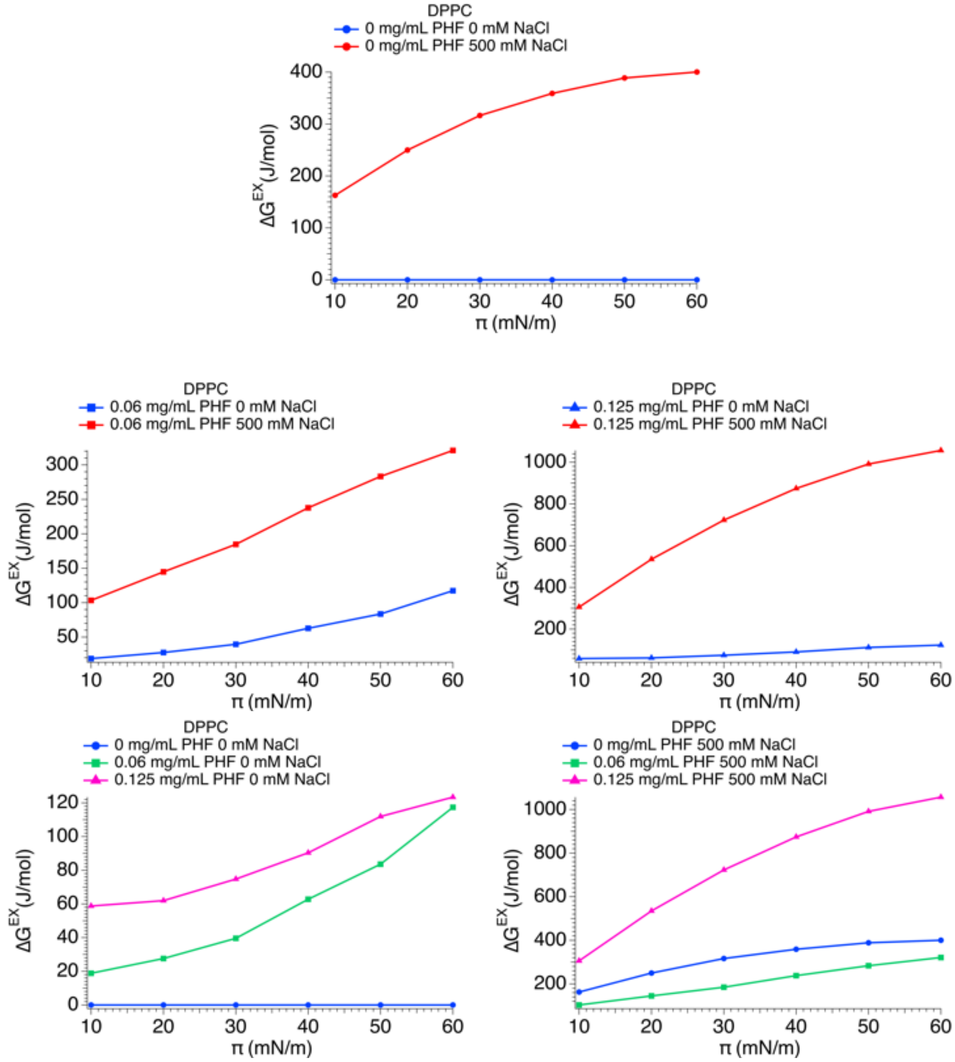

Figure 4.2a. Excess free energy of mixing of DPPC with varying NaCl subphase (top). Excess free energy of mixing of DPPC with 0.06 mg/mL PHF with varying NaCl subphase (middle left). Excess free energy of mixing of DPPC with 0.125 mg/mL PHF with varying NaCl subphase (middle right). Excess free energy of mixing of DPPC with varying PHF and 0 mM NaCl (bottom left). Excess free energy of mixing of DPPC with varying PHF and 500 mM NaCl (bottom right).

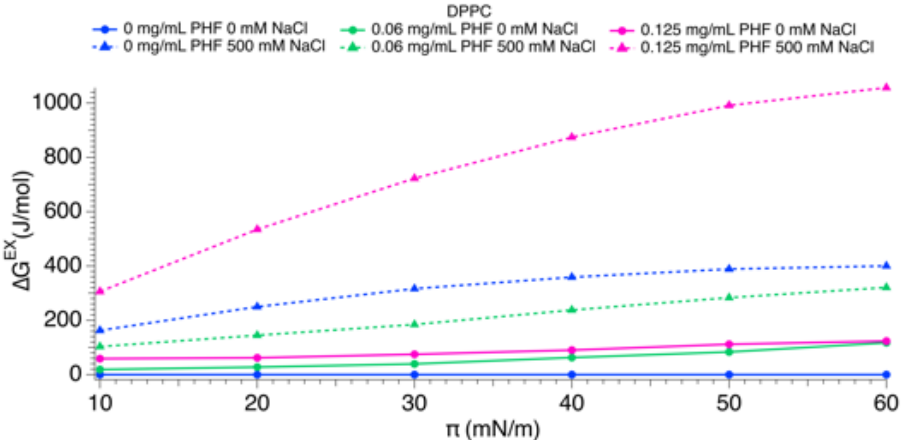

Figure 4.2b. Excess free energy of mixing of DPPC with varying PHF and varying NaCl subphase.

While thermodynamic data are instructive with regards to monolayer energetics and phase behavior, they do not provide information about molecular structure and organization. Discerning molecular structure and organization at interfaces is challenging due to the small number of molecules involved and the sometimes large, overwhelming responses from bulk solution responses. In order to determine how a solution's ionic strength changes PHF effects on DPPC monolayer structure and organization, VSFG was used to evaluate structure and organization in the liquid condensed and tightly packed DPPC monolayers as a function of solution-phase ionic strength. SE measurements were also performed to correlate changes in molecular structure with overall film thickness.

4.3.3 VSFG (Spectra & r^+/d^+ Ratios)

Figures 4.3 shows VSFG spectra in the CH stretching region of DPPC monolayers in their liquid condensed and tightly packed states on solutions of pure water and 500 mM NaCl. In Figure 4.3 ,"r" denotes vibrations associated with the methyl group of DPPC monomers and "d" describes vibrations associated with methylene groups [162,

[163]. The "+" indicates a symmetric stretch (SS) and a "-" indicates an antisymmetric stretch (AS). d^+ at 2850 cm^{-1} corresponds to a CH_2 SS, r^+ at 2874 cm^{-1} corresponds to a CH_3 SS, r^- at 2952 cm^{-1} corresponds to an out-of-plane CH_3 AS, r^- at 2962 cm^{-1} corresponds to an in-plane CH_3 AS, and r^+_{FR} at 2930 cm^{-1} corresponds to a CH_3 Fermi resonance interaction [64, 117]. Note that the y-axes report intensities in 'arbitrary units' (au) and should not be compared directly between both spectra in Figure 4.3. A better indicator of the absolute signal intensities in the two spectra can be inferred from each spectrum's S/N. Spectra from the more expanded, liquid-condensed (loosely packed at 55 $Å^2$/molecule) monolayer are much weaker than those from tightly packed monolayers (tightly packed at 40 $Å^2$/molecule).

Following convention, the ratio of the r^+ and d^+ intensities often serves as a sensitive indicator of alkyl chain conformational order [164-166]. Under SSP conditions, a well-ordered monolayer with alkyl chains in an all-*trans* conformation aligned predominantly along the surface normal will show a strong r^+ band and a weak d^+ band. The strong r^+ results from the terminal methyl groups aligned with their local C_3 axes (and IR transition moments) directed in the laboratory z-axis. Two considerations lead to a weak d^+ band in this well-ordered system: first, if the chains are all-*trans* and aligned along the surface normal, the CH_2 symmetric (and antisymmetric) IR transition moments will be aligned in-plane and will not be accessible to an SSP polarization combination. Second, an all-*trans* chain will have local inversion symmetry about each carbon-carbon bond making the d^+ transition symmetry forbidden in VSFG experiments. The introduction of *gauche* defects to the chain leads to more conformational disorder, a weaker r$^+$, and the appearance of symmetry allowed d$^+$ transitions. The r+/d+ ratio will serve as an important indicator of how DPPC monolayers are affected by soluble PHFs as a function of solution-phase ionic strength. We note that the PHFs themselves have no VSFG active features in the region of interest.

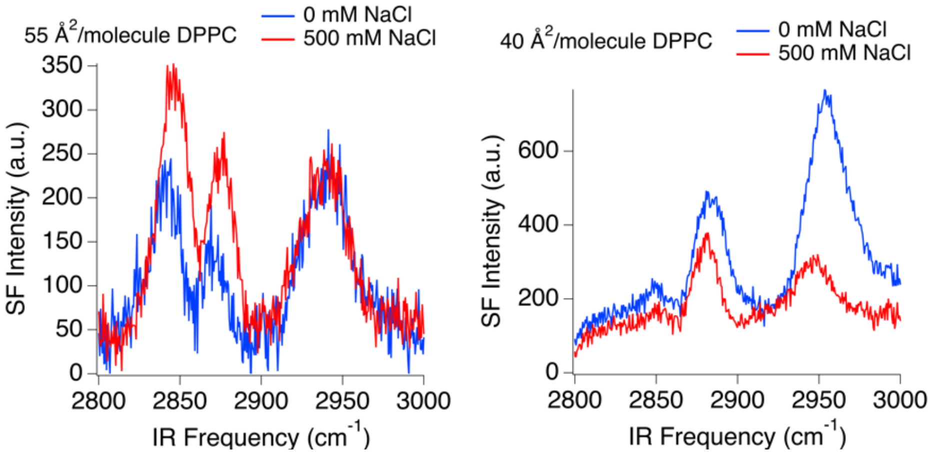

Figure 4.3. VSFG spectra of 55 Å^2/molecule DPPC on 0 and 500 mM NaCl at SSP polarization with peak assignments (left). VSFG spectra of 40 Å^2/molecule DPPC on 0 and 500 mM NaCl at SSP polarization with peak assignments (right).

Figure 4.4 shows resonant SFG contributions from loosely packed and tightly packed DPPC monolayers with varying PHF concentration as a function of solution-phase ionic strength. Although the data are baseline corrected relative to a pure water – air interface, addition of PHF to the aqueous solution leads to a changing baseline. Because prior analysis of reflectivity data shows that the surface reflectivity remains constant for all PHF concentrations, the changing baseline is not attributed to a change in reflectivity [66]. As a result, we assign this effect to broadband fluorescence from PHFs adsorbed to the surface and in solution. The relative intensities are changing in a way that becomes clearer to see when the r+/d+ ratios are plotted (Figure 4.5).

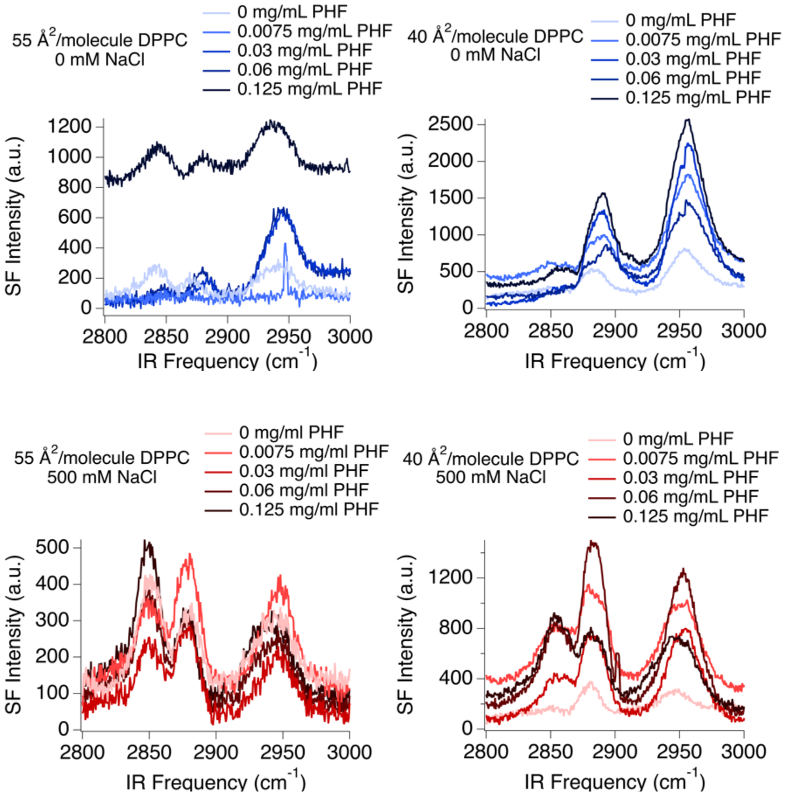

Figure 4.4. VSFG spectra of 55 Å^2/molecule DPPC on different NaCl concentration subphases with varying PHF concentrations (all at SSP polarization) (left). VSFG spectra of 40 Å^2/molecule DPPC on different NaCl concentration subphases with varying PHF concentrations (all at SSP polarization) (right).

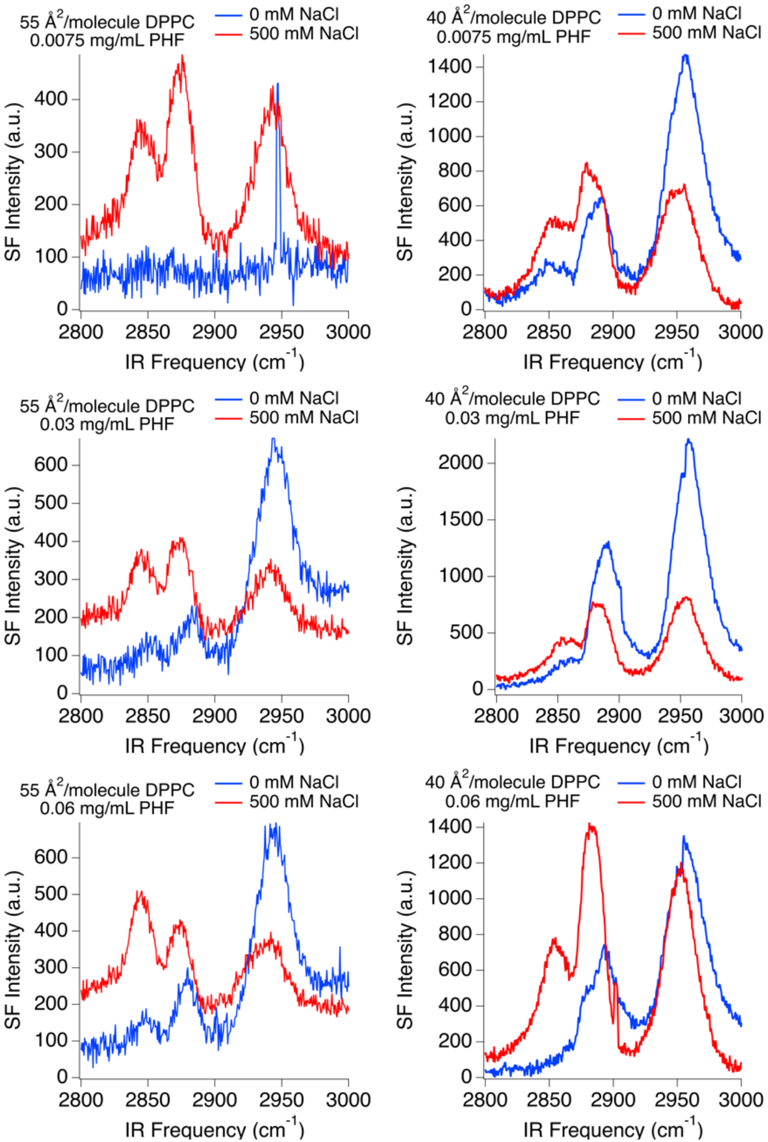

Figure 4.4 continued. VSFG spectra of 55 Å^2/molecule DPPC on different NaCl concentration subphases with varying PHF concentrations (all at SSP polarization) (left). VSFG spectra of 40 Å^2/molecule DPPC on different NaCl concentration subphases with varying PHF concentrations (all at SSP polarization) (right).

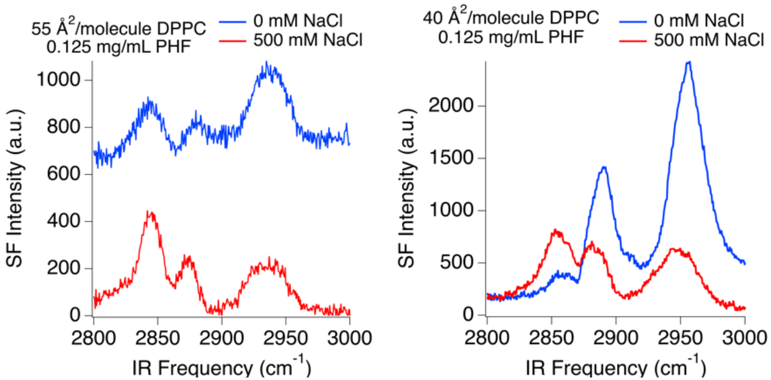

Figure 4.4 continued. VSFG spectra of 55 Å^2/molecule DPPC on different NaCl concentration subphases with varying PHF concentrations (all at SSP polarization) (left). VSFG spectra of 40 Å^2/molecule DPPC on different NaCl concentration subphases with varying PHF concentrations (all at SSP polarization) (right).

The VSFG spectra as a function of PHF concentration show that dissolved NaCl changes how PHFs affect DPPC monolayer organization. These changes are most evident when comparing the r^+/d^+ intensity ratios from the different spectra. Figure 4.5 shows r^+/d^+ ratios for loosely packed and tightly packed DPPC monolayers with varying PHF concentration for the different NaCl concentrations. These ratios were calculated from spectra acquired with an $S_{sum}S_{vis}P_{IR}$ polarization combination. Traditionally, a larger r^+/d^+ ratio is associated with a more ordered monolayer with chains adopting all-*trans* conformations and aligned along the surface normal. In light of monolayer thickness results described below, we note that the all-*trans* conformation will lead to low intensity in the d^+ band due to local inversion symmetry about each carbon-carbon bond, but if the monolayer adopts a net chain tilt away from surface normal, this behavior will leave the methyl symmetric stretch (r^+) with less of its IR transition moment projected along the surface normal. The net result will be a smaller r^+/d^+ ratio but the origin will be monolayer tilt within the monolayer rather than increased conformational disorder.

Figure 4.5 shows that, in neat Millipore (0 mM NaCl), increasing PHF concentration up to 0.06 mg/ml increases the liquid condensed monolayer's r^+/d^+ ratio. In earlier work, this effect was attributed to PHF solutes in bulk solution being drawn to the surface and effectively compressing the DPPC film [66]. This behavior would lead to the expanded monolayers observed in the Langmuir trough experiments in Figure 4.1 and the corresponding positive ΔG_{excess} reported in Figure 4.3. The r^+/d^+ ratio for DPPC liquid condensed films on a 500 nM NaCl solution rises sharply at the lowest concentration before tailing off monotonically at higher PHF concentrations. This result observed for the 500 mM/0.0075 mg/ml PHF system is consistent with more monomers adsorbing to the surface at lower concentrations than in the Millipore/PHF system. Again, as with the Millipore system, PHF adsorption will effectively compress the liquid compressed monolayer leading to an increase in r^+/d^+. The data in Figure 4.5 imply that PHF adsorption happens more readily at lower concentrations when salt is present. This result is consistent with the hypothesis that PHF monomers are responsible for cooperative adsorption to the lipid monolayer, and that in the NaCl solution PHFs are present primarily as monomers. In (salt-free) Millipore water, PHF monomers are believed to aggregate at very low concentrations ($\leq$ 0.03 mg/ml), and if the aggregates are less surface active than monomers, then higher bulk PHF concentrations will be needed before a sufficient number of monomers in solution are available to adsorb to the surface.

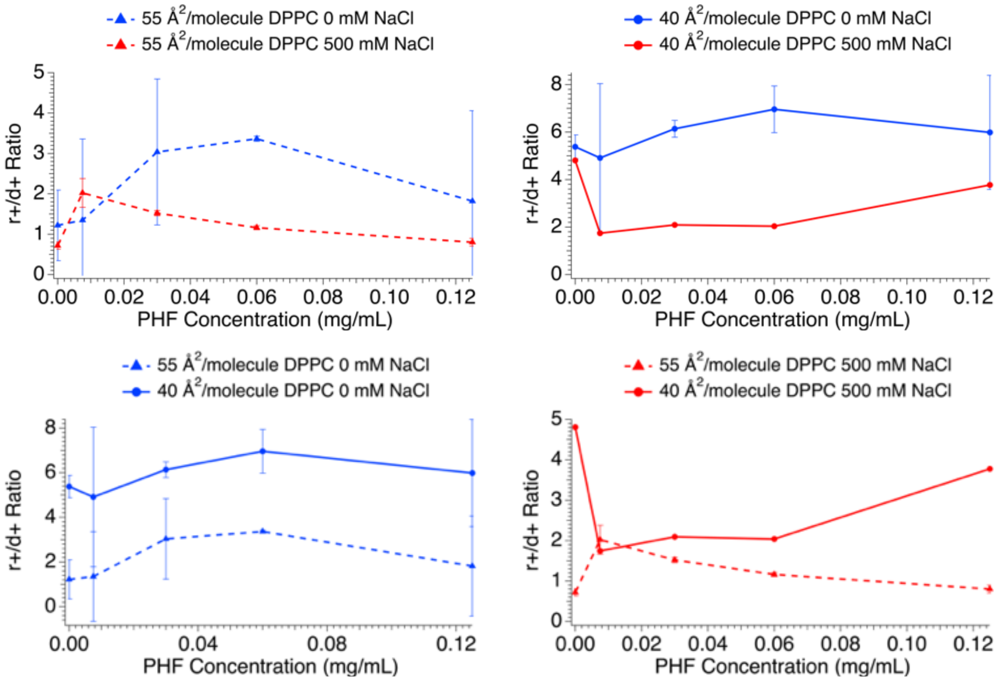

Figure 4.5. Combined VSFG r+/d+ ratio of 55 Å^2/molecule DPPC on varying NaCl concentration subphases with PHFs (top left). Combined VSFG r+/d+ ratio of 40 Å^2/molecule DPPC on varying NaCl concentration subphases with PHFs (top right). Combined VSFG r+/d+ ratio of 55 and 40 Å^2/molecule DPPC on 0 mM NaCl subphase with PHFs (bottom left). Combined VSFG r+/d+ ratio of 55 and 40 Å^2/molecule DPPC on 500 mM NaCl subphase with PHFs (bottom right).

In the high surface coverage limit, DPPC monolayers start out highly ordered with r^+/d^+ ratios between 5 and 6 on both the Millipore and 500 mM NaCl solutions in the absence of PHFs. Adding PHF to the subphase does not have a large effect on the r^+/d^+ ratio for tightly packed DPPC on Millipore, but r^+/d^+ ratio drops dramatically on the 500 mM NaCl solution when PHFs are present at low concentration (Figure 4.5). The ratio then climbs modestly with increasing PHF concentration. Unlike DPPC monolayers in their liquid condensed state, tightly packed monolayers do not have vacant interstitial space at the surface where PHF solutes can adsorb. The fact that adding PHF *does* impact r^+/d^+ for tightly packed monolayers on the 500 mM NaCl solution further supports a cooperative adsorption mechanism that attracts PHF monomers to the DPPC headgroups. However, unless PHFs (at very low bulk concentrations) are forcing the DPPC monolayer to form multilayers or buckle to encapsulate adsorbed PHF monomers, the only rationalization for changes in r^+/d^+ for these tightly packed monolayers hinges upon an overall tilt to the adsorbed lipid film.

4.3.4 Spectroscopic Ellipsometry

To independently test how dissolved NaCl affects PHF-DPPC interactions, we examined monolayer thickness using spectroscopic ellipsometry. We note that when NaCl is present, PHF surface coverages diminish and, as noted earlier, we assume that the PHFs that *do* adsorb do so as monomers and not aggregates. SE data were used to calculate film thicknesses as described in the Experimental Section and in previous reports [66, 167-169]. Data for liquid condensed and tightly packed DPPC monolayers as a function of PHF concentration with and without NaCl are shown in Figure 4.6.

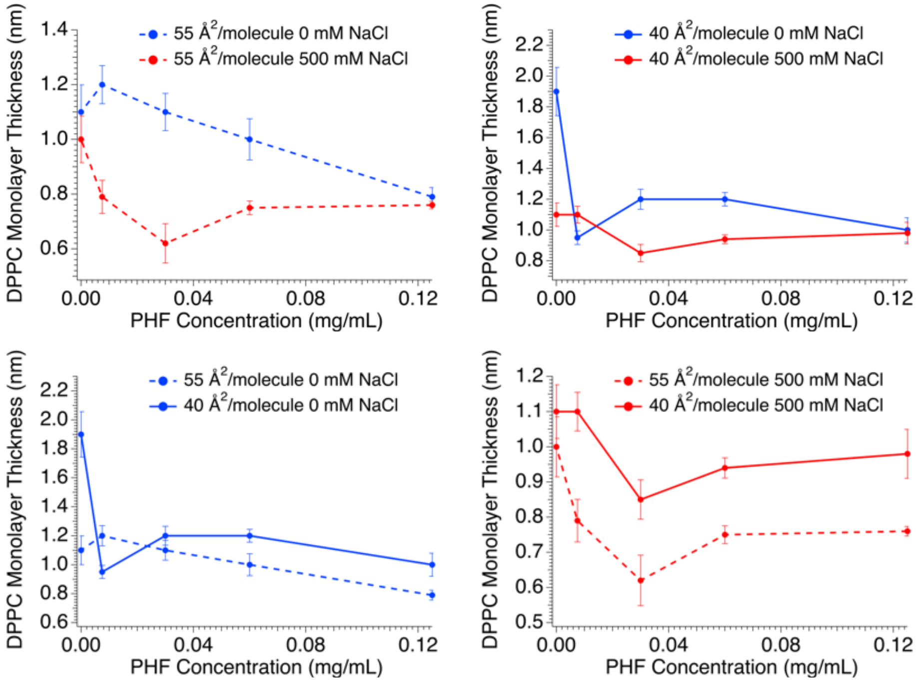

Figure 4.6. 55 Å^2/molecule DPPC monolayer thickness on varying NaCl/PHF subphase (top left). 40 Å^2/molecule DPPC monolayer thickness on varying NaCl/PHF subphase (top right). 55 and 40 Å^2/molecule DPPC monolayer thickness on 0 mM NaCl subphase with PHFs (bottom left). 55 and 40 Å^2/molecule DPPC monolayer thickness on 500 mM NaCl subphase with PHFs (bottom right).

Previous SE data has shown that small amounts of PHF in the subphase lead to systematic changes in DPPC monolayer thickness, and the data further support a cooperative adsorption hypothesis [66]. In the absence of any PHF in solution, the tightly packed monolayer is 1.9 nm thick, and the loosely packed monolayer is 1.1 nm thick, values consistent with previous reports [167-169]. The thickness for the loosely packed lipid film is consistent with a ‘thinner’, more disorganized monolayer and the correspondingly small r^+/d^+ ratio observed in the VSFG data. Relative to the PHF-free case in 0 mM NaCl, adding even a small amount (0.0075 mg/ml) of PHF to the solution leads to a measurable increase in monolayer thickness for a loosely packed monolayer, but a decrease in monolayer thickness for a tightly packed monolayer (Figure 4.6). When the subphase includes 500 mM NaCl, the DPPC film decreases in thickness for both the liquid condensed and tightly packed monolayers. Given our assumption that PHFs in 500 mM NaCl solutions are present as monomers and in pure Millipore as aggregates, these results hold consistent in that there is a decrease in DPPC film thickness in the presence of 500 mM NaCl, but an increase in film thickness in 0 mM NaCl – aggregates taking up a larger footprint than monomers would force the lipids in a more vertical orientation.

4.4 Discussion

The studies described here were premised on the hypothesis that salt changes the interactions between PHFs and insoluble lipid monolayers. This hypothesis emerged from 1) reports that suggesting that dissolving simple salts such as NaCl into solution would inhibit PHF aggregation and 2) recent discoveries that demonstrated PHFs in very dilute concentrations in Millipore water interact with DPPC monolayers through a proposed cooperative adsorption mechanism [66, 144]. To test how dissolved salt affected PHF-DPPC interactions, several independent methods including surface tensiometry, VSFG spectroscopy and spectroscopic ellipsometry were used to quantify the surface behavior of these complex chemical systems.

Two different types of surface tension measurements were performed and both proved very instructive. First, simple surface tension measurements tested PHF surface activity in both Millipore water and 500 mM NaCl solutions. The data (Figure 4.1) showed that while PHFs retain a measure of surface activity in the NaCl solution, the terminal surface coverage as determined by a Gibbs isotherm expression is less than that in a pure Millipore solution. Terminal monolayer coverages in the two systems are 6.4

and 2.5 molecules/cm^2 at the water – air interface when bulk concentrations approach 0.519 and 0.130 mg/ml for 0 and 500 mM NaCl respectively. Fitting these data lead to adsorption energies of -29 (±7) (0 mM NaCl) and -21 (±7) (500 mM NaCl) kJ/mole [102].

Second, as evidenced by their terminal surface coverages, even though PHFs are not strongly drawn to the water – air interface, their presence in solution has readily observable effects on DPPC monolayer compression isotherms that suggests a cooperative adsorption mechanism. This cooperative adsorption mechanism is enhanced in the presence of dissolved NaCl. Specifically, even at the lowest PHF bulk concentration tested in this work (0.0075 mg/ml) where surface coverages at the neat water – air interface are on the order of $1.8*10^{13}$ molecules/cm^2, the presence of dissolved NaCl increases ΔG^{E}_{excess}, leading the DPPC isotherm to lift off at larger areas and have consistently larger DPPC MMAs relative to DPPC on a pure water subphase. Because NaCl has been shown to inhibit PHF aggregation, we interpret this effect in terms of monomer adsorption to the surface. In the *absence* of NaCl, PHF monomers in solution can either aggregate and remain in bulk solution *or* adsorb to the surface. In the *presence* of NaCl, aggregation is suppressed and monomers can either remain in solution or adsorb to the surface. A higher fraction of monomers (relative to aggregates) in bulk will lead to more monomers adsorbing to the water – air interface at lower concentrations. These data also imply that the higher surface pressures and surface excess concentrations observed in the pure Millipore system are the result of both monomer and aggregate adsorption.

In order to test how salt altered PHF effects on DPPC monolayer structure and organization, VSFG measurements were performed at DPPC surface coverages of 55 Å^2/molecule (liquid condensed phase) and 40 Å^2/molecule (tightly packed) with 500 mM NaCl subphases and results were compared to equivalent experiments conducted with PHF solutions in pure Millipore water. A ratio of r^+/d^+ intensities were used as a measure of organization within the DPPC monolayer, where a larger r+/d+ ratio corresponds to acyl chains having primarily all-*trans* conformations and typically aligned along the surface normal. Data in Figure 4.5 show that when PHFs are added to solution, the r^+/d^+ ratio initially rises for liquid condensed monolayers. This change is gradual for DPPC monolayers on Millipore water but abrupt for DPPC on the 500 mM NaCl solution. With increasing concentration the r^+/d^+ ratio becomes smaller, again with the results more gradual for the Millipore system and more pronounced for the 500 mM NaCl system. These findings are consistent with data from the DPPC Langmuir trough isotherms that show DPPC/PHF systems at 55 Å^2/molecule having higher surface pressures on the saline subphase. Assuming that PHFs in the NaCl solution are present only as monomers, PHF adsorption to a surface covered by DPPC in its liquid condensed state will more effectively compress the DPPC to become closely packed with greater conformational order. The same effect – PHF monomer adsorption – will also change organization in the DPPC liquid condensed film on Millipore but at higher PHF concentrations.

For tightly packed monolayers the r^+/d^+ data do not lend themselves to a straightforward interpretation. For the tightly packed monolayer on Millipore water, the

r^+/d^+ ratio appears largely insensitive to PHF subphase concentration. To the extent that tightly packed monolayers have no remaining vacant interstitial space at the water–air interface, such behavior may not be surprising. The monolayer is tightly packed and no change in the subphase will change that condition. However, r^+/d^+ for the tightly packed DPPC monolayer on the 500 mM NaCl solution shows a 60% drop in its value with the addition of small amounts of PHF to the subphase. The r^+/d^+ ratio then slowly increases as additional amounts of PHF are added to solution. If we assume that a tightly packed monolayer has very little opportunity become disordered, then we are left to interpret the data in Figure 4.5 as indicating an overall tilt in the monolayer as monomers adsorb to the modified water–air interface, leading to a decreased monolayer thickness as evidenced in Figure 4.6.

Monolayer thicknesses measured by spectroscopic ellipsometry do not, by themselves, provide a clear picture of how DPPC film structure is changing with the addition of PHFs to Millipore and NaCl solutions. However, when these results are considered in the context of changing r^+/d^+ ratios, thicknesses derived from SE measurements provide complementary information and insight.

For liquid condensed monolayers, film thickness rises modestly on Millipore water when small amounts of PHF are added to the subphase. This result is consistent with DPPC islands in the liquid condensed phase becoming compressed and more ordered with the adsorption of PHF monomers and standing more upright. In contrast, film thickness in the liquid condensed phase shrinks by 40% (1.0 nm to 0.6 nm) when PHFs are added to the NaCl subphase, even as the DPPC monomers themselves are showing a larger r^+/d^+ ratio rises. Keeping in mind that there are more monomers than aggregates adsorbed to the surface in the presence of NaCl which have a smaller footprint leading to more remaining vacant interstitial space, we interpret these results to signal that while the DPPC on a salt solution becomes more ordered with PHF monomer adsorption, the monolayer itself also tilts, accounting for the reduction in thickness. As more PHF is added to the solution, DPPC film thickness on Millipore begins to shrink gradually (while r^+/d^+ stays approximately constant, indicating tilt) while the film thickness on the NaCl solution rises. At a PHF concentration of 0.125 mg/ml, the film thicknesses are equivalent, regardless of subphase composition. With the tightly packed monolayers, the presence of NaCl in the subphase results in consistently smaller film thicknesses and again, this difference is attributed to a net tilt to the monolayer itself.

4.5 Conclusions

Results reported here use independent but complementary optical and thermodynamic techniques to examine the effects of salt on PHF-DPPC interactions. The studies focus on building upon prior used model systems having well-controlled lipid compositions and a variety of PHF concentrations, but adding complexity to the model system by introducing NaCl to the system to determine the mechanism(s) responsible for carbon particulate accumulation at the water – air interface, and how specific thermodynamic and optical properties of DPPC at the water – air interface change with the inclusion of PHFs as a function of ionic strength. Using PHFs as model aerosol particulates, and using DPPC as a model for lung surfactant, data that the soluble PHFs are drawn to the lipid covered water – air interface through a cooperative adsorption mechanism, *and* that this effect is observable even at very low PHF concentrations. Furthermore, we have determined that NaCl inhibits PHF aggregation at the water – air interface. For lipid monolayers in both their loosely and tightly packed states, PHF adsorption (from bulk solution) in 0 mM NaCl effectively compresses the DPPC monolayer making the acyl chains more ordered, but adding salt to the system lead to an overall tilt in the DPPC film as evidenced by a decrease in monolayer thickness. One possible interpretation is that, in the presence of NaCl, more monomers are adsorbed to the surface, leaving sufficient free interstitial space available to the lipid film. The decrease in r+/d+ ratios as a function of NaCl concentration (suggesting less acyl ordering) and the decrease in monolayer thickness as a function of NaCl concentration align with the hypothesis that PHFs in NaCl induce a net 'tilting' of the monolayer away from surface normal leading to a monolayer that appears less well ordered (according to the r^+/d^+ order parameter) with a decreased monolayer thickness. From a physiological perspective, results presented in this work suggest that carbon particulates, especially those that are at the very small end of $PM_{2.5}$ (particulate matter <2.5 μm in diameter) range may remain enriched at the alveoli water – air interface rather than dissolving into the alveoli's water-based subphase.

CHAPTER FIVE

CONCLUSIONS AND FUTURE DIRECTIONS

5.1 Summary

Work presented in this thesis examined cooperative adsorption as a means of describing PHF particulates interacting with DPPC monolayers [65, 66, 101]. Ultimately, these interactions will play a role in controlling lung-surfactant behavior in the presence of non-biological nanoparticles.

Initial work focused on choosing a representative model system to study black carbon – lung surfactant interactions at a biologically-relevant aqueous – air interface. The model system chosen consisted of PHFs as surrogate species for aged BC, and of DPPC monolayers as a model for lung surfactant. As previously mentioned, the importance of aqueous – air interfaces has been well-recognized, but majority of the studies conducted at water interfaces at the molecular level are recent [53-56] because of the limited number of surface-specific techniques capable of probing these chemically complex interfaces with molecular specificity [53]. After establishing a model system, a host of complementary surface-specific techniques including Langmuir trough and surface tension measurements, second harmonic generation and vibrational sum frequency generation spectroscopy, and spectroscopic ellipsometry were used to study the effects of PHFs on DPPC monolayers adsorbed to the at the aqueous – air interface.

Chapter 2 examined PHF surface activity and aggregation behavior at the air – water interface using surface tension and resonance enhanced second harmonic generation. Surface tension data showed that PHFs are surface active with a limiting surface excess corresponding to 155 Å^2/molecule in aqueous (Millipore water) solutions. Increasing solution phase ionic strength (through the addition of NaCl) reduces PHF surface excess. Conductivity measurements show that PHFs carry a presumably negative charge (-4). Surface specific SHG experiments show a small but measurable fixed-wavelength, nonlinear response from solutions having surface excess coverages as low as ~400 Å^2/molecule. The SHG response of PHF solutions in the low-concentration limit shows unexpected behavior, implying that at bulk concentrations above 0.12 mg/ml (and a surface coverage of 4.0 x 10^{13} molecules/cm^2 or 250 Å^2/molecule), PHFs adsorb to the surface as dimers or higher aggregates and only at low concentrations do monomers contribute to the measured SHG response.

Chapter 3 focused on using surface specific vibrational spectroscopy experiments together with surface tension measurements and spectroscopic ellipsometry data to characterize the effects of soluble carbon particulates on compressed and partially compressed lipid monolayers adsorbed to the water–air interface. The lipid monolayers consisted of dipalmitoylphosphatidylcholine (DPPC) and measurements were made for both tightly packed monolayers (40 Å^2/molecule) and monolayers in their liquid condensed state (55 Å^2/molecule). The soluble carbon particulates were poly-hydroxylated fullerenes (PHFs), chosen to mimic black carbon aerosols that have oxidized in the atmosphere and have become soluble in water. Data from surface tension measurements showed that even a very small amount of PHF (0.0075 mg/ml or 6.4*10^{-6} M of solution) decreases lipid film compressibility. This finding supports a cooperative adsorption mechanism whereby the soluble PHFs are drawn to, and associate with, the insoluble DPPC monolayer. Excess free energies for the system (ΔG_{mix}^{E}) were determined by comparing the DPPC/PHF isotherms with that from pure DPPC. ΔG^{EX} values showed positive excess free energies, consistent with PHF cooperative adsorption, and although the excess free energies were small, they had measurable effects on monolayer structure. Further support for the cooperative adsorption mechanism at the water – air interface came from surface specific vibrational sum frequency generation (VSFG) experiments. In solutions of pure Millipore water, low PHF concentrations ($\leq$ 0.06 mg/ml) increased DPPC acyl chain ordering in liquid condensed lipid films and decreased DPPC acyl chain ordering in tightly packed lipid films. DPPC film thickness in the liquid condensed phase also increased in this low PHF concentration regime according to spectroscopic ellipsometry measurements. Such behavior is consistent with PHF monomers or aggregates occupying surface area at the water – air interface, effectively compressing DPPC domains, forcing the lipids to adopt a more vertical orientation. Together, findings presented in Chapter 4 illustrated how independent measurement techniques can identify subtle but measurable interactions between atmospherically relevant particulates and lipid membranes and how these associations depend sensitively on a lipid film's thermodynamic state.

Chapter 4 built on discoveries reported in Chapter 3. Surface specific vibrational spectroscopy experiments together with surface tension measurements and ellipsometric characterization were used to examine the effects of changing ionic strength on PHF cooperative adsorption to DPPC monolayers. These studies were undertaken because dissolved sodium chloride is known to inhibit PHF aggregation. Data from surface tension measurements showed that, in the presence of salt, PHFs affect DPPC significantly more than in just pure Millipore water. Given that the PHFs are weakly surface active, excess free energies of mixing ($\mathit{\Delta} G_{mix}^{E}$) were determined by comparing the DPPC/PHF/NaCl isotherms with that from pure DPPC. ΔG^{EX} values showed positive excess free energies, consistent with PHF cooperative adsorption, and they had measurable effects on monolayer structure. In contrast to NaCl-free PHF solutions, adding salt to the aqueous PHF solution leads to lower r+/d+ ratios, suggesting a lipid that is more *disordered*. However, spectroscopic ellipsometry measurements showed DPPC thickness decreased as salt concentration increased, which, taken with the r+/d+ ratios, suggests a more *ordered* but *tilted* (decreased thickness) DPPC monolayer. Together, findings presented in this work illustrate how a host of independent measurements can be complementary in identifying how water-soluble black carbon aerosols induce organizational changes in lipid monolayers at the water – air interface as a function of solution-phase ionic strength.

Taken in their entirety, the experiments presented in this thesis represent a detailed investigation of 1) the mechanism(s) responsible for carbon particulate accumulation at lipid monolayer covered water–air interface, and 2) how specific thermodynamic behavior and optical properties (i.e. structure, composition, membrane integrity, orientation, thickness, and organization) at the aqueous/monolayer/air interface change with the inclusion of non-biological, nano-sized materials.

5.2 Future Directions

While these experiments represent new and important discoveries into developing a predictive understanding of black carbon – lung surfactant interactions and how non-biological, nano-sized materials impact membrane structure and function, there remain unresolved questions concerning the systems in this work that merit revision and additional attention. The three remaining questions inspired by this work fall into two general areas: other carbon particulates, a more accurate lung model, and reversibility.

5.2.1 Other Carbon Particulates

The work described in this thesis examined PHFs that were chosen to mimic black carbon aerosols that have oxidized in the atmosphere and have become soluble in water. An important consideration, however, is that when black carbon is initially generated, it has a high elemental carbon content and is insoluble in water [4]. For this reason, existing research in this field typically uses carbon nanopowders [12, 13]. Additionally, BC aerosols in ambient air can collide with other airborne particles to form larger, and even more heterogeneous particles with elemental carbon content under 50% [4]. To my knowledge, the interactions of PHFs with DPPC monolayers at aqueous – air interfaces have not previously been explored with anything other than carbon nanopowder (and now PHFs). To further our understanding of the effects of inhaling non-biological carbonaceous nanoparticles, studying "freshly generated" vs. "aged" black carbon, specifically PHFs vs. fullerenes or carbon nanopowder, would be significant. Given that black carbon is extremely heterogeneous in its chemical composition [4], it would also be pertinent to build up our current BC model to a more complex and accurate BC model (i.e. with trace organics, sulfate, nitrate, metals, etc.), ultimately working our way up to field samples.

5.2.2 More Accurate Lung Model

The work described in this thesis examined DPPC, which was chosen to be a model biological membrane, as it is the primary component of lung surfactant. As previously discussed, lung surfactant is a complex, heterogeneous chemical mixture that consists of lipids (~90%) and surfactant-associated proteins (~10%) [20]. Of the ~90% lipid component of lung surfactant, phosphatidylcholine (PC) lipids make up ~80%, about half of which is DPPC [20, 21]. The other 20% is comprised of lysophosphatidylcholine (LPC), sphingomyelin (SM), phosphatidylglycerol (PG), phosphatidylinositol (PI), phosphatidylserine (PS), phosphatidylethanolamine (PE), and a phospholipid (PL)/cholesterol (chol) mixture [20, 21]. Additionally, SP-A, SP-B, SP-C, and SP-D are common surfactant-associated proteins. Because inhalation of nanoparticles such as black carbon can lead to deficiency and dysfunction of lung surfactant, and can contribute to a variety of harmful respiratory disorders and illnesses [60], using more accurate models of lung surfactant (i.e. mixed monolayers with protein components) should be an important goal for future studies.

5.2.3 Reversibility

The work described in Chapters 3 and 4 discusses how a Langmuir trough is used to obtain compression isotherms. These Langmuir trough compression isotherms of PHFs with DPPC address how PHFs affect a DPPC monolayer's thermodynamic properties by showing disruption in ordering of the DPPC film with the addition of particulates. What Chapters 3 and 4 don't address is whether the PHF-DPPC interactions we are observing are irreversible.

To strengthen thermodynamic studies of DPPC (in Chapters 3 and 4), DPPC's response to quasi-static compression-expansion cycles of the surface area should be investigated [13, 189]. These quasi-static compression-expansion cycles of the surface area will allow us to evaluate possible hysteresis induced by various phenomena, including internal reorganization of the monolayer, formation of multilayers, or expulsion of lipid molecules to the subphase and respreading processes [13]. These compression-expansion cycle experiments are significant when studying pulmonary surfactant because they are related to physiological responses during the respiratory cycle [13, 190-194].

REFERENCES CITED

REFERENCES CITED

1. Wagner, S.; Jaffé, R.; Stubbins, A., Dissolved black carbon in aquatic ecosystems. *Limnology and Oceanography Letters* **2018,** *3* (3), 168-185.

2. NASA:EarthObservatory, Camp Fire Spreads Foul Air in California. **2018**.

3. Zhang, Y.; Li, M.; Cheng, Y.; Geng, G.; Hong, C.; Li, H.; Li, X.; Tong, D.; Wu, N.; Zhang, X.; Zheng, B.; Zheng, Y.; Bo, Y.; Su, H.; Zhang, Q., Modeling the aging process of black carbon during atmospheric transport using a new approach: a case study in Beijing. *Atmospheric Chemistry and Physics* **2019,** *19* (14), 9663-9680.

4. Long, C. M.; Nascarella, M. A.; Valberg, P. A., Carbon black vs. black carbon and other airborne materials containing elemental carbon: physical and chemical distinctions. *Environ Pollut* **2013,** *181*, 271-86.

5. EPA Basic Information What is Black Carbon? https://www3.epa.gov/airquality/blackcarbon/basic.html#where.

6. Wang, Y.; Ma, P. L.; Peng, J.; Zhang, R.; Jiang, J. H.; Easter, R. C.; Yung, Y. L., Constraining Aging Processes of Black Carbon in the Community Atmosphere Model Using Environmental Chamber Measurements. *J Adv Model Earth Syst* **2018,** *10* (10), 2514-2526.

7. Liu, C.; Xu, X.; Yin, Y.; Schnaiter, M.; Yung, Y. L., Black carbon aggregates: A database for optical properties. *Journal of Quantitative Spectroscopy and Radiative Transfer* **2019,** *222-223*, 170-179.

8. He, C.; Liou, K.-N.; Takano, Y.; Zhang, R.; Levy Zamora, M.; Yang, P.; Li, Q.; Leung, L. R., Variation of the radiative properties during black carbon aging: theoretical and experimental intercomparison. *Atmospheric Chemistry and Physics* **2015,** *15* (20), 11967-11980.

9. Kunzi, L.; Krapf, M.; Daher, N.; Dommen, J.; Jeannet, N.; Schneider, S.; Platt, S.; Slowik, J. G.; Baumlin, N.; Salathe, M.; Prevot, A. S.; Kalberer, M.; Strahl, C.; Dumbgen, L.; Sioutas, C.; Baltensperger, U.; Geiser, M., Toxicity of aged gasoline exhaust particles to normal and diseased airway epithelia. *Sci Rep* **2015,** *5*, 11801.

10. Lary, D. J.; Shallcross, D. E.; Toumi, R., Carbonaceous aerosols and their potential role in atmospheric chemistry. *Journal of Geophysical Research: Atmospheres* **1999,** *104* (D13), 15929-15940.

11. Janssen, N. A.; Hoek, G.; Simic-Lawson, M.; Fischer, P.; van Bree, L.; ten Brink, H.; Keuken, M.; Atkinson, R. W.; Anderson, H. R.; Brunekreef, B.; Cassee, F. R., Black carbon as an additional indicator of the adverse health effects of airborne particles compared with PM10 and PM2.5. *Environ Health Perspect* **2011,** *119* (12), 1691-9.

12. Sheridan, A. J.; Slater, J. M.; Arnold, T.; Campbell, R. A.; Thompson, K. C., Changes to DPPC Domain Structure in the Presence of Carbon Nanoparticles. *Langmuir* **2017,** *33* (39), 10374-10384.

13. Guzmán, E.; Santini, E.; Zabiegaj, D.; Ferrari, M.; Liggieri, L.; Ravera, F., Interaction of Carbon Black Particles and Dipalmitoylphosphatidylcholine at the Water/Air Interface: Thermodynamics and Rheology. *The Journal of Physical Chemistry C* **2015,** *119* (48), 26937-26947.

14. FederalAviationAdministration, Aviation Emissions, Impacts & Mitigation: A Primer. **2015**.

15. UnitedStatesEnvironmentalProtectionAgency, Black Carbon Research. **2017**.

16. Levy, L.; Chaudhuri, I. S.; Krueger, N.; McCunney, R. J., Does carbon black disaggregate in lung fluid? A critical assessment. *Chem Res Toxicol* **2012,** *25* (10), 2001-6.

17. Guzmán, E.; Liggieri, L.; Santini, E.; Ferrari, M.; Ravera, F., Effect of Hydrophilic and Hydrophobic Nanoparticles on the Surface Pressure Response of DPPC Monolayers. *The Journal of Physical Chemistry C* **2011,** *115* (44), 21715-21722.

18. Jansen, K. L.; Larson, T. V.; Koenig, J. Q.; Mar, T. F.; Fields, C.; Stewart, J.; Lippmann, M., Associations between Health Effects and Particulate Matter and Black Carbon in Subjects with Respiratory Disease. *Environmental Health Perspectives* **2005,** *113* (12), 1741-1746.

19. Highwood, E. J.; Kinnersley, R. P., When smoke gets in our eyes: the multiple impacts of atmospheric black carbon on climate, air quality and health. *Environ Int* **2006,** *32* (4), 560-6.

20. Ruud Veldhuizen, K. N., Sandra Orgeig, Fred Possmayer, The role of lipids in pulmonary surfactant. *Molecular Basis of Disease* **1998,** *1408* (2-3), 90-108.

21. Haagsman, H. P.; Diemel, R. V., Surfactant-associated proteins: functions and structural variation. *Comp Biochem Physiol A Mol Integr Physiol.* **2001,** *129* (1), 91-108.

22. Jackson, J. C., Chapter 46 - Respiratory Distress in the Preterm Infant. *Avery's Diseases of the Newborn* **2012,** *9*, 633-646.

23. Arifa, R. D. N.; de Paula, T. P.; Lima, R. L.; Brito, C. B.; Andrade, M. E. R.; Cardoso, V. N.; Pinheiro, M. V. B.; Ladeira, L. O.; Krambrock, K.; Teixeira, M. M.; Fagundes, C. T.; Souza, D. G., Anti-inflammatory and antioxidant effects of the nanocomposite Fullerol decrease the severity of intestinal inflammation induced by gut ischemia and reperfusion. *European Journal of Pharmacology* **2021,** *898*.

24. Awan, F.; Bulger, E.; Berry, R. M.; Tam, K. C., Enhanced radical scavenging activity of polyhydroxylated C-60 functionalized cellulose nanocrystals. *Cellulose* **2016,** *23* (6), 3589-3599.

25. Ding, M.; Li, M.; Zhang, E. M.; Yang, H. L., FULLEROL alleviates myocardial ischemia-reperfusion injury by reducing inflammation and oxidative stress in cardiomyocytes via activating the Nrf2/HO-1 signaling pathway. *European Review for Medical and Pharmacological Sciences* **2020,** *24* (18), 9665-9674.

26. Kovac, T.; Marcek, T.; Sarkanj, B.; Borisev, I.; Izakovic, M.; Jukic, K.; Loncaric, A.; Krska, T.; Sulyok, M.; Krska, R., Fullerol C-60(OH)(24) Nanoparticles and Drought Impact on Wheat (Triticum aestivum L.) during Growth and Infection with Aspergillus flavus. *Journal of Fungi* **2021,** *7* (3).

27. Ouyang, H. X.; Liang, A. H.; Jiang, Z. L., Fullerol Nanocatalysis and Trimodal Surface Plasmon Resonance for the Determination of Isocarbophos. *Frontiers in Chemistry* **2020,** *8*.

28. Shafiq, F.; Iqbal, M.; Ashraf, M. A.; Ali, M., Foliar applied fullerol differentially improves salt tolerance in wheat through ion compartmentalization, osmotic adjustments and regulation of enzymatic antioxidants. *Physiology and Molecular Biology of Plants* **2020,** *26* (3), 475-487.

29. Yu, H. X.; Dong, L.; Wu, C. Y.; Wu, L.; Xing, J., Hydroxyfullerene as a novel coating for solid-phase microextraction fiber with sol-gel technology. *Journal of Chromatography A* **2002,** *978* (1-2), 37-48.

30. Ma, J. H.; Guo, R. R.; Tan, X. N., Aqueous photochemistry of fullerol revisited: Energy transfer vs. electron transfer processes probed by Rhodamine B degradation. *Journal of Photochemistry and Photobiology a-Chemistry* **2020,** *397*.

31. Pickering, K. D.; Wiesner, M. R., Fullerol-sensitized production of reactive oxygen species in aqueous solution. *Environmental Science & Technology* **2005,** *39* (5), 1359-1365.

32. Roberts, J. E.; Wielgus, A. R.; Boyes, W. K.; Andley, U.; Chignell, C. F., Phototoxicity and cytotoxicity of fullerol in human lens epithelial cells. *Toxicology and Applied Pharmacology* **2008,** *228* (1), 49-58.

33. Yuan, Y.; Guo, P. P.; Peng, X. J., Effect of fullerol nanoparticles on the transport and release of copper ions in saturated porous media. *Environmental Science and Pollution Research* **2019,** *26* (15), 15255-15261.

34. Zhao, L. J.; Zhang, H. L.; Wang, J. J.; Tian, L. Y.; Li, F. F.; Liu, S. J.; Peralta-Videa, J. R.; Gardea-Torresdey, J. L.; White, J. C.; Huang, Y. X.; Keller, A.; Ji, R., C60 Fullerols Enhance Copper Toxicity and Alter the Leaf Metabolite and Protein Profile in Cucumber. *Environmental Science & Technology* **2019,** *53* (4), 2171-2180.

35. Kokubo, K.; Matsubayashi, K.; Tategaki, H.; Takada, H.; Oshima, T., Facile synthesis of highly water-soluble fullerenes more than half-covered by hydroxyl groups. *Acs Nano* **2008,** *2* (2), 327-333.

36. Semenov, K. N.; Charykov, N. A.; Keskinov, V. N., Fullerenol Synthesis and Identification. Properties of the Fullerenol Water Solutions. *Journal of Chemical and Engineering Data* **2011,** *56* (2), 230-239.

37. Letenko, D. G.; Charykov, N. A.; Nikitin, V. A.; Semenov, K. N.; Matuzenko, M. Y.; Keskinov, V. A.; Gruzinskaya, E. G.; Tsvetkova, L. V., Study of aqueous solutions of fullerenol-d by the dynamic light scattering method. *Russian Journal of Applied Chemistry* **2011,** *84* (1), 50-53.

38. Dawid, A.; Gorny, K.; Gburski, Z., Water Solvent Effect on Infrared and Raman Spectra of C-60(OH)(24) Fullerenol Isomers: DFT Study. *Journal of Physical Chemistry C* **2017,** *121* (4), 2303-2315.

39. Indeglia, P. A.; Georgieva, A.; Krishna, V. B.; Bonzongo, J. C. J., Physicochemical characterization of fullerenol and fullerenol synthesis by-products prepared in alkaline media. *Journal of Nanoparticle Research* **2014,** *16* (9).

40. Piatek, A.; Dawid, A.; Gburski, Z., The properties of small fullerenol cluster (C-60(OH)(24))(7): Computer simulation. *Spectrochimica Acta Part a-Molecular and Biomolecular Spectroscopy* **2011,** *79* (4), 819-823.

41. Rodriguez-Zavala, J. G.; Guirado-Lopez, R. A., Structure and energetics of polyhydroxylated carbon fullerenes. *Physical Review B* **2004,** *69* (7).

42. Vachugova, E.; Savchenko, E.; Nepomnyashchaya, E. In *Investigation of the fullerenol solution parameters by combined technique based on light scattering*, 6th International Conference on Information Technology and Nanotechnology (IEEE ITNT), Samara, RUSSIA, May 26-29; Samara, RUSSIA, 2020.

43. Vranes, M.; Borisev, I.; Tot, A.; Armakovic, S.; Armakovic, S.; Jovic, D.; Gadzuric, S.; Djordjevic, A., Self-assembling, reactivity and molecular dynamics of fullerenol nanoparticles. *Physical Chemistry Chemical Physics* **2017,** *19* (1), 135-144.

44. Chaban, V. V.; Fileti, E. E., Which fullerenols are water soluble? Systematic atomistic investigation. *New Journal of Chemistry* **2017,** *41* (1), 184-189.

45. Fileti, E. E.; Rivelino, R.; Mota, F. D.; Malaspina, T., Effects of hydroxyl group distribution on the reactivity, stability and optical properties of fullerenols. *Nanotechnology* **2008,** *19* (36).

46. Keshri, S.; Tembe, B. L., Thermodynamics of association of water soluble fullerene derivatives , n=0, 2, 4, 8 and 12 in aqueous media. *Journal of Chemical Sciences* **2017,** *129* (9), 1327-1340.

47. Keshri, S.; Tembe, B. L., Thermodynamics of hydration of fullerols C-60(OH)(n) and hydrogen bond dynamics in their hydration shells. *Journal of Chemical Physics* **2017,** *146* (7).

48. Maciel, C.; Fileti, E. E.; Rivelino, R., Assessing the solvation mechanism of C-60(OH)(24) in aqueous solution. *Chemical Physics Letters* **2011,** *507* (4-6), 244-247.

49. Sharoyko, V. V.; Ageev, S. V.; Meshcheriakov, A. A.; Akentiev, A. V.; Noskov, B. A.; Rakipov, I. T.; Charykov, N. A.; Kulenova, N. A.; Shaimardanova, B. K.; Podolsky, N. E.; Semenov, K. N., Physicochemical study of water-soluble C-60(OH)(24) fullerenol. *Journal of Molecular Liquids* **2020,** *311.*

50. Lum, K.; Chandler, D.; Weeks, J. D., Hydrophobicity at small and large length scales. *Journal of Physical Chemistry B* **1999,** *103* (22), 4570-4577.

51. Liu, W. J.; Jeng, U.; Lin, T. L.; Lai, S. H.; Shih, M. C.; Tsao, C. S.; Wang, L. Y.; Chiang, L. Y.; Sung, L. P., Adsorption of dodecahydroxylated-fullerene monolayers at the air-water interface. *Physica B* **2000,** *283* (1-3), 49-52.

52. Akentiev, A. V.; Gorniaia, S. B.; Isakov, N. A.; Lebedev, V. T.; Milyaeva, O. Y.; Sedov, V. P.; Semenov, K. N.; Timoshen, K. A.; Noskov, B. A., Surface properties of fullerenol C-60(OH)(20) solutions. *Journal of Molecular Liquids* **2020,** *306.*

53. Shen, Y. R.; Ostroverkhov, V., Sun-Frequency Vibrational Spectroscopy on Water Interfaces: Polar Orientation of Water Molecules at Interfaces. *Chem. Rev.* **2006,** *106*, 1140-1154.

54. Ball, P., How to keep dry in water. *Nature* **2003,** *423*, 25-26.

55. Israelachvili, J.; Wennerstrom, H., Role of hydration and water structure in biological and colloidal interactions. *Nature* **1996,** *379*, 219-225.

56. Franks, F., *Water: A Comprehensive Treatise*. 1979; Vol. Vol. 1-6.

57. Gobrogge, E. A.; Woods, B. L.; Walker, R. A., Liquid organization and solvation properties at polar solid/liquid interfaces. *Faraday Discuss* **2013,** *167*, 309-27.

58. Roy, D.; Liu, S.; Woods, B. L.; Siler, A. R.; Fourkas, J. T.; Weeks, J. D.; Walker, R. A., Nonpolar Adsorption at the Silica/Methanol Interface: Surface Mediated Polarity and Solvent Density across a Strongly Associating Solid/Liquid Boundary. *The Journal of Physical Chemistry C* **2013,** *117* (51), 27052-27061.

59. Woods, B. L.; Walker, R. A., pH effects on molecular adsorption and solvation of p-nitrophenol at silica/aqueous interfaces. *J Phys Chem A* **2013,** *117* (29), 6224-33.

60. Ma, G.; Allen, H. C., DPPC Langmuir Monolayer at the Air-Water Interface: Probing the Tail and Head Groups by Vibrational Sum Frequency Generation Spectroscopy. *Langmuir* **2006,** *22*, 5341-5349.

61. Woods, B. L.; George, J. K.; Sherman, A. M.; Callis, P. R.; Walker, R. A., Adsorption and Aggregation at Silica/Methanol Interfaces: The Role of Solute Structure. *The Journal of Physical Chemistry C* **2015,** *119* (25), 14230-14238.

62. Link, K. A.; Spurzem, G. N.; Tuladhar, A.; Chase, Z.; Wang, Z.; Wang, H.; Walker, R. A., Cooperative Adsorption of Trehalose to DPPC Monolayers at the Water-Air Interface Studied with Vibrational Sum Frequency Generation. *J Phys Chem B* **2019,** *123* (42), 8931-8938.

63. Link, K. A.; Spurzem, G. N.; Tuladhar, A.; Chase, Z.; Wang, Z.; Wang, H.; Walker, R. A., Organic Enrichment at Aqueous Interfaces: Cooperative Adsorption of Glucuronic Acid to DPPC Monolayers Studied with Vibrational Sum Frequency Generation. *J Phys Chem A* **2019,** *123* (26), 5621-5632.

64. Link, K. A.; Hsieh, C.; Tuladhar, A.; Chase, Z.; Wang, Z.; Wang, H.; Walker, R. A., Vibrational studies of saccharide-induced lipid film reorganization at aqueous/air interfaces. *Chemical Physics* **2018,** *512*, 104-110.

65. Shaikh, N.; Andriolo, J. M.; Skinner, J. L.; Walker, R. A., Carbon Nanoparticle-Induced Changes to Lipid Monolayer Structure at Air-Water Interfaces. 2. Ionic Strength Effects. *J. Phys. Chem. B. (prepared for submission)* **2022**.

66. Shaikh, N.; Andriolo, J. M.; Skinner, J. L.; Walker, R. A., Carbon Nanoparticle-Induced Organizational Changes in Lipid Monolayers at Water – Air Interfaces. *J. Phys. Chem. B. (submitted and in review)* **2022**.

67. Shaikh, N.; Bernhard, S. P.; Walker, R. A., Surface Activity and Aggregation Behavior of Polyhydroxylated Fullerenes in Aqueous Solutions. *Langmuir (submitted and in review)* **2022**.

68. Scholl, F. A.; Morais, P. V.; Gabriel, R. C.; Schöning, M. J.; Siqueira, J. J. R.; Caseli, L., Carbon Nanotubes Arranged As Smart Interfaces in Lipid Langmuir− Blodgett Films Enhancing the Enzymatic Properties of Penicillinase for Biosensing Applications. *Appl. Mater. Interfaces* **2017,** *9*, 31054-31066.

69. Schach, D.; Globisch, C.; Roeters, S. J.; Woutersen, S.; Fuchs, A.; Wieiss, C. K.; Backus, E. H. G.; Landfester, K.; Bonn, M.; Peter, C.; Weidner, T., Sticky water surfaces: Helix–coil transitions suppressed in a cell-penetrating peptide at the air-water interface. *The Journal of Chemical Physics* **2014,** *141* (22).

70. Azam, M. S.; Gibbs-Davis, J. M., Monitoring DNA Hybridization and Thermal Dissociation at the Silica/Water Interface Using Resonantly Enhanced Second Harmonic Generation Spectroscopy. *Anal. Chem.* **2013,** *85* (17), 8031-8038.

71. Li, W.; Liiu, D.; Wu, J.; Kim, C.; Fortner, J. D., Aqueous Aggregation and Surface Deposition Processes of Engineered Superparamagnetic Iron Oxide Nanoparticles for Environmental Applications. *Environ. Sci. Technol.* **2014,** *48* (20), 11892-11900.

72. Wu, G.; Zhu, X.; Ji, H.; Chen, D., Molecular modeling of interactions between heavy crude oil and the soil organic matter coated quartz surface. *Chemosphere* **2015,** *119*, 242-249.

73. Franco, C. A.; Martínez, M.; Benjumea, P.; Patiño, E.; Cortés, F. B., Water Remediation Based on Oil Adsorption Using Nanosilicates Functionalized with a Petroleum Vacuum Residue. *Adsorpt. Sci. Technol.* **2014,** *32*, 197-207.

74. Lin, M.-C.; Lin, K.-C., Interaction between crystal violet and anionic surfactants at silica/water interface using evanescent wave-cavity ring-down absorption spectroscopy. *J Colloid Interface Sci* **2012,** *379*, 41-47.

75. Burrows, S. M.; Ogunro, O.; Frossard, A. A.; Russell, L. M.; Rasch, P. J.; Elliott, S. M., A physically based framework for modeling the organic fractionation of sea spray aerosol from bubble film Langmuir equilibria. *Atmospheric Chemistry and Physics* **2014,** *14* (24), 13601-13629.

76. Pan, X. C.; Yang, F. Y.; Chen, S. L.; Zhu, X. F.; Wang, C. Y., Cooperative Effects of Zwitterionic-Ionic Surfactant Mixtures on the Interfacial Water Structure Revealed by Sum Frequency Generation Vibrational Spectroscopy. *Langmuir* **2018,** *34* (18), 5273-5278.

77. Cao, D. P.; Wu, J. Z., Theoretical study of cooperativity in multivalent polymers for colloidal stabilization. *Langmuir* **2005,** *21* (21), 9786-9791.

78. Vakarin, E.; Duda, Y.; Holovko, M., Cooperative adsorption of network forming fluids onto crystalline surfaces: Structure and connectivity of the interface. *Journal of Chemical Physics* **1997,** *107* (14), 5569-5581.

79. Nguyen, K. T.; Nguyen, T. D.; Nguyen, A. V., Strong Cooperative Effect of Oppositely Charged Surfactant Mixtures on Their Adsorption and Packing at the Air-Water Interface and Interfacial Water Structure. *Langmuir* **2014,** *30* (24), 7047-7051.

80. Cordon, M. J.; Harris, J. W.; Vega-Vila, J. C.; Bates, J. S.; Kaur, S.; Gupta, M.; Witzke, M. E.; Wegener, E. C.; Miller, J. T.; Flaherty, D. W.; Hibbitts, D. D.; Gounder, R., Dominant Role of Entropy in Stabilizing Sugar Isomerization Transition States within Hydrophobic Zeolite Pores. *Journal of the American Chemical Society* **2018,** *140* (43), 14244-14266.

81. Jimenez-Cruz, F.; Hernandez, J. A.; Laredo, G. C.; Mares-Gallardo, M. T.; Garcia-Gutierrez, J. L., Adsorption of n-heptane and 2-methylheptane in the gas phase on polyvinylidene chloride-based microporous activated carbon. *Energy & Fuels* **2007,** *21* (5), 2929-2934.

82. Kiraly, Z.; Borner, R. H. K.; Findenegg, G. H., Adsorption and aggregation of C8E4 and C(8)G(1) nonionic surfactants on hydrophilic silica studied by calorimetry. *Langmuir* **1997,** *13* (13), 3308-3315.

83. Hinderliter, A.; May, S., Cooperative adsorption of proteins onto lipid membranes. *Journal of Physics-Condensed Matter* **2006,** *18* (28), S1257-S1270.

84. Schwarz, G., A universal thermodynamic approach to analyze biomolecular binding experiments. *Biophysical Chemistry* **2000,** *86* (2-3), 119-129.

85. Yaminsky, V. V.; Ninham, B. W.; Christenson, H. K.; Pashley, R. M., Adsorption forces between hydrophobic monolayers. *Langmuir* **1996,** *12* (8), 1936-1943.

86. Penfold, J.; Thomas, R. K., Counterion Condensation, the Gibbs Equation, and Surfactant Binding: An Integrated Description of the Behavior of Polyelectrolytes and Their Mixtures with Surfactants at the Air-Water Interface. *Journal of Physical Chemistry B* **2020,** *124* (28), 6074-6094.

87. Rajagopal, R.; Hong, M. K.; Ziegler, L. D.; Erramilli, S.; Narayan, O., Conjugate Acid-Base Interaction Driven Phase Transition at a 2D Air-Water Interface. *Journal of Physical Chemistry B* **2021,** *125* (23), 6330-6337.

88. Sarkar, B.; Mukhopadhyay, R.; Ramanayaka, S.; Bolan, N.; Ok, Y. S., The role of soils in the disposition, sequestration and decontamination of environmental contaminants. *Philosophical Transactions of the Royal Society B-Biological Sciences* **2021,** *376* (1834).

89. Schill, S. R.; Burrows, S. M.; Hasenecz, E. S.; Stone, E. A.; Bertram, T. H., The Impact of Divalent Cations on the Enrichment of Soluble Saccharides in Primary Sea Spray Aerosol. *Atmosphere* **2018,** *9* (12).

90. Otten, D. E.; Shaffer, P. R.; Geissler, P. L.; Saykally, R. J., Elucidating the mechanism of selective ion adsorption to the liquid water surface. *Proceedings of the National Academy of Sciences of the United States of America* **2012,** *109* (3), 701-705.

91. Zhang, H.; Fan, Q.; Wang, Y. E.; Neal, C. R.; Zuo, Y. Y., Comparative study of clinical pulmonary surfactants using atomic force microscopy. *Biochim Biophys Acta* **2011,** *1808* (7), 1832-42.

92. Ma, G.; Allen, H. C., New Insights into Lung Surfactant Monolayers Using Vibrational Sum Frequency Generation Spectroscopy. **2006**.

93. Nag, K.; Perez-Gil, J.; Ruano, M. L. F.; Worthman, L. A. D.; Stewart, J.; Casals, C.; Keough, K. M. W., Phase Transitions in Films of Lung Surfactant at the Air-Water Interface. *Biophysical Journal* **1998,** *74*, 2983-2995.

94. Plant, A. L., Supported hybrid bilayer membranes as rugged cell membrane mimics. *Langmuir* **1999,** *15*, 5128-5135.

95. Sackmann, E., Supported membranes: scientific and practical applications. *Science* **1996,** *271*, 43-48.

96. Ciumac, D.; Campbell, R. A.; Xu, H.; Clifton, L. A.; Hughes, A. V.; Webster, J. R. P.; Lu, J. R., Implications of lipid monolayer charge characteristics on their selective interactions with a short antimicrobial peptide. *Colloids Surf. B-Biointerfaces* **2017,** *150*, 308-316.

97. Joondan, N.; Jhaumeer-Laulloo, S.; Caumul, P., Effect of Chain Length on the Micellization, Antibacterial, DPPC Interaction and Antioxidant Activities of L-3,4-Dihydroxyphenylalanine (L-DOPA) Esters. *J. Surfactants Deterg,* **2015,** *18*, 1095-1104.

98. Mendez, M. A.; Nazemi, Z.; Uyanik, I.; Lu, Y.; H., G. H., Melittin adsorption and lipid monolayer disruption at liquid-liquid interfaces. *Langmuir* **2011,** *27*, 13918-13924.

99. Salay, L. C.; Ferreira, M.; Oliveira, O. N.; Nakaie, C. R.; Schreier, S., Headgroup specificity for the interaction of the antimicrobial peptide tritrpticin with phospholipid Langmuir monolayers. *Colloids Surf. B-Biointerfaces* **2012,** *100*, 95-102.

100. Guzmán, E.; Santini, E.; Ferrari, M.; Liggieri, L.; Ravera, F., Interfacial Properties of Mixed DPPC–Hydrophobic Fumed Silica Nanoparticle Layers. *The Journal of Physical Chemistry C* **2015,** *119* (36), 21024-21034.

101. Shaikh, N.; Walker, R. A., Cooperative Adsorption at Liquid Interfaces. *Langmuir (in preparation for submission)* **2022**.

102. Danov, K. D.; Kralchevsky, P. A., The Standard Free Energy of Surfactant Adsorption at Air/Water and Oil/Water Interfaces: Theoretical vs. Empirical Approaches. *Colloid Journal* **2012,** *74* (2), 172-185.

103. Wustneck, R.; Perez-Gil, J.; Wustneck, N.; Cruz, A.; Fainerman, V. B.; Pison, U., Interfacial properties of pulmonary surfactant layers. *Adv Colloid Interface Sci* **2005,** *117* (1-3), 33-58.

104. Giner-Casares, J. J.; Brezesinski, G.; Möhwald, H., Langmuir monolayers as unique physical models. *Current Opinion in Colloid & Interface Science* **2014,** *19* (3), 176-182.

105. Möhwald, H., Phospholipid and phospholipid-protein monolayers at the air/water interface. *Annu. Rev. Phys. Chem.* **1990,** *41*, 441-476.

106. Kaganer, V. M.; Möhwald, H.; Dutta, P., Structure and phase transitions in Langmuir monolayers. *Reviews of Modern Physics* **1999,** *71*, 779-819.

107. Vollhardt, D.; Nandi, N.; Banik, S. D., Nanoaggregate shapes at the air/water interface. *Phys Chem Chem Phys* **2011,** *13* (11), 4812-29.

108. Duncan, S. L.; Larson, R. G., Comparing experimental and simulated pressure-area isotherms for DPPC. *Biophys J* **2008,** *94* (8), 2965-86.

109. J.A. Zasadzinski, J. D., H.E. Warriner, F. Bringezu, Alan J. Waring, The physics and physiology of lung surfactants. *Colloid & Interface Science* **2001,** *6*, 506-513.

110. Siebert, T. A.; Rugonyi, S., Influence of liquid-layer thickness on pulmonary surfactant spreading and collapse. *Biophys J* **2008,** *95* (10), 4549-59.

111. Sudheesh, S.; Ahmad, J.; Singh, G. S., Hysteresis of Isotherms of Mixed Monolayers of N-Octadecyl-N′-phenylthiourea and Stearic Acid at Air/Water Interface. *ISRN Physical Chemistry* **2012,** *2012*, 1-6.

112. Franken, P. A.; Weinreich, G.; Peters, C. W.; Hill, A. E., Generation of Optical Harmonics. *Phys Rev Lett* **1961,** *7* (4), 118-119.

113. Moad, A. J.; Simpson, G. J., A unified treatment of selection rules and symmetry relations for sum-frequency and second harmonic spectroscopies. *J Phys Chem B* **2004,** *118* (11), 3548-3562.

114. Lambert, A. G.; Davies, P. B.; Neivandt, D. J., Implementing the Theory of Sum Frequency Generation Vibrational Spectroscopy: A Tutorial Review. *Applied Spectroscopy Reviews* **2005,** *40* (2), 103-145.

115. Rangwalla, H.; Dhinojwala, A., Probing Hidden Polymeric Interfaces Usingir–Visible Sum-Frequency Generation Spectroscopy. *The Journal of Adhesion* **2010,** *80* (1-2), 37-59.

116. Shen, Y. R., Surface Properties probed by second-harmonic and sum-frequency generation. *Nature* **1989,** *337*, 519-525.

117. Richmond, G. L., Molecular Bonding and Interactions at Aqueous Surfaces as Probed by Vibrational Sum Frequency Spectroscopy. *Chem. Rev.* **2002,** *102*, 2693-2724.

118. Link, K. A.; Hsieh, C.-Y.; Tuladhar, A.; Chase, Z.; Wang, Z.; Wang, H.; Walker, R. A., Vibrational studies of saccharide-induced lipid film reorganization at aqueous/air interfaces. *Chemical Physics* **2018,** *512*, 104-110.

119. Noskov, B. A.; Timoshen, K. A.; Akentiev, A. V.; Chirkov, N. S.; Dubovsky, I. M.; Lebedev, V. T.; Lin, S. Y.; Loglio, G.; Miller, R.; Sedov, V. P.; Borisenkova, A. A., Dynamic Surface Properties of Fullerenol Solutions. *Langmuir* **2019,** *35* (10), 3773-3779.

120. Liu, W.-J.; Jeng, U.; Lin, T.-L.; Lai, S.-H.; Shih, M. C.; Tsao, C.-S.; Wang, L. Y.; Chiang, L. Y.; Sung, L. P., Adsorption of dodecahydroxylated-fullerene monolayers at the air-water interface. *Physica B: Condensed Matter* **2000,** *283* (1-3), 49-52.

121. Akentiev, A. V.; Gorniaia, S. B.; Isakov, N. A.; Lebedev, V. T.; Milyaeva, O.; Sedov, V. P.; Semenov, K. N.; Timoshen, K. A.; Noskov, B. A., Surface properties of fullerenol C60(OH)20 solutions. *Journal of Molecular Liquids* **2020,** *306*.

122. Wielgus, A. R.; Zhao, B.; Chignell, C. F.; Hu, D. N.; Roberts, J. E., Phototoxicity and cytotoxicity of fullerol in human retinal pigment epithelial cells. *Toxicol Appl Pharmacol* **2010,** *242* (1), 79-90.

123. Garcia-Caurel, E.; De Martino, A.; Gaston, J.-P.; Yan, L., Application of Spectroscopic Ellipsometry and Mueller Ellipsometry to Optical Characterization. *Applied Spectroscopy* **2013,** *67* (1), 1-21.

124. Losurdo, M.; Hingerl, K., *Ellipsometry at the Nanoscale* 2013.

125. J.A.Woollam What is Ellipsometry? https://www.jawoollam.com/resources/ellipsometry-tutorial/what-is-ellipsometry (accessed March 01, 2019).

126. Andreoni, A.; Nardo, L.; Bondani, M.; Zhao, B. Z.; Roberts, J. E., Time-Resolved Fluorescence Studies of Fullerene Derivatives. *Journal of Physical Chemistry B* **2013,** *117* (24), 7203-7209.

127. Brant, J. A.; Labille, J.; Robichaud, C. O.; Wiesner, M. R., Fullerol cluster formation in aqueous solutions: Implications for environmental release. *Journal of Colloid and Interface Science* **2007,** *314* (1), 281-288.

128. Pradhan, S.; Xu, L. P.; Chen, S. W., Janus nanoparticles by interfacial engineering. *Advanced Functional Materials* **2007,** *17* (14), 2385-2392.

129. Tsyrenoya, A.; Miller, K.; Yan, J.; Olson, E.; Anthony, S. M.; Jiang, S., Surfactant-Mediated Assembly of Amphiphilic Janus Spheres. *Langmuir* **2019,** *35* (18), 6106-6111.

130. Metcalf, A. R.; Loza, C. L.; Coggon, M. M.; Craven, J. S.; Jonsson, H. H.; Flagan, R. C.; Seinfeld, J. H., Secondary Organic Aerosol Coating Formation and Evaporation: Chamber Studies Using Black Carbon Seed Aerosol and the Single-Particle Soot Photometer. *Aerosol Science and Technology* **2013,** *47* (3), 326-347.

131. Moteki, N.; Kondo, Y., Dependence of Laser-Induced Incandescence on Physical Properties of Black Carbon Aerosols: Measurements and Theoretical Interpretation. *Aerosol Science and Technology* **2010,** *44* (8), 663-675.

132. Schmitt, C. G.; All, J. D.; Schwarz, J. P.; Arnott, W. P.; Cole, R. J.; Lapham, E.; Celestian, A., Measurements of light-absorbing particles on the glaciers in the Cordillera Blanca, Peru. *Cryosphere* **2015,** *9* (1), 331-340.

133. Nandy, L.; Yao, Y.; Zheng, Z. H.; Riemer, N., Water uptake and optical properties of mixed organic-inorganic particles. *Aerosol Science and Technology* **2021**.

134. Rastogi, N.; Satish, R.; Singh, A.; Kumar, V.; Thamban, N.; Lalchandani, V.; Shukla, A.; Vats, P.; Tripathi, S. N.; Ganguly, D.; Slowik, J.; Prevot, A. S. H., Diurnal

variability in the spectral characteristics and sources of water-soluble brown carbon aerosols over Delhi. *Science of the Total Environment* **2021,** *794*.

135. Textor, C.; Schulz, M.; Guibert, S.; Kinne, S.; Balkanski, Y.; Bauer, S.; Berntsen, T.; Berglen, T.; Boucher, O.; Chin, M.; Dentener, F.; Diehl, T.; Easter, R.; Feichter, H.; Fillmore, D.; Ghan, S.; Ginoux, P.; Gong, S.; Kristjansson, J. E.; Krol, M.; Lauer, A.; Lamarque, J. F.; Liu, X.; Montanaro, V.; Myhre, G.; Penner, J.; Pitari, G.; Reddy, S.; Seland, O.; Stier, P.; Takemura, T.; Tie, X., Analysis and quantification of the diversities of aerosol life cycles within AeroCom. *Atmospheric Chemistry and Physics* **2006,** *6*, 1777-1813.

136. Clifford, M. H.; Potocki, M.; Koch, I.; Sherpa, T.; Handley, M.; Korotkikh, E.; Introne, D.; Kaspari, S.; Miner, K.; Matthews, T.; Perry, B.; Guy, H.; Gajurel, A.; Singh, P. K.; Elvin, S.; Elmore, C. A.; Tait, A.; Mayewski, A. P., A case study using 2019 pre-monsoon snow and stream chemistry in the Khumbu region, Nepal. *Science of the Total Environment* **2021,** *789*.

137. Lohmann, U.; Feichter, J., Global indirect aerosol effects: a review. *Atmospheric Chemistry and Physics* **2005,** *5*, 715-737.

138. Zhang, H. Y.; Wu, L.; Qian, W.; Ni, J. Z.; Wei, R.; Qi, Z. C.; Chen, W. F., Spectral characteristics of dissolved organic carbon derived from biomass-pyrogenic smoke (SDOC) in the aqueous environment and its solubilization effect on hydrophobic organic pollutants. *Water Research* **2021,** *203*.

139. Can, S. Z.; Mago, D. D.; Walker, R. A., Structure and Organization of Hexadecanol Isomers Adsorbed to the Air/Water Interface. *Langmuir* **2006,** *22* (19), 8043-8049.

140. Rosen, M. J., *Surfactants and Interfacial Phenomena*. Third ed.; John Wiley & Sons, Inc.: Hoboken, New Jersey, 2004.

141. Purnell, G. E.; Walker, R. A., Surface solvation and hindered isomerization at the water/silica interface explored with second harmonic generation. *J Chem Phys* **2019,** *150* (19), 194701.

142. Purnell, G. E.; McNally, M. T.; Walker, R. A., Buried liquid interfaces as a form of chemistry in confinement: the case of 4-dimethylaminobenzonitrile at the silica-liquid interface. *Journal of the American Chemical Society* **2020,** *142* (5), 2375-2385.

143. Andreoni, A.; Nardo, L.; Bondani, M.; Zhao, B.; Roberts, J. E., Time-resolved fluorescence studies of fullerene derivatives. *J Phys Chem B* **2013,** *117* (24), 7203-9.

144. Laus, S.; Sitharaman, B.; Tóth, É.; Bolskar, R. D.; Helm, L.; Asokan, S.; Wong, M. S.; Wilson, L. J.; Merbach, A. E., Destroying Gadofullerene Aggregates by Salt Addition in Aqueous Solution of Gd@C60(OH)x and Gd@C60[C(COOH2)]10. *J. AM. CHEM. SOC.* **2005,** *127* (26), 9368-9369.

145. Li, X.-J.; Y, X.-H.; S, L.-M.; R, H.-J.; T, T.-Z., A DFT study on structure, stability, and optical property of fullerenols. *Structural Chemistry* **2013,** *24*, 1185-1192.

146. Liu, Y.; Zhang, G.; Niu, L.; Gan, L.; Liang, D., Assembly of Janus fullerenol: a novel approach to prepare rich carbon structures. *Journal of Materials Chemistry* **2011,** *21*, 14864-14868.

147. Xiong, F.; Li, J.; Wang, H.; Xing, G.; He, R., Evaluation of a Series of Different Surface Charged Fullerenol Nanoparticles as Reactive Oxygen Species Scavengers and Potential Cytoprotective Agents. *Journal of Nanoscience and Nanotechnology* **2016,** *17* (7), 7170-7174(5).

148. Wang, F. F.; Li, N.; Tian, D.; Xia, G. F.; Xiao, N., Efficient Synthesis of Fullerenol in Anion Form for the Preparation of Electrodeposited Films. *ACS Nano* **2010,** *4* (10), 5565-5572.

149. Moad, A. J.; Simpson, G. J., A unified treatment of selection relations for sum-frequency and second harmonic spectroscopies. *Journal of Physical Chemistry B* **2004,** *108* (11), 3548-3562.

150. Hara, T.; Nomura, Y.; Narita, S.; Ito, H.; Shibuya, T., Electric-dipole forbidden transitions in C60: oscillator strengths induced by the spin–orbit coupling. *Journal of Molecular Structure: THEOCHEM* **2002,** *589-590*, 139-145.

151. Harrod, K. S.; Jaramillo, R. J.; Rosenberger, C. L.; Wang, S., Increased susceptibility to RSV infection by exposure to inhaled diesel engine emissions. *American Journal of Respiratory Cell and Molecular Biology* **2003,** *28* (4), 451-463.

152. Borm, P. J.; Cakmak, G.; Jermann, E.; Weishaupt, C.; Kempers, P.; van Schooten, F. J.; Oberdorster, G.; Schins, R. P., Formation of PAH-DNA adducts after in

vivo and vitro exposure of rats and lung cells to different commercial carbon blacks. *Toxicol Appl Pharmacol* **2005,** *205* (2), 157-167.

153. Wang, T.; Xu, H.; Zhu, Y.; Sun, X.; Chen, J.; Liu, B.; Zhao, Q.; Zhang, Y.; Liu, L.; Fang, J.; Xie, Y.; Liu, S.; Wu, R.; Song, X.; He, B.; Huang, W., Traffic-related air pollution associated pulmonary pathophysiologic changes and cardiac injury in elderly patients with COPD. *J Hazard Mater* **2022,** *424* (Pt B), 127463.

154. Kendall, M.; Brown, L.; Trought, K., Molecular adsorption at particle surfaces: a PM toxicity mediation mechanism. *Inhal Toxicol* **2004,** *16 Suppl 1*, 99-105.

155. Arick, D. Q.; Choi, Y. H.; Kim, H. C.; Won, Y. Y., Effects of nanoparticles on the mechanical functioning of the lung. *Adv Colloid Interface Sci* **2015,** *225*, 218-28.

156. Bernhard, W., Lung surfactant: Function and composition in the context of development and respiratory physiology. *Annals of Anatomy* **2016,** *208*, 146-150.

157. Perring, A. E.; Schwarz, J. P.; Markovic, M. Z.; Fahey, D. W.; Jiminez, J. L.; Campuzano-Jost, P.; Palm, B. D.; Wisthaler, A.; Mikoviny, T.; Diskin, G.; Sachse, G.; Ziemba, L.; Anderson, B.; Shingler, T.; Crosbie, E.; Sorooshian, A.; Yokelson, R.; Gao, R., In situ measurements of water uptake by black carbon-containing aerosol in wildfire plumes. *Journal of Geophysical Research: Atmospheres* **2017,** *122*, 1086-1097.

158. Gzyl-Malcher, B.; Paluch, M., Studies of lipid interactions in mixed Langmuir monolayers. *Thin Solid Films* **2008,** *516* (24), 8865-8872.

159. Blume, A., Lipids at the Air - Water Interface. *ChemTexts* **2018,** *4*, 3.

160. Shen, Y. R., Surface properties probed by second-harmonic and sum-frequency generation. *Nature* **1989,** *337* (9), 519-525.

161. Can, S. Z.; Chang, C. F.; Walker, R. A., Spontaneous formation of DPPC monolayers at aqueous/vapor interfaces and the impact of charged surfactants. *Biochim Biophys Acta* **2008,** *1778* (10), 2368-77.

162. MacPhail, R. A.; Strauss, H. L.; Elliger, C. A., C-H Stretching Modes and the Structure of n-Alkyl Chains. 2. Long, All-Trans Chains. *J. Phys. Chem.* **1984,** *88* (3), 334-341.

163. Snyder, R. G.; Strauss, H. L.; Elliger, C. A., C-H Stretching Modes and the Structure of n-Alkyl Chains. 1. Loong, Disordered Chains. *J. Phys. Chem.* **1982,** *86*, 5145-5150.

164. Can, S. Z.; Mago, D. D.; Esenturk, O.; Walker, R. A., Balancing Hydrophobic and Hydrophilic Forces at the Water/Vapor Interface: Surface Structure of Soluble Alcohol Monolayers. *J. Phys. Chem.* **2007,** *111*, 8739-8748.

165. Ma, G.; Allen, H. C., Condensing Effect of Palmitic Acid on DPPC in Mixed Langmuir Monolayers. *Langmuir* **2007,** *23* (2), 589-597.

166. Walker, R. A.; Gragson, D. E.; Richmond, G. L., Induced Changes in Solvent Structure by Phospholipid Monolayer Formation at a Liquid-Liquid Interface. *Physicochemical and Engineering Aspects* **1999,** *154* (1-2), 175-185.

167. Yun, H.; Choi, Y.-W.; Kim, N.; Sohn, D., Physicochemical Properties of Phosphatidylcholine (PC) Monolayers with Different Alkyl Chains, at the Air/Water Interface. *Bull. Korean Chem. Soc.* **2003,** *24* (3), 377-383.

168. Finot, E.; Markey, L.; Hane, F.; Amrein, M.; Leonenko, Z., Combined atomic force microscopy and spectroscopic ellipsometry applied to the analysis of lipid–protein thin films. *Colloids and Surfaces B: Biointerfaces* **2013,** *104*, 289-293.

169. Kamble, S.; Patil, S.; Kulkarni, M.; Murthy, A. V. R., Spectroscopic Ellipsometry of fluid and gel phase lipid bilayers in hydrated conditions. *Colloids and Surfaces B: Biointerfaces* **2019,** *176*, 55-61.

170. Zhao, Q.; Li, Y. A.; Chai, X.; Xu, L.; Zhang, L.; Ning, P.; Huang, J.; Tian, S., Interaction of inhalable volatile organic compounds and pulmonary surfactant: Potential hazards of VOCs exposure to lung. *Journal of Hazardous Materials* **2019,** *369*, 512-520.

171. Frerking, I.; Günther, A.; Seeger, W.; Pison, U., Pulmonary surfactant: functions, abnormalities and therapeutic options. *Intensive Care Med* **2001,** *27*, 1699-1717.

172. Pradhan, P.; Giri, J.; Rieken, F.; Koch, C.; Mykhaylyk, O.; Döblinger, M.; Banerjee, R.; Bahadur, D.; Plank, C., Targeted temperature sensitive magnetic liposomes for thermo-chemotherapy. *Journal of Controlled Release* **2010,** *142*, 108-121.

173. Andresen, T. L.; Davidsen, J.; Begtrup, M.; Mouritsen, O. G.; Jørgensen, K., Enzymatic Release of Antitumor Ether Lipids by Specific Phospholipase A2 Activation of Liposome-Forming Prodrugs. *J. Med. Chem.* **2004,** *47*, 1694-1703.

174. Li, S.; Du, L.; Wang, W., Impact of anions on the surface organisation of lipid monolayers at the air-water interface. *Environmental Chemistry* **2017,** *14* (7), 407-416.

175. Phillips, M. C.; Chapman, D., Monolayer characteristics of saturated 1,2-diacyl phosphatidycholines (lecithins) and phosphatidylethanolalimes at the air-water interface. *Biochem. Biophys. Acta* **1968,** *163*.

176. Adams, E. M.; Casper, C. B.; Allen, H. C., Effect of cation enrichment on dipalmitoylphosphatidylcholine (DPPC) monolayers at the air-water interface. *Journal of Colloid and Interface Science* **2016,** *478*, 353-364.

177. Lopez-Oyama, A. B.; Flores-Vazquez, A. L.; Burboa, M. G.; Gutierrez-Millan, L. E.; Ruiz-Garcia, J.; Valdez, M. A., Interaction of the Cationic Peptide Bactenecin with Phospholipid Monolayers at the Air-Water Interface: I Interaction with 1,2-Dipalmitoyl-sn-Glycero-3-Phosphatidilcholine. *Journal of Physical Chemistry B* **2009,** *113* (29), 9802-9810.

178. Adams, E. M.; Allen, H. C., Palmitic Acid on Salt Subphases and in Mixed Monolayers of Cerebrosides: Application to Atmospheric Aerosol Chemistry. *Atmosphere* **2013,** *4* (4), 315-336.

179. Casillas-Ituarte, N. N.; Chen, X.; Castada, H.; Allen, H. C., Na+ and Ca2+ effect on the hydration and orientation of the phosphate group of DPPC at air-water and airhydrated silica surface. *J. Phys. Chem. B.* **2010,** *114*, 9485-9495.

180. Tang, C. Y.; Allen, H. C., Ionic Binding of Na+ versus K+ to the carboxylic acid headgroup of palmitic acid monolayers studied by vibrational sum frequency generation spectroscopy. *J. Phys. Chem. A.* **2009,** *113*, 7383-7393.

181. Tang, C. Y.; Huang, Z.; Allen, H. C., Binding of Mg2+ and Ca2+ to palmitic acid and deprotonation of the COOH headgroup studied by vibrational sum frequency generation spectroscopy. *J. Phys. Chem. B.* **2010,** *114*, 17068-17076.

182. Shapovalov, V. L., Interaction of DPPC monolayer at air-water interface with hydrophobic ions. *Thin Solid Films* **1998,** *327-329*, 599-602.

183. Aroti, E.; Leontidis, E.; Maltseva, E.; Brezesinski, G., Effects of Hofmeister anions on DPPC Langmuir monolayers at air-water interface. *J. Phys. Chem. B.* **2004,** *108*, 15238-15245.

184. Sovago, M.; Wurpel, G. W. H.; Smits, M.; Müller, M.; Bonn, M., Calcium-induced phospholipid ordering depends on surface pressure. *J. Amer. Chem. Soc.* **2007,** *129*, 11079-11084.

185. Leontidis, E.; Aroti, E.; Belloni, L., Liquid-expanded monolayers of lipids as model systems to understand the anionic Hofmeister series: 1. A tale of models. *J. Phys. Chem. B.* **2009,** *113*, 1447-1459.

186. Eftaiha, A. F.; Paige, M. F., The influence of salinity on surfactant miscibility in mixed dipalmitoylphosphatidylcholine - perfluorooctadecanoic acid monolayer films. *J. Colloid. Interf. Sci.* **2011,** *353*, 210-219.

187. Christoforou, M.; Leontidis, E.; Brezesinski, G., Effects of sodium salts of lyotropic anions on low-temperature, ordered lipid monolayers. *J. Phys. Chem. B.* **2012,** *116*, 14602-14612.

188. Shaikh, N.; Queen, M. S.; Callis, P. R.; Walker, R. A., Surface Activity and Aggregation Behavior of Polyhydroxylated Fullerenes in Aqueous Solutions. *Carbon (in preparation)* **2022**.

189. Otis Jr., D. R.; Ingenito, E. P.; Kamm, R. D.; Johnson, M., Dynamic surface tension of surfactant TA: experiments and theory. *Journal of Applied Physiology* **1994,** *77* (6), 2681-2688.

190. Ma, G.; Allen, H. C., Real-Time Investigation of Lung Surfactant Respreading with Surface Vibrational Spectroscopy. *Langmuir* **2006,** *22*, 11267-11274.

191. Rugonyi, S.; Biswas, S. C.; Hall, S. B., The biophysical function of pulmonary surfactant. *Respiratory Physiology & Neurobiology* **2008,** *163*, 244-255.

192. Bouchoris, K.; Bontozoglou, V., A model of lung surfactant dynamics based on intrinsic interfacial compressibility. *Colloids and Surfaces A: Physicochemical and Engineering Aspects* **2021,** *624*, 126839.

193. Roohbakhshan, F.; Sauer, R. A., A finite membrane element formulation for surfactants. *Colloids and Surfaces A* **2019,** *566*, 84-103.

194. Ingenito, E. P.; Mark, L.; Morris, J.; Espinosa, F. F.; Kamm, R. D.; Johnson, M., Biophysical characterization and modeling of lung surfactant components. *Journal of Applied Physiology* **1999,** *86* (5), 1702-1714.

APPENDICES

APPENDIX A

SUPPORTING INFORMATION FOR CHAPTER TWO

Supporting information

CONTENTS:

- SHG power dependence measurements to demonstrate quadratic behavior
- Size exclusion chromatography-HPLC of PHFs
- Adsorption energies of PHFs in aqueous solutions

SHG power dependence measurements

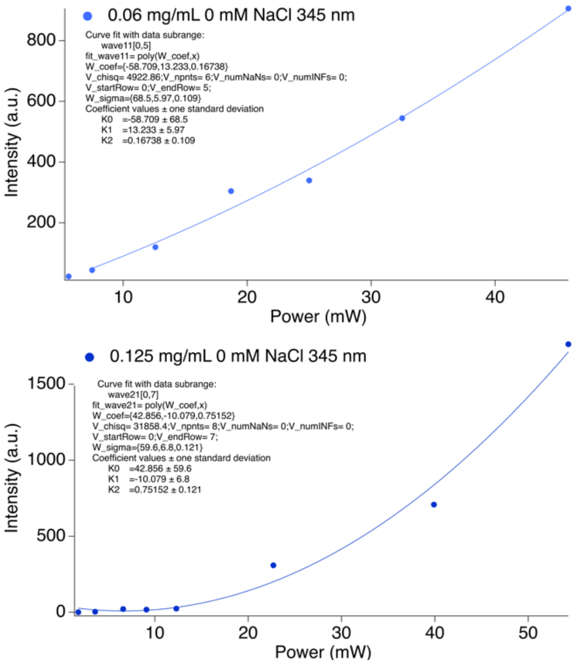

```
Curve fit with data subrange:
    wave11[0,5]
fit_wave11= poly(W_coef,x)
W_coef={-58.709,13.233,0.16738}
V_chisq= 4922.86;V_npnts= 6;V_numNaNs= 0;V_numINFs= 0;
V_startRow= 0;V_endRow= 5;
W_sigma={68.5,5.97,0.109}
Coefficient values ± one standard deviation
    K0   =-58.709 ± 68.5
    K1   =13.233 ± 5.97
    K2   =0.16738 ± 0.109
```

```
Curve fit with data subrange:
    wave21[0,7]
fit_wave21= poly(W_coef,x)
W_coef={42.856,-10.079,0.75152}
V_chisq= 31858.4;V_npnts= 8;V_numNaNs= 0;V_numINFs= 0;
V_startRow= 0;V_endRow= 7;
W_sigma={59.6,6.8,0.121}
Coefficient values ± one standard deviation
    K0   =42.856 ± 59.6
    K1   =-10.079 ± 6.8
    K2   =0.75152 ± 0.121
```

Figure SI-2.1. Power dependence (showing 2 photon process) confirming quadratic behavior for PHF concentrations of 0.06 mg/mL and 0.125 mg/mL in 0 mM NaCl (clean Millipore water).

The power dependence measurements in Figure SI-2.1 support that at the lower concentrations in Figure 2.4, the long wavelength background exhibits quadratic dependence of detected signal on incident intensity, confirming that the signal being detected at non-SHG wavelengths arises from a two-photon process.

Size exclusion chromatography-HPLC

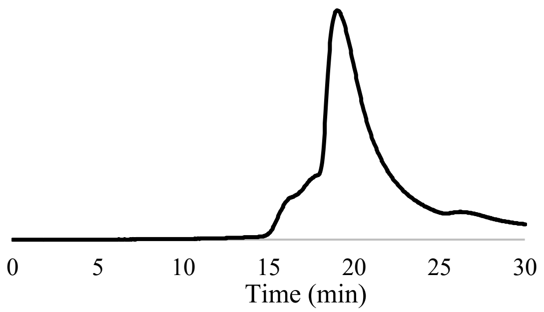

Figure SI-2.2. Chromatogram featuring a 0.06 mg/mL aqueous solution of analyte PHF.

Table SI-2.1**.** Results of mass analysis for aqueous solutions of analyte PHF. Across viable samples, the weight average molecular weight calculated for monomeric PHF species is **1100 ± 30 g/mol**, which corresponds with **22 ± 2 hydroxyl groups**.

Sample conc. (mg/mL)	M_W (g/mol)	M_N (g/mol)	PDI	-OH Groups
0.06	1130	470	2.4	24
0.06	1080	510	2.1	21
0.125	1090	760	1.4	22

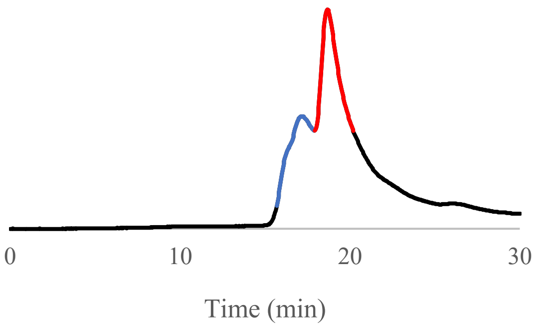

Figure SI-2.3. Demonstration of peak selection for a chromatogram featuring a 0.125 mg/mL aqueous solution of analyte PHF. Aggregates (blue) represent 36% of the total sample, while the representative monomeric PHF (red) comprises 64% of this sample.

Table SI-2.2**.** Relative area of peaks observed for 0.125 mg/mL aqueous solution of analyte PHF.

Peak	Area (a.u.)	Percent of Sample
Peak 1 (blue)	478931	36
Peak 2 (red)	864670	64

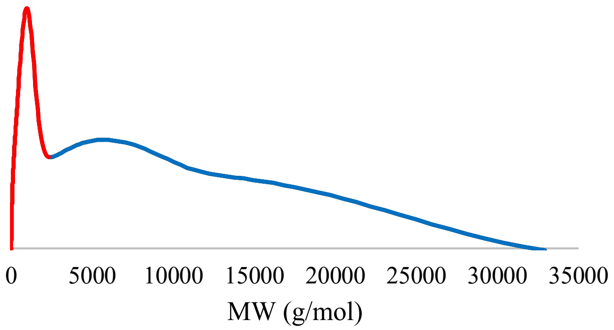

Figure SI-2.4. Mass profile obtained for 0.125 mg/mL aqueous solution of analyte PHF. Data corresponds with the chromatogram from Figure SI-3.2.

Table SI-2.3. Results of mass analysis for 0.125 mg/mL aqueous solution of analyte PHF. Weighted average molecular weight calculated for monomeric PHF species is 1130 g/mol, which corresponds with 24 -OH groups.

Peak	MW (g/mol)	MN (g/mol)	PDI
1 (blue)	14400	9400	1.5
2 (red)	1140	800	1.4
Total Analysis	12520	2720	4.6

Size exclusion chromatography (SEC)-HPLC was used to determine the molecular weight for a monomeric PHF. Representative data associated with the red peak was taken (same intensity on both sides of the peak). The resolution between monomer and aggregate peaks is limited, and as a result of the described analysis, traces that exhibit more aggregates will report a smaller monomer molecular weight. Therefore, a range of concentrations and sample preparation methods were explored in order to reduce aggregate presence. Because aggregation is a concentration dependent phenomenon, several PHF concentration samples were observed to have the best compromise between aggregation and detector sensitivity. Unintended interactions between analyte and solid phase may be amplified by charged (anionic) character of the analyte. These interactions were reduced through the selection of a high ionic strength eluent but may still contribute to unanticipated peak broadening and artificially reduce the reported mass through peak tailing. Data extracted from the red region was used to determine an average molecular weight of 1100 ± 30 g/mol suggesting 22 ± 2 hydroxyl groups/molecule.

Adsorption energies of PHFs in aqueous solutions

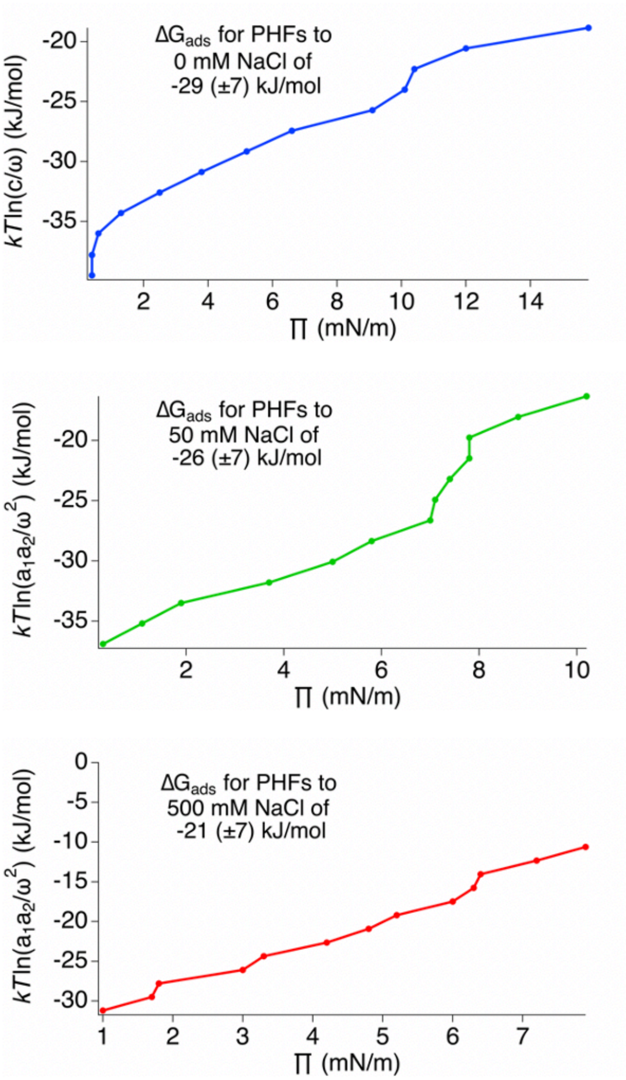

Figure SI-2.5. Adsorption energies of PHFs to 0, 50, and 500 mM NaCl.

Fitting data from Figure 2.1 lead to adsorption energies of -29 (±7) (0 mM NaCl), -26 (±7) (50 mM NaCl), and -21 (±7) (500 mM NaCl) kJ/mole [102].

APPENDIX B

SUPPORTING INFORMATION FOR CHAPTER THREE

Supporting Information

CONTENTS:

- PHF surface excess coverage at selected PHF bulk concentrations
- Reflectivity measurements from aqueous solutions containing PHFs

PHF surface activity

Table SI-3.1. PHF surface coverages (in both molecules/cm^2 and Å^2/molecule) in Millipore water as a function of PHF concentration.

PHF concentration (mg/mL)	Millipore water	
	(/cm^2)	Å^2
Terminal coverage	$7.5*10^{13}$	130
0.50	$7.5*10^{13}$	130
0.25	$6.6*10^{13}$	150
0.125	$4.6*10^{13}$	220
0.060	$2.6*10^{13}$	380
0.030	$1.4*10^{13}$	730
0.0075	$3*10^{12}$	$\geq$3000

According to the Gibbs adsorption equation ($\Gamma = \frac{d\Pi}{dln[C]} * \frac{1}{kT}$), the slope of steepest ascent in Figure 3.1 provides a direct measure of the terminal PHF surface excess concentration [140]. The data show PHFs are, in fact, surface active despite their high solubility in aqueous solution. Specifically, PHFs have terminal surface coverages of 130 Å^2/molecule in neat Millipore water.

Reflectivity measurements

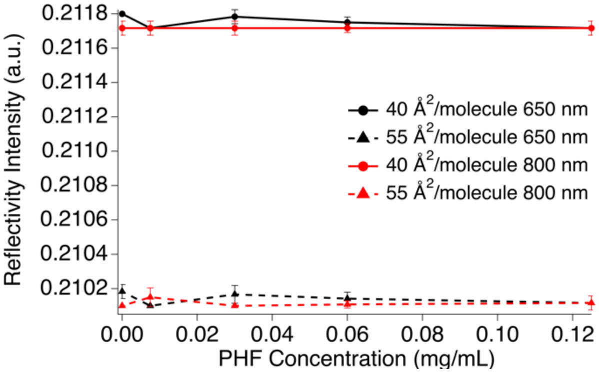

Figure SI-3.2. Reflectivity values at 650 and 800 nm on different concentrations of PHFs in neat Millipore with DPPC surface coverages of 55 and 40 Å^2/molecule. Monolayer thickness uncertainties range between ±0.034 and ±0.16 nm.

Optical properties, specifically thickness values, were measured using spectroscopic ellipsometry (see Figure 3.6), which were then used to simulate reflectivity intensities. Similar to thickness data, reflectivity data were analyzed in CompleteEASE, a modeling software application distributed by J.A. Woollam. Figure SI-3.2 confirms that the rising baseline with increasing PHF concentration exhibited in Figure 3.4 is not attributed to changes in reflectivity.

APPENDIX C

SUPPORTING INFORMATION FOR CHAPTER FOUR

Supporting information

CONTENTS:

- PHF surface activity

PHF surface activity

Table SI-4.1. PHF surface coverages (in both molecules/cm^2 and Å^2/molecule) in 0 and 500 mM NaCl as a function of PHF concentration.

PHF concentration (mg/mL)	**0 mM NaCl**		**500 mM NaCl**	
	(/cm^2)	**Å^2**	**(/cm^2)**	**Å^2**
Terminal coverage	$6.4*10^{13}$	155	$2.5*10^{13}$	404
0.519	$6.4*10^{13}$	155	$2.5*10^{13}$	404
0.260	$5.1*10^{13}$	194	$2.5*10^{13}$	404
0.130	$3.7*10^{13}$	273	$2.5*10^{13}$	404
0.063	$2.3*10^{13}$	434	$2.4*10^{13}$	408
0.033	$1.4*10^{13}$	705	$2.3*10^{13}$	428
0.008	$4.3*10^{12}$	≥2200	$1.8*10^{13}$	549

According to the Gibbs adsorption equation ($\Gamma = \frac{d\Pi}{dln[C]} * \frac{1}{kT}$), the slope of steepest ascent in Figure 4.1 provides a direct measure of the terminal PHF surface excess concentration.[140] The data show PHFs are, in fact, surface active despite their high solubility in aqueous solution. Specifically, PHFs have terminal surface coverages of 155 Å^2/molecule in 0 mM NaCl (neat Millipore water), and 404 Å^2/molecule in 500 mM NaCl.